



HAL
open science

Modeling of particle mixing in the atmosphere

Shupeng Zhu

► **To cite this version:**

Shupeng Zhu. Modeling of particle mixing in the atmosphere. Environmental Engineering. Université Paris-Est, 2015. English. NNT : 2015PESC1156 . tel-01384607

HAL Id: tel-01384607

<https://pastel.hal.science/tel-01384607>

Submitted on 20 Oct 2016

HAL is a multi-disciplinary open access archive for the deposit and dissemination of scientific research documents, whether they are published or not. The documents may come from teaching and research institutions in France or abroad, or from public or private research centers.

L'archive ouverte pluridisciplinaire **HAL**, est destinée au dépôt et à la diffusion de documents scientifiques de niveau recherche, publiés ou non, émanant des établissements d'enseignement et de recherche français ou étrangers, des laboratoires publics ou privés.



Thèse de doctorat de l'Université Paris-Est

Présentée et soutenue publiquement le 11 décembre 2015 par

Shupeng ZHU

pour l'obtention du diplôme de docteur
de l'Université Paris-Est

Spécialité: Sciences et Techniques de l'Environnement

Modélisation du mélange des particules dans l'atmosphère

Jury composé de

P ^r John Wenger	University College Cork	Président et examinateur
P ^r Yang Zhang	North Carolina State University	Rapporteur
P ^r Nicole Riemer	University of Illinois	Rapporteur
P ^r Christian Seigneur	ENPC, CEREА	Examineur
D ^r Bertrand Bessagnet	INERIS	Examineur
D ^r Karine Sartelet	ENPC, CEREА	Directrice de thèse

Acknowledgements

This thesis was supported by CEREAs, joint laboratory École des Ponts ParisTech EDF R&D. My deepest gratitude goes to CEREAs for financing this thesis.

I would like to express my sincere gratitude to my supervisor Karine Sartelet for her patient and inspiring guidance during pass three years. I also want to thank the director of our laboratory and also the supervisor of my first year PhD study, Christian Seigneur. Karine and Christian, together, they guide me into the universe of air quality modelling and inspire my enthusiasm of scientific research. Also, it was them who sincerely helped me to polish papers and this manuscript. I will not forget these enjoyably three years studying with them.

I am also deeply grateful to my thesis committee, Prof Wenger John, Prof Yang Zhang, Prof Nicole Riemer, Dr Bessagnet Bertrand for their attendance and encouragement. In particular, I sincerely thank my thesis referees, Prof Yang Zhang and Prof Nicole Riemer for their helpful comments and coming to Paris from the US. Additionally, I thank Prof Wenger John for sparing a time from his busy schedule and coming to Paris from Ireland.

I would like to thank my colleague Dr Youngseob Kim for his many helps during my PhD thesis and sharing his knowledge. Usually, his is the first person I turned to whenever a obstacle comes up. I thank our research engineer Sylvain Doré for helping me solving technical problems and improving my technical skills. My thanks also goes to my former colleague Stephanie Deschamps, we have a lot insightful discussions before she left. I also want to thank Dr Florian Couvidat for his support in solving the organic aerosol formation issue during the model development, and Dr Edouard Debry for his help in improving the computation of particle coagulation coefficient.

Those three years in CEREAs will be treasures of my memory. I enjoyed the harmonious and friendly working environments here. Everybody is kind and enthusiasm here, they are sharing cakes and presents whenever there is a birthday of one colleague or just after someone's journey. So I would like to send my gratitude to all of them, present or former colleagues: Véronique Dehlinger, Marc Bocquet, Yelva Roustan, Mounir Chrit, Ruiwei Chen, Valentin Raffort, Carole Legorgeu, Jérôme Drevet, Laëtitia Girault, Nicolas Yan, Charbel Abdallah, Laëtitia Thouron, Juliette Pinon, Nicolas Chérin, Rémy Nsir, Xiao Wei, Zhenlan Gao, Eve Lecoœur, Victor Winiarek, Yiguo Wang, etc.

Finally, my deepest gratitude goes to my parents for their support and encouragement. I thank my father for always encourage me to pursue my dreams and be a better man. I also appropriate for the support and comfort from my mother whenever I was depressed and frustrated. Without them, I would never go this far.

Abstract

This thesis presents a newly developed size-composition resolved aerosol model (SCRAM), which is able to simulate the dynamics of externally-mixed particles in the atmosphere, and evaluates its performance in three-dimensional air-quality simulations. The main work is split into four parts. First, the research context of external mixing and aerosol modelling is introduced. Secondly, the development of the SCRAM box model is presented along with validation tests. Each particle composition is defined by the combination of mass-fraction sections of its chemical components or aggregates of components. The three main processes involved in aerosol dynamic (nucleation, coagulation, condensation/evaporation) are included in SCRAM. The model is first validated by comparisons with published reference solutions for coagulation and condensation/evaporation of internally-mixed particles. The particle mixing state is investigated in a 0-D simulation using data representative of air pollution at a traffic site in Paris. The relative influence on the mixing state of the different aerosol processes and of the algorithm used to model condensation/evaporation (dynamic evolution or bulk equilibrium between particles and gas) is studied. Then, SCRAM is integrated into the Polyphemus air quality platform and used to conduct simulations over Greater Paris during the summer period of 2009. This evaluation showed that SCRAM gives satisfactory results for both $PM_{2.5}/PM_{10}$ concentrations and aerosol optical depths, as assessed from comparisons to observations. Besides, the model allows us to analyze the particle mixing state, as well as the impact of the mixing state assumption made in the modelling on particle formation, aerosols optical properties, and cloud condensation nuclei activation. Finally, two simulations are conducted during the winter campaign of MEGAPOLI (Megacities : Emissions, urban, regional and Global Atmospheric POLLution and climate effects, and Integrated tools for assessment and mitigation) in January 2010 where the composition of individual particles was measured. One simulation assumes that particles are internally mixed, while the other explicitly models the mixing state with SCRAM. The simulation results of both bulk concentrations of chemical species and concentrations of individual particle classes are compared with the measurements. Then, the single particle diversity and the mixing-state index are computed using a quantification approach based on information-theoretic entropy, and they are compared to those derived from the measurements at a urban site in Paris: the simulated mixing-state index is equal to 69% against 59% from the measurements, indicating that particles are not internally mixed over Paris.

Résumé

Cette thèse présente un nouveau modèle SCRAM (Size and Composition Resolved Aerosol Model) pour simuler la dynamique des particules dans l'atmosphère (nucléation, coagulation, condensation / évaporation) en prenant en compte leur état de mélange, et elle évalue la performance de SCRAM dans des simulations 3D de qualité de l'air. Le travail peut être divisé en quatre parties. Premièrement, la notion de mélange externe est introduite, ainsi que la modélisation de la dynamique des aérosols. Ensuite, le développement du modèle SCRAM est présenté avec des tests de validation. Dans SCRAM, pour définir les compositions, on discrétise d'abord en sections les fractions massiques des composés chimiques des particules ou d'ensembles de composés chimiques. Les compositions des particules sont ensuite définies par les combinaisons des sections de fractions massiques. Les trois processus principaux impliqués dans la dynamique des aérosols (la coagulation, la condensation / évaporation et la nucléation) sont inclus dans SCRAM. SCRAM est validé par comparaison avec des simulations « académiques » publiées dans la littérature de coagulation et condensation/évaporation pour des particules en mélange interne. L'impact de l'hypothèse de mélange externe pour ces simulations est notamment étudié. L'impact du degré de mélange sur les concentrations de particules est ensuite étudié dans une simulation 0-D en utilisant des données représentatives d'un site trafic en Ile de France. L'influence relative sur l'état de mélange des différents processus influençant la dynamique des particules (condensation / évaporation, coagulation) et de l'algorithme utilisé pour modéliser la condensation / évaporation (hypothèse d'équilibre entre les phases gazeuse et particulaire, ou bien modélisation dynamique des échanges gaz/particules) est étudiée. Ensuite, SCRAM est intégré dans la plate-forme de qualité de l'air Polyphemus et utilisé pour effectuer des simulations sur l'Ile de France pendant l'été 2009. Une évaluation par comparaison à des observations a montré que SCRAM donne des résultats satisfaisants pour les concentrations de $PM_{2.5}/PM_{10}$ et l'épaisseur optique des aérosols. Le modèle est utilisé pour analyser l'état de mélange des particules, ainsi que l'impact des différentes hypothèses de mélange (mélange interne MI ou mélange externe ME) sur la formation des particules et leurs propriétés. Enfin, deux simulations, une avec l'hypothèse de MI et une autre avec l'hypothèse de ME, sont effectuées entre le 15 janvier et le 11 février 2010, pendant la campagne hiver MEGAPOLI (Megacities : Emissions, urban, regional and Global Atmospheric POLLution and climate effects, and Integrated tools for assessment and mitigation) durant laquelle les compositions des particules individuelles ont été mesurées. Les concentrations simulées de composés chimiques (concentration massique totale de différents composés) et les concentrations des classes de particules individuelles (une classe est définie par sa taille et sa composition chimique) sont comparées avec les observations à un site urbain parisien. Un indicateur de la diversité des particules et de l'état de mélange est calculé à partir des simulations et comparé

à celui calculé à partir des mesures. Le modèle se compare bien aux observations avec un état de mélange moyen simulé de 69% contre 59% dans les observations, indiquant que les particules ne sont pas en mélange interne sur Paris.

List of Figures

1.1	Particle size and their corresponding intrusion areas within the human respiration system [Hussgroup.com, 2015]	19
1.2	This composite photograph shows Beijing central business district during heavy aerosol pollution on 20 Feb. 2014 and during good air quality condition on 19 Feb. 2014 (taken by Qingxiong Zheng).	21
1.3	Global average radiative forcing (RF) in 2005 with respect to 1750 for CO ₂ , CH ₄ , N ₂ O, aerosols and other important agents and mechanisms. LOSU stands for the level of scientific understanding. Blue bars indicate a negative or cooling effect on the climate. Red bars indicate a positive or heating effect. From Intergovernment Panel on Climate Control (IPCC) [2007].	22
1.4	Aerosol size distribution and morphology for various aerosol types. [Colbeck et al., 2014]	24
1.5	Illustration of (a) a group of internally mixed particles and (b) a group of externally mixed particles	27
1.6	An altitude-latitude distribution of observed tropospheric aerosols and their mixing states [Murphy et al., 2006]	28
1.7	Scheme of aerosol dynamics processes. [Raes et al., 2000]	29
1.8	Processes described in CTMs. [Sportisse, 2008]	35
2.1	Particle discretization schemes used in internal (a) and external (b) mixing aerosol models.	42
2.2	Simulation of condensation for hazy conditions: initial distribution and after 12 hours.	53
2.3	Mean and standard deviations of species 1 mass fraction as functions of particle diameter using 2, 10 and 100 composition sections.	54
2.4	Simulation of both coagulation and condensation for hazy conditions: initial distribution and after 12 hours.	55
2.5	Distribution after 12 hours: particle mass concentration as a function of diameter and mass fraction of species 1.	55
2.6	EC emissions over Greater Paris at 2 UT, 1 July 2009.	56
2.7	Transprt EC concentrations profile of on 1 July 2009.	56

2.8	Result mass distributions of externally-mixed particles as a function of particle diameter for the different chemical compositions for 6 different simulation scenarios: (a) Emission only; (b) Emission+Coagulation; (c) Emission+C/E; (d) Emission+Coagulation+C/E+nucleation; (e) Initial Condition; (f) Internal mixing result.	60
2.9	Result number distributions of externally-mixed particles as a function of particle diameter for the different chemical compositions for 6 different simulation scenarios: (a) Emission only; (b) Emission+Coagulation; (c) Emission+C/E; (d) Emission+Coagulation+C/E+nucleation; (e) Initial Condition; (f) Internal mixing result.	61
2.10	Result mass distributions of externally-mixed particles as a function of particle diameter for the different chemical compositions for 4 different C/E simulation scenarios: (a) External bulk-equilibrium; (b) Internal bulk-equilibrium; (c) External hybrid method; (d) Internal dynamic.	63
2.11	Result number distributions of externally-mixed particles as a function of particle diameter for the different chemical compositions for 4 different C/E simulation scenarios: (a) External bulk-equilibrium; (b) Internal bulk-equilibrium; (c) External hybrid method; (d) Internal dynamic.	64
3.1	Simulated domain located within the red rectangle	75
3.2	Time evolution of PM _{2.5} at BDQA site Gennevilliers (48.93 N°, 2.29 E°) between 28 June and 5 July 2009	79
3.3	Time evolution of NO ₃ ⁻ and NH ₄ ⁺ at BDQA site Gennevilliers (48.93 N°, 2.29 E°) between 28 June and 5 July 2009	80
3.4	Spatial distribution of EC mixing state over Paris region	81
3.5	Temporal evolution of EC mixing state over Paris region	82
3.6	Comparison between partition of EC mass amongst the particle types at urban and rural site (Week averaged at ground level)	83
3.7	(a) Comparison of AOD between different mixing assumptions and the observation; (b) comparison of SSA between internal and external mixing case; Both plot is based on the data collected from the location of AERONET site Paris (48.87° N, 2.33° E; 50 m a.s.l.)	86
3.8	Spatial distribution of differences between different mixing assumptions of different parameters	87
3.9	(a) Averaged mass fraction of each particle types (all level); (b) Averaged AOD fraction contribute by each particle types	88
3.10	Spatial distribution of weekly averaged CCN activation percentage differences (%) between internal and external mixing under (a) high supersaturation (1%), (b) low supersaturation (0.02%)	90
3.11	Averaged CCN activation percentage and CCN activation difference (%) for different supersaturation % at urban site.	91
3.12	CCN contribution of each particle types under 1% and 0.02% of supersaturation.	92
3.13	Averaged fraction of each particle type to total aerosol number concentration	93

4.1	Map of three domains of simulations: Europe ($[-14.75^{\circ}\text{E}, 34.75^{\circ}\text{E}] \times [35.25^{\circ}\text{N}, 69.75^{\circ}\text{N}]$, resolution: $0.5^{\circ} \times 0.5^{\circ}$), France ($[-5.0^{\circ}\text{E}, 10.0^{\circ}\text{E}] \times [41^{\circ}\text{N}, 52^{\circ}\text{N}]$, resolution: $0.1^{\circ} \times 0.1^{\circ}$) and Greater Paris ($[1.35^{\circ}\text{E}, 3.55^{\circ}\text{E}] \times [48.00^{\circ}\text{N}, 49.50^{\circ}\text{N}]$, resolution: $0.02^{\circ} \times 0.02^{\circ}$)	100
4.2	Comparisons of the IM (blue line) and the EM (green line) simulation results with ATOFMS-derived mass concentrations for PM_{10} , EC, OA and inorganic ions (Obs. stands for observation - red line)	105
4.3	Mass-size distribution (left, stacked) and size-resolved average mass fractions (right, stacked) for each chemical species from external mixing simulation.	108
4.4	Mass-size distribution (left, stacked) and size-resolved average mass fractions (right, stacked) for each chemical species from inter mixing simulation using bulk equilibrium approach with updated redistribution method. . .	111
4.5	Dependence of the time-averaged number concentration on single particle diversity (diversity normalised by the number of particles in each section) and particle diameter (upper panel), and dependence of time-averaged particle composition on particle diameter (lower panel).	116
4.6	Scattering plot of the hourly mixing-state index (χ) as a function of average particle diversity (D_{α}) and average bulk population diversity (D_{γ}). . . .	118
4.7	Diurnal variations of the mixing state index (χ) and bulk population mass fraction.	119
4.8	Spatial distribution of time-averaged average single particle diversity (D_{α} , a), average bulk population diversity (D_{γ} , b), difference between D_{α} and D_{γ} (c), and mixing state index (χ , d) over Greater Paris.	120

List of Tables

2.1	20 Externally-mixed particle compositions	58
2.2	Mixing state after 12hs simulation	59
2.3	Computational times	65
3.1	20 Externally-mixed particle compositions	76
3.2	Definitions of the statistics used in this work. $(o_i)_i$ and $(c_i)_i$ are the observed and the model concentrations at time and location i , respectively. n is the number of data	78
3.3	Statistics between simulation results and the measurements of the BDQA (Base de Données sur la Qualité de l Air) network during the MEGAPOLI summer experiment. (Obs. stands for observation. Sim. stands for simulation. Corr. stands for correlation.)	78
3.4	CRI of simulated species at $\lambda=550$ nm in dry state	84
3.5	Statistics between AOD values computed from simulation results and the measurements of the AERONET. (Obs. stands for observation. Sim. stands for simulation. Corr. stands for correlation.)	85
4.1	17 Externally-mixed particle compositions	102
4.2	Definitions of the statistics used in this work. $(o_i)_i$ and $(c_i)_i$ are the observed and the simulated concentrations at time and location i , respectively. n is the number of data	104
4.3	Statistics between the IM and EM simulation results (from 15 January to 11 February) and the measurements of the BDQA network during the MEGAPOLI winter campaign. (Obs. stands for observation. Sim. stands for simulation. Corr. stands for correlation.)	104
4.4	Statistics between the IM and EM simulation results (from 15 January to 11 February) and the measurements of [Healy et al., 2013] at LHVP site (48.75° N, 2.36° E) during the MEGAPOLI winter campaign. (Obs. stands for observation. Sim. stands for simulation. Corr. stands for correlation.)	106
4.5	Mass ratio of each particle class to the total mass, and the mass fraction of each chemical group within each particle class	109
4.6	Mass ratio of particle class to the total mass, and the mass fraction of each chemical group within each particle class	112
4.7	Mass fractions of each chemical group determined for each ATOFMS class [Healy et al., 2013], and their corresponding SCRAM class	113
4.8	Mass fractions of each chemical group for EC-rich and EC-poor particles from both observation (Obs.) and simulation (Sim.)	113

4.9	Statistics of EC-rich and EC-poor particles between simulation results (15 to 28 January) and the measurements of [Healy et al., 2013] at LHVP site (48.75° N, 2.36° E). (Obs. stands for observation. Sim. stands for simulation. Corr. stands for correlation.)	113
-----	---	-----

Contents

1	Introduction	17
1.1	Particles and their adverse effects	18
1.1.1	Effect on human health	19
1.1.2	Effect on visibility	20
1.1.3	Effect on climate	20
1.2	Aerosol origins and properties	23
1.2.1	Aerosol origins and compositions	23
1.2.2	Morphology and size distribution	23
1.2.3	Representation of the size distribution	25
1.3	Mixing state of particles	26
1.4	Aerosol dynamics	29
1.4.1	Nucleation	29
1.4.2	Coagulation	30
1.4.3	Condensation and evaporation	31
1.4.4	General dynamic equation	32
1.5	Air quality modelling	34
1.5.1	Chemical transport models	34
1.5.2	Aerosol modelling	36
1.5.3	Model performance evaluation	37
1.6	Objectives and plan of thesis	38
2	A size-composition resolved aerosol model for simulating the dynamics of externally-mixed particles: SCRAM (v 1.0)	41
2.1	Introduction	45
2.2	Model Description	46
2.2.1	Condensation-Evaporation Algorithm	47
2.2.2	Bulk equilibrium and hybrid approaches	51
2.2.3	Overall time integration and operator splitting in SCRAM	51
2.3	Model validation	52
2.4	Simulation with realistic concentrations	54
2.4.1	Simulation set-up	55
2.4.2	Aerosol dynamics and mixing state	58
2.4.3	External versus internal mixing	62
2.4.4	Bulk equilibrium and hybrid approaches	64
2.5	Conclusions	66

3	Three-dimensional modelling of the mixing state of particles over Greater Paris	69
3.1	Introduction	73
3.2	Model description and simulation setup	74
3.3	Particle concentrations	77
3.3.1	PM concentrations	77
3.3.2	Inorganic aerosol formation	80
3.3.3	Mixing state of EC	81
3.4	Aerosol optical properties	83
3.4.1	Computation of aerosol optical properties	83
3.4.2	Comparisons to AERONET measurements	84
3.4.3	Influence of the mixing state	85
3.4.4	Contributions of particle types	88
3.5	Cloud Condensation Nuclei	89
3.5.1	Computation of CCN	89
3.5.2	Impact of the mixing state on CCN	90
3.5.3	Contribution of particle types	92
3.6	Conclusions	93
4	Simulation of particle diversity and mixing state over Greater Paris: Model-to-data comparison	95
4.1	Introduction	97
4.2	Model presentation	98
4.3	Simulation setup and measurement database	99
4.4	Result analysis and discussion	103
4.4.1	Bulk mass concentrations	103
4.4.2	Concentration of each particle composition	108
4.4.3	Mixing state analysis	114
4.5	Conclusion	121
5	Conclusion	123
5.1	Conclusions	124
5.2	Perspectives	126
5.2.1	Dynamic condensation/evaporation of organics	126
5.2.2	Cloud aerosol study	126
5.2.3	Source identifications and impact analysis	127
5.2.4	Improve the computational efficiency	127
A	Change of variables for the evolution of number and mass distributions	129
B	The time derivation of Equation (2.10) and (2.9)	133

Chapter 1

Introduction

Résumé

Ce chapitre présente le contexte de la thèse et la modélisation des aérosols, ainsi que l'objectif et le plan de thèse. Les particules ont des effets néfastes sur la santé humaine. Elles peuvent aussi dégrader la visibilité et affecter le climat en influant sur le bilan énergétique global. Les particules peuvent avoir plusieurs sources, naturelles ou anthropiques, avec des compositions distinctes. Elles ont une grande variété de tailles et de formes. Par souci de simplification, on les suppose sphérique en modélisation, et on définit un diamètre aérodynamique qui correspond au diamètre d'une particule sphérique de taille équivalente. Les distributions en taille des particules atmosphériques peuvent souvent être caractérisées par une superposition de plusieurs modes log-normaux, et dans les modèles, elles sont souvent représentées soit par une approche modale ou une approche sectionnelle. En général, l'état de mélange des particules définit le degré de mélange entre des particules de différentes origines. Les particules sont considérées comme étant en mélange interne, lorsque toutes les particules de la même taille ont une composition homogène, sinon elles sont considérées comme étant en mélange externe. Le mélange de particules est contrôlé par plusieurs processus décrivant la dynamique des aérosols: la nucléation, la coagulation et la condensation / évaporation. L'influence de ces processus dynamiques sur la distribution des particules peut être décrit par l'équation de dynamique générale (GDE). Les modèles d'aérosols simulent l'évolution des distributions de particules en résolvant la GDE. Les modèles d'aérosols font souvent l'hypothèse de mélange interne (composition homogène par taille de particules). Ces modèles sont intégrés dans des modèles de chimie transport pour simuler la qualité de l'air atmosphérique.

Sommaire

1.1	Particles and their adverse effects	18
1.1.1	Effect on human health	19
1.1.2	Effect on visibility	20
1.1.3	Effect on climate	20
1.2	Aerosol origins and properties	23
1.2.1	Aerosol origins and compositions	23
1.2.2	Morphology and size distribution	23

1.2.3	Representation of the size distribution	25
1.3	Mixing state of particles	26
1.4	Aerosol dynamics	29
1.4.1	Nucleation	29
1.4.2	Coagulation	30
1.4.3	Condensation and evaporation	31
1.4.4	General dynamic equation	32
1.5	Air quality modelling	34
1.5.1	Chemical transport models	34
1.5.2	Aerosol modelling	36
1.5.3	Model performance evaluation	37
1.6	Objectives and plan of thesis	38

1.1 Particles and their adverse effects

An aerosol is usually defined as a colloidal system of solid or liquid particles in a gas. Particles in suspension in the atmosphere can vary from several nanometres to tens of micrometers with extreme diversity in both morphological and physiochemical characteristics [Putaud et al., 2010]. Particles can be introduced into the atmosphere either by direct emissions or through aggregation/nucleation from gas molecules. The former ones are known as primary particles while the later ones are identified as secondary particles. Primary particles are emitted through combustion, suspension of sea spray, suspension of dust, volcanoes, etc. Some chemical compounds of particles are secondary: they are formed through the nucleation or the condensation/evaporation of gas. Particles are mostly transported through diffusion and advection. Depending on their size, the lifetime of particles vary from a few hours to several days. Particles are often removed from the atmosphere by precipitation or absorbed by cloud droplets, such process is known as wet deposition or wet scavenging. According to Anthony and Mary-Scott [1990], considering the annual global mean, the majority of particle mass is removed by wet deposition processes, while only less than 20% of particle mass is removed by dry deposition.

People have acknowledged the existence of particles in the atmosphere for centuries. Back to 44 BC, the cool summers and poor harvests after the eruption of Mount Etna caused people to suspect the impact of particles released by the volcano on the local climate. Records about regional haze caused by forest fire can be found in historical documents ranging from the seventeenth to nineteenth century. As early as 1767, efforts have been made to map the path of the smoke based on the locations of the fires and their appearances at different locations [Colbeck et al., 2014].

Despite of the common appearance of particles in nature and their frequent association to daily life issues, it is only in comparatively recent times that detailed scientific studies have been held to investigate their properties and behaviour. While those studies continue, the multiple adverse effects of particles are revealed ranging from those on human health to those on visibility and climate.

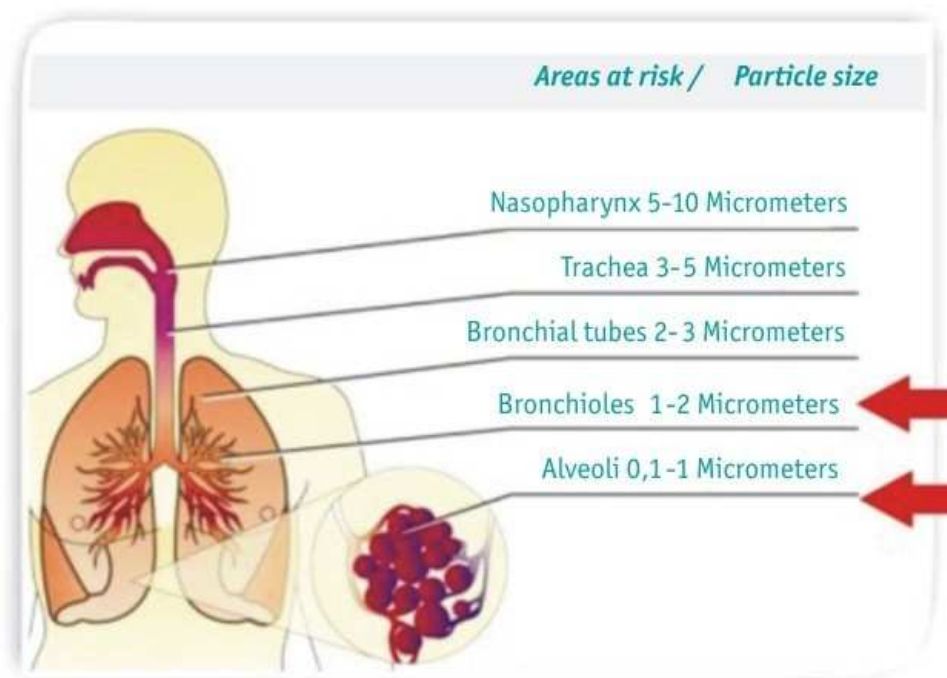


Figure 1.1: Particle size and their corresponding intrusion areas within the human respiration system [Hussgroup.com, 2015]

1.1.1 Effect on human health

Atmospheric particles can reach human body in many ways such as skin attachment, food contamination and inhalation through the respiration system. Inhalation is an efficient way for particles to reach human body, as adults take in average 16-20 breaths per minute to get enough oxygen, and about 10 L air per minute.

Figure 1.1 shows the possible intrusion areas within the human respiration system for different particle sizes. Coarse particles of diameters larger than 10 μm are basically harmless, as most of them are stopped by the cilia and mucus within the nose and the throat. However, particles of diameters lower than 10 μm can go through the nose and the throat and reach the sensitive bronchi or lungs. Such particles may stimulate the human immune system, and cause inflammation as white blood cells try to destroy those intruders [Seaton et al., 1995], which can lead to severe health issues especially for patients with long-term respiration problems like asthma [Tolbert et al., 2000]. For such reason, the concentration of particulate matter of diameter lower than 10 μm (PM_{10}) is monitored and regulated in the U.S as well as in Europe.

Fine particles of diameter lower than 2.5 μm ($\text{PM}_{2.5}$) are able to reach the alveolar at the end of bronchi, which is the gas exchange region of the lung. Particles resting in the alveolar are unlikely to be removed through ventilation such as cough and sneeze, but they are rather consumed by macrophages. This may decrease the overall immunity if the macrophage is overloaded. Besides, ultra-fine particles of diameter lower than 0.1 μm ($\text{PM}_{0.1}$) can pass directly into the blood circulatory system, thus directly impacting the cardiovascular system and other organs distant from the lungs [Polichetti et al., 2009].

Reports of epidemiology studies have confirmed that particles have large impacts

on morbidity and mortality. The World Health Organization (WHO) estimated that exposure to PM_{10} led to 3.7 millions of premature deaths worldwide in 2012 [WHO, 2014]. They also estimated that about 80% of aerosol-related premature deaths were due to heart disease and strokes, while 14% of deaths were due to chronic obstructive pulmonary disease or acute lower respiratory infections; and 6% were due to lung cancer. Considering the health effects of particles, WHO suggested that the annual mean concentrations of PM_{10} should be lower than $20 \mu\text{g m}^{-3}$ and $10 \mu\text{g m}^{-3}$ for $\text{PM}_{2.5}$. However, governments set their own standards based on local situations. For example, in China, the limits for annual mean concentrations are $70 \mu\text{g m}^{-3}$ for PM_{10} and $35 \mu\text{g m}^{-3}$ for $\text{PM}_{2.5}$ [GB 3095—2012, 2012], while in Europe, the regulation for annual PM_{10} is $40 \mu\text{g m}^{-3}$ and $25 \mu\text{g m}^{-3}$ for $\text{PM}_{2.5}$ [EU Air Quality Standards, 2015].

1.1.2 Effect on visibility

Visibility decreases when ambient light is either absorbed or scattered by airborne particles, thereby reducing the contrast in light intensity between a distant object and the background sky. Such degradation of visibility can be quite striking. Normally, one can see objects more than 200 kilometres away under clean, dry air condition. However polluted air can restrict visibility to less than one kilometre.

Figure 1.2 demonstrates how severe the degradation of visibility can be, because of particles. Such level of visibility degradation has large impacts on traffic activities, (e.g., roads, sailing and aviation). Low visibility reduces the observation range of drivers and pilots, thereby reducing their ability to scene obstacles or dangerous situations, which may lead to traffic accidents. Besides, it has been reported that the reduction of the visual range influences the psychological well being of people, increasing stress and degrading the enjoyment of outdoor leisure activities [Davidson et al., 2005]. For tourist attractions (e.g. seashores, national parks, landmarks), poor visibility may produce negative impact on their appealing and reduce their ability to attract tourists, therefore cause economic dis-benefits.

1.1.3 Effect on climate

The climate system on earth is driven by the energy from the sun. When the solar radiation reaches the earth, it is partially absorbed by different parts of the climate system (e.g., atmosphere, landmass and ocean), while the rest is reflected back into space. The absorbed energy warms up the earth and makes it habitable. As the temperature rises, each part of the climate system produces their own outgoing long-wave radiations, which in return colds the earth down. The net flow of energy into and out of the earth is described as the earth's radiation balance and is crucial to the climate evolution. The effect of particles on climate change is complex, as they can influence the earth's radiation balance directly, indirectly or even semi-directly.

Direct aerosol effects involve the scattering and absorption of both incoming or outgoing radiation within the atmosphere. In some cases, the presence of particles may increase the reflectance of solar radiation back to space, thus producing a net cooling effect on the earth. In other cases, particles may increase the absorption of radiation, resulting in a net warming effect. The global particle effect can be influenced by many



Figure 1.2: This composite photograph shows Beijing central business district during heavy aerosol pollution on 20 Feb. 2014 and during good air quality condition on 19 Feb. 2014 (taken by Qingxiong Zheng).

factors such as particle sizes, shapes, and compositions as well as the angle of the sun. For instance, ammonium sulphate particles have high albedos and hence cause cooling, while black carbon (EC) particles have high absorptions and cause warming. According to Jacobson [2002c], EC may be the second most important anthropogenic atmospheric constituent contributing to global warming, after CO_2 .

The indirect effects come from the change of cloud coverage and characteristics due to the presence of atmospheric particles serving as cloud condensation nuclei (CCN). Hygroscopic particles such as ammonium sulphate are efficient CCN, although hydrophobic particles may also become CCN [Koehler et al., 2009]. According to Twomey [1977], for two clouds with the same liquid water content, the one that contains more CCN particles (CCN rich) may have a larger amount of cloud droplets. Furthermore, these cloud droplets may have smaller sizes than those of the cloud with less CCN (CCN poor). As a result, the CCN-rich cloud may have a larger albedo, which could enhance its reflection ability and cooling effect. Besides, because smaller droplets require longer growth times to reach sizes of precipitation, this cloud can persist for longer time periods. This effect may enhance the cloud cover, thus imposing an additional cooling effect [Albrecht, 1989], which can influence the global radiative forcing and the climate.

The semi-direct effect is produced by absorbing aerosols, which have the potential to modify clouds properties, without directly acting as CCN. Hansen et al. [1997] introduced a possible mechanism to explain the semi-direct effect. First, by absorbing the solar energy, particles reduce the amount of solar radiation that reaches the ground, reducing temperature growth in the lowest layers of the atmosphere. At the same time, by heating

up the air surrounding them in the highest layers, they create a positive temperature gradient which stabilizes the atmosphere and diminishes convection and thus the potential for cloud formation. Secondly, at high altitudes, as the atmospheric temperature increases, relative humidity decreases, inhibiting cloud formation, and enhancing evaporation of existing clouds. These effects reduce the Earth's albedo due to the reduction of cloud cover and lead to a warming effect.

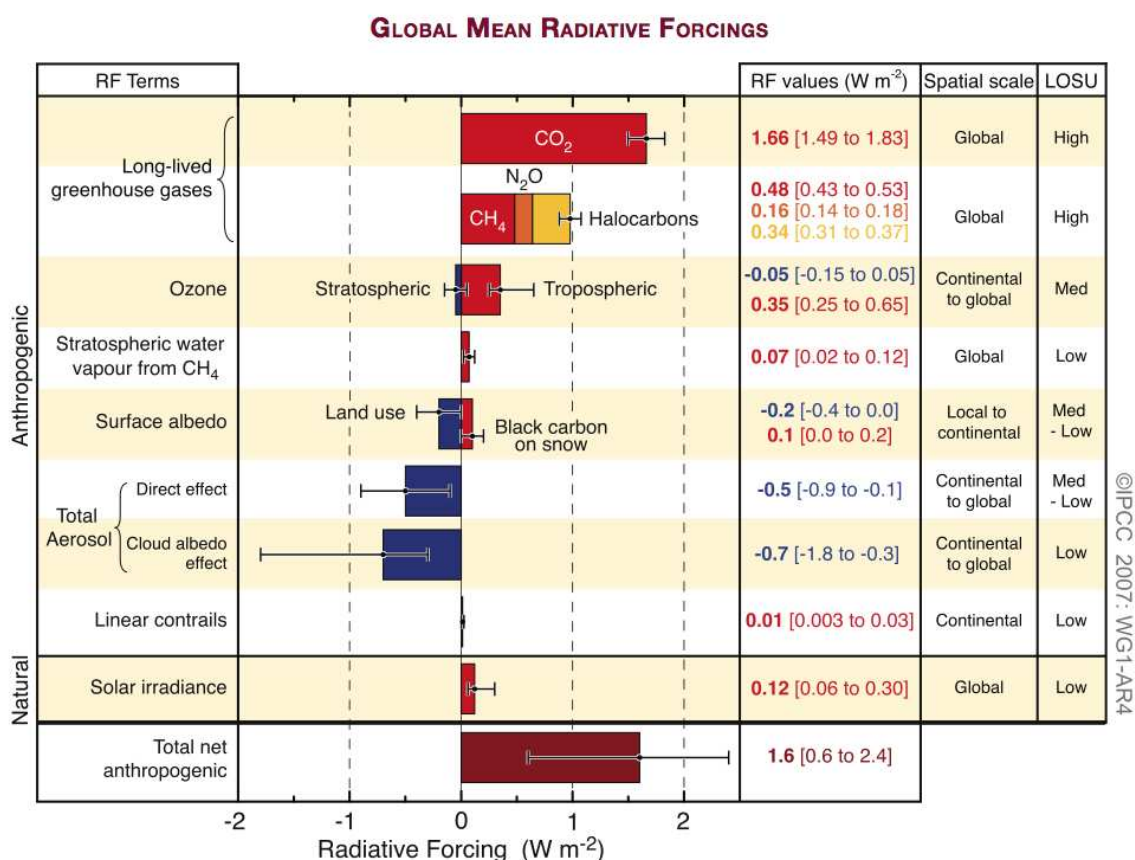


Figure 1.3: Global average radiative forcing (RF) in 2005 with respect to 1750 for CO₂, CH₄, N₂O, aerosols and other important agents and mechanisms. LOSU stands for the level of scientific understanding. Blue bars indicate a negative or cooling effect on the climate. Red bars indicate a positive or heating effect. From Intergovernment Panel on Climate Control (IPCC) [2007].

In addition, EC and other absorbing constituent of particles deposit on snow or ice surfaces, reducing the surface albedo, leading to reduced reflectance of solar radiation, and hence a warming effect [Hansen and Nazarenko, 2004].

The change in the earth's radiation balance due to anthropogenic or natural emission is referred to as radiative forcing (RF). RF is often used to quantify and compare the potential climate impact of the various aerosol effects. Figure 1.3 represents the global radiative forcing in 2005. It is clear that in general, both direct and indirect aerosol effects tend to produce negative RF, leading to a cooling effect.

1.2 Aerosol origins and properties

The abundance of aerosol diversity is largely caused by the great variety of its origins, with aerosols of different origins mixing and evolving. Particles from different sources can have distinct properties, sizes, and compositions. For example, combustion generated particles that can be as small as a few nanometres with carbonaceous compositions while sea spray particles originate from burst wave bubbles are generally larger than $1\ \mu\text{m}$, with high sodium chloride concentrations. Knowledge about aerosol origins and aerosol formation is essential to understand the nature of aerosols.

1.2.1 Aerosol origins and compositions

Based on their origins, atmospheric particles and their chemical components are either primary or secondary. Primary particles are those directly emitted into the atmosphere from either natural or anthropogenic sources. Secondary particles are formed in the atmosphere from precursor gases.

Primary particles are mostly composed of either inert (dust, black carbon), inorganic or organic chemical species. Primary particles from natural sources originate from sea spray (sodium, chloride, sulphate), desert (mineral dust), and volcanoes (dust, ash), etc.. They are usually relatively large (of diameter larger than $1\ \mu\text{m}$). These particles have short atmospheric lifetime, typically a few days. Anthropogenic primary particles are mostly made of black carbon (EC) and organic matter (OM). They are mostly produced through combustion processes, such as biomass burning and combustion of fossil fuels from traffic, residential heating, industry. Primary EC and OM containing particles are generally of diameter lower than $1\ \mu\text{m}$.

Secondary particles are produced in the atmosphere from precursor gases by homogeneous nucleation or by gas-to-particle conversion processes. Their main chemical components are sulphate, nitrate, ammonium, chloride and OM. The main precursor gases are emitted from fossil fuel combustion, agriculture, while biomass burning and biogenic emissions of VOCs are also important. Biogenic VOCs are generally produced by photosynthesis which is enhanced during the summer time when temperature and solar radiation are high. As a result, the formation of secondary organic aerosol (SOA) is favoured in summer. The evolution between gas and particles phases is largely related to the change of ambient environment such as temperature and humidity as well as the concentration and volatility of precursors. The volatility of precursors, such as volatile organic compounds (VOC), changes in the atmosphere by different processes: oligomerization (producing less volatile compounds with similar O:C ratio), oxidation reactions (leading to the formation of lower volatility compounds with higher O:C ratio) or fragmentation (producing higher volatility compounds) [Crippa et al., 2013].

1.2.2 Morphology and size distribution

Atmospheric particles have a great variety of sizes and shapes. Figure 1.4 shows an example of particle size distribution and morphology obtained from electron microscopy. There are spherical particles such as ammonium sulphate. While, there are also fibre like particles as well as particles with irregular shapes like dust and sea salt. The variety of

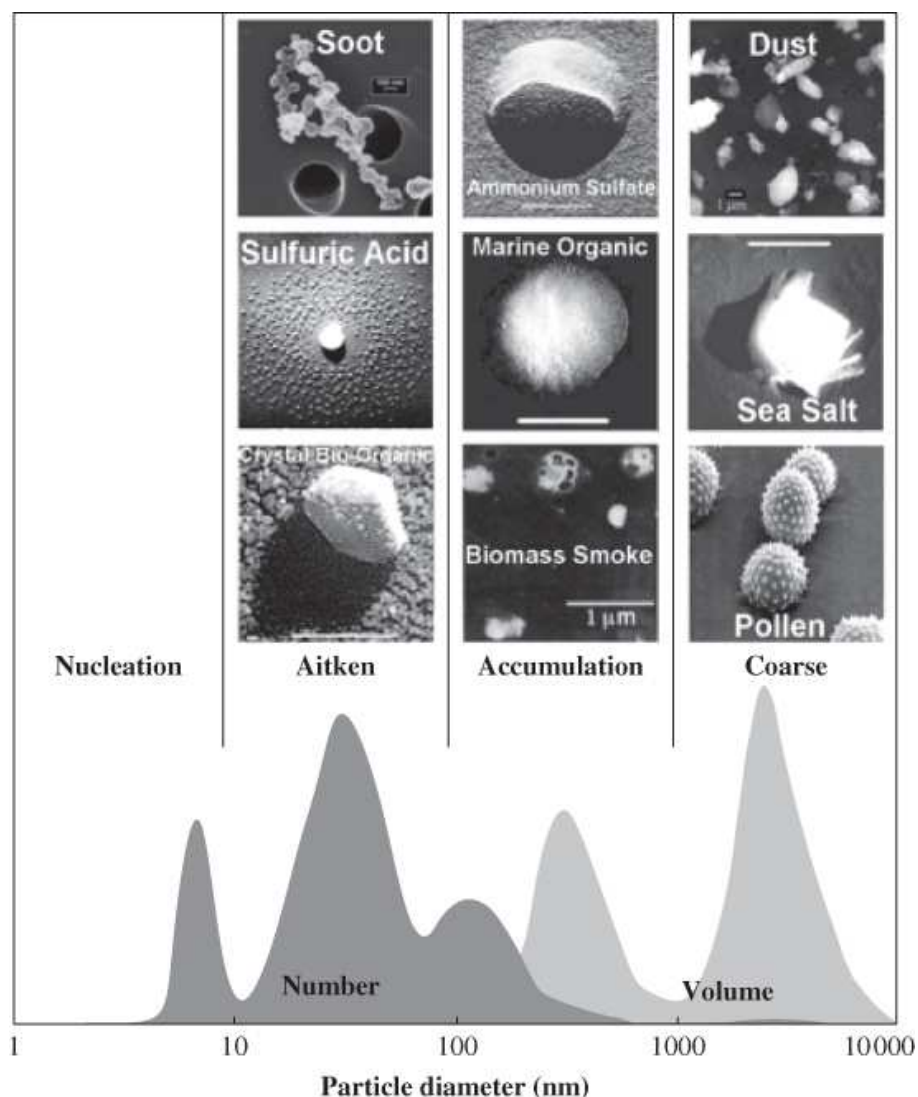


Figure 1.4: Aerosol size distribution and morphology for various aerosol types. [Colbeck et al., 2014]

particle shapes creates a difficulty to characterize their sizes. For spherical particles, the size is described directly by their radius or diameter. However, for particles which are not spherical, other parameters must be used such as their settling velocity. For example, the aerodynamic diameter of a non-spherical particle A is defined as the diameter that could have a spherical particle B of same settling velocity and density [Hinds, 2012]. Other definitions could be made based on other parameters such as volume or mass. However, the aerodynamic diameter is the most commonly used to describe particle sizes and it will be used in this thesis.

Determination of the aerosol size distribution is an important aspect of aerosol dynamics. A size distribution is the variation of concentration (i.e., number, surface area, volume, or mass of particles per unit volume of air) with size [Jacobson, 2002b]. Such distribution can be represented for example by the sum of log-normal modes with peaks of concentrations at different diameter ranges, such as a nucleation mode ($10^{-3} \mu\text{m} - 10^{-2}$

μm), an Aitken mode ($10^{-2} \mu\text{m} - 0.1 \mu\text{m}$), an accumulation mode ($0.1 \mu\text{m} - 1 \mu\text{m}$), and a coarse mode ($> 1 \mu\text{m}$).

Particles within the nucleation range are tiny particles created by nucleation. Through coagulation and condensation of gas, these particles increase in size and move into the Aitken and accumulation ranges. Particles of diameters within the Aitken and accumulation ranges are usually too light to be removed by gravity forces (i.e., sedimentation) or too large (for some of them) to be removed by diffusion (Brownian diffusion), so they can exist in the atmosphere for a relatively long period. Particles in this range require special attention, as they are the major force to affect health by penetrating deep into the lungs (see subsection 1.1.1). Besides, particles in this range are close in size to the wavelengths of visible light and, as a result, affect visibility (see subsection 1.1.2). Particles in the nucleation, Aitken and accumulation ranges are denoted as fine particles. The coarse range consists of particles of diameter larger than $2.5 \mu\text{m}$. Particles in this range are mostly of primary origins, i.e., directly emitted. Coarse particles are generally heavy enough to sediment out rapidly. As shown in Figure 1.4, the number concentration is usually dominated by nucleation and Aitken modes, while their contributions to the volume and mass distributions are small. On the contrary, with much lower number concentrations, accumulation and coarse particles dominate the volume and mass distributions.

1.2.3 Representation of the size distribution

The size distribution is often represented using a modal [Whitby and McMurry, 1997] or a sectional approach [Gelbard et al., 1980] or using the moment method [McGraw, 1997]. The modal and sectional approaches are now briefly explained. The sectional approach will be used in this study.

In the modal approach, the particle size distribution for number concentration n ($\# \text{m}^{-3}$) is expressed as a function of the particle diameter d_p . At a given time t , this function is described mathematically as the sum of x log-normal distributions:

$$n(\log d_p, t) = \sum_{i=1}^x \frac{N_i(t)}{\sqrt{2\pi} \log \sigma_i} \exp\left(-\frac{(\log d_p - \log \bar{d}_{pi})^2}{2 \log^2 \sigma_i}\right) \quad (1.1)$$

where i denotes the mode, $N_i(t)$ is the total particle number concentration, \bar{d}_{pi} is the geometric mean diameter, and σ_i the standard deviation of the log-normal mode i .

By assuming that all particles are spherical, the size distribution of the volume concentration v ($\mu\text{m}^3 \text{m}^{-3}$) can be deduced from the number concentration n :

$$v(\log d_p, t) = \frac{\pi}{6} d_p^3 n(\log d_p, t) \quad (1.2)$$

The size distribution of the mass concentration q ($\mu\text{g} \text{m}^{-3}$) can also be computed by assuming that all particles within a mode have the same density ρ_p ($\text{g} \text{cm}^{-3}$):

$$q(\log d_p, t) = \left(\frac{\rho_p}{10^6}\right) v(\log d_p, t) = \left(\frac{\rho_p}{10^6}\right) \frac{\pi}{6} d_p^3 n(\log d_p, t) \quad (1.3)$$

where the factor 10^6 is needed to convert the units of density ρ_p from $\text{g} \text{cm}^{-3}$ to $\mu\text{g} \mu\text{m}^{-3}$.

In the sectional approach, the particle size distribution is described by a sum of sections. Let us denote $n_i(d_p, t)$ and $q_i(d_p, t)$ the number and mass of particles of diameters ranging between d_p and $d_p + dd_p$. In each section i , the number $N_i(t)$ and the mass $Q_i(t)$ of particles are assumed to be constant:

$$N_i(t) = \int_{d_i^-}^{d_i^+} n_i(d_p, t) dd_p \quad (1.4)$$

$$Q_i(t) = \int_{d_i^-}^{d_i^+} q_i(d_p, t) dd_p = \frac{\pi}{6} \rho_i \int_{d_i^-}^{d_i^+} d_p^3 n_i(d_p, t) dd_p \quad (1.5)$$

where ρ_i is the density of particles, and d_i^- and d_i^+ are the lower and upper bounds of the section i . The diameter $d_{p,i}$ of particles in section i can be diagnosed using the relation

$$Q_i = \frac{\pi}{6} d_{p,i}^3 N_i \quad (1.6)$$

1.3 Mixing state of particles

Generally, the mixing state of particles defines the degree of mixing between the different chemical compounds of particles, i.e., how the chemical components are distributed among particles. At a given location, particles of different mixing states may co-exist. For example, let us assume that particles from a given origin have the same composition while particles from a different origin have a different composition. Then, when particles from these different origins meet together, if we let them co-exist and mix gradually by coagulation, condensation/evaporation, then in a given size range, particle may have different chemical compositions, as shown in Figure 1.5 (b), and particles are said to be externally mixed. Alternatively, if in a given size range, particles are assumed to have a homogeneous composition, then they are said to be internally mixed (see Figure 1.5 (a)).

In the real world, externally-mixed aerosols may be observed near emission sources. Interactions between newly emitted particles and background aerosols and gas molecules change the original composition of those particles, such process is known as particle ageing. As particles age, they may lose their original identities and they may reach the same composition as background aerosols, that is to say they become internally mixed. However, completely externally or internally mixed particles probably rarely exist. The mixture is likely to be something in between, i.e., an aerosol population consisting of an external mixture of internally-mixed particles but with varying compositions. Figure 1.6 shows one of the attempt to classify measured tropospheric aerosols according to their compositions made by Murphy et al. [2006]: a wide range of aerosol compositions can coexist in the atmosphere, including pure sulphate particles, pure organic particles, and mixed particles of various degrees.

Information on the mixing state of particles is very important. First, the particle mixing state can provide essential information about source appointment and particle ageing process. Second, the mixing state influences particle composition, hence particle properties. For example, if particles from source A consist of pure black carbon (EC), which is a strong absorber of sunlight but hostile to water vapour, come in contact with

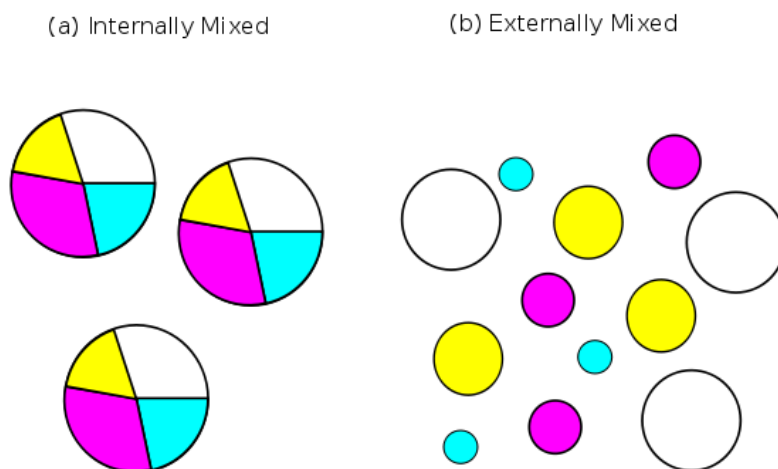


Figure 1.5: Illustration of (a) a group of internally mixed particles and (b) a group of externally mixed particles

hydrophilic particles of ammonium-sulphate ($(\text{NH}_4)_2\text{SO}_4$), the properties of EC particles may change as they mix with the other particles. A coating layer of $(\text{NH}_4)_2\text{SO}_4$ could be formed upon the surface of EC particles, due to condensation or coagulation. The resulting particles would be more easily activated as a cloud condensation nuclei than EC particles. Such mixing would also modify particle's optical properties as well. The mixing may reduce the absorption ability of EC particles, while the scattering capability may be strengthened as $(\text{NH}_4)_2\text{SO}_4$ has a high scattering coefficient.

In order to investigate the importance of aerosol mixing state, field studies have been conducted. The evolution of the aerosol mixing state from Long Beach to Riverside, CA was observed by Hughes et al. [2000], where initially externally mixed sea-salt and primary carbon particles undergo substantial changes of chemical composition during transport by condensation of ammonium nitrate and organics. Mallet et al. [2004] found that the observed aerosol optical properties have a better coherence with reconstructed values under the assumption of an external mixture between EC and other particles. The mixing state of mineral dust from western Sahara was investigated during the African Monsoon Multidisciplinary Analysis project (AMMA) by Deboudt et al. [2010b]. Mineral dust and carbonaceous and marine compounds were predominantly found externally mixed. During the MEGAPOLI ¹ campaign, Healy et al. [2012], Healy et al. [2013] and Healy et al. [2014] conducted a series of studies on the mixing state of carbonaceous particles. A bimodal distribution of elemental carbon (EC) particles was observed, where particles of the smaller mode were mostly externally-mixed and locally emitted, while particles from the larger mode were associated with continental transport event and mostly internally mixed with OM and nitrate. The diurnal evolution and source identification of aerosols at a continental regional background site in Italy was investigated by Decesari et al. [2014] based on observed aerosol composition and mixing state, where the mixing

¹Megacities: emissions, urban, regional and Global Atmospheric POLLution and climate effects, and Integrated tools for assessment and mitigation

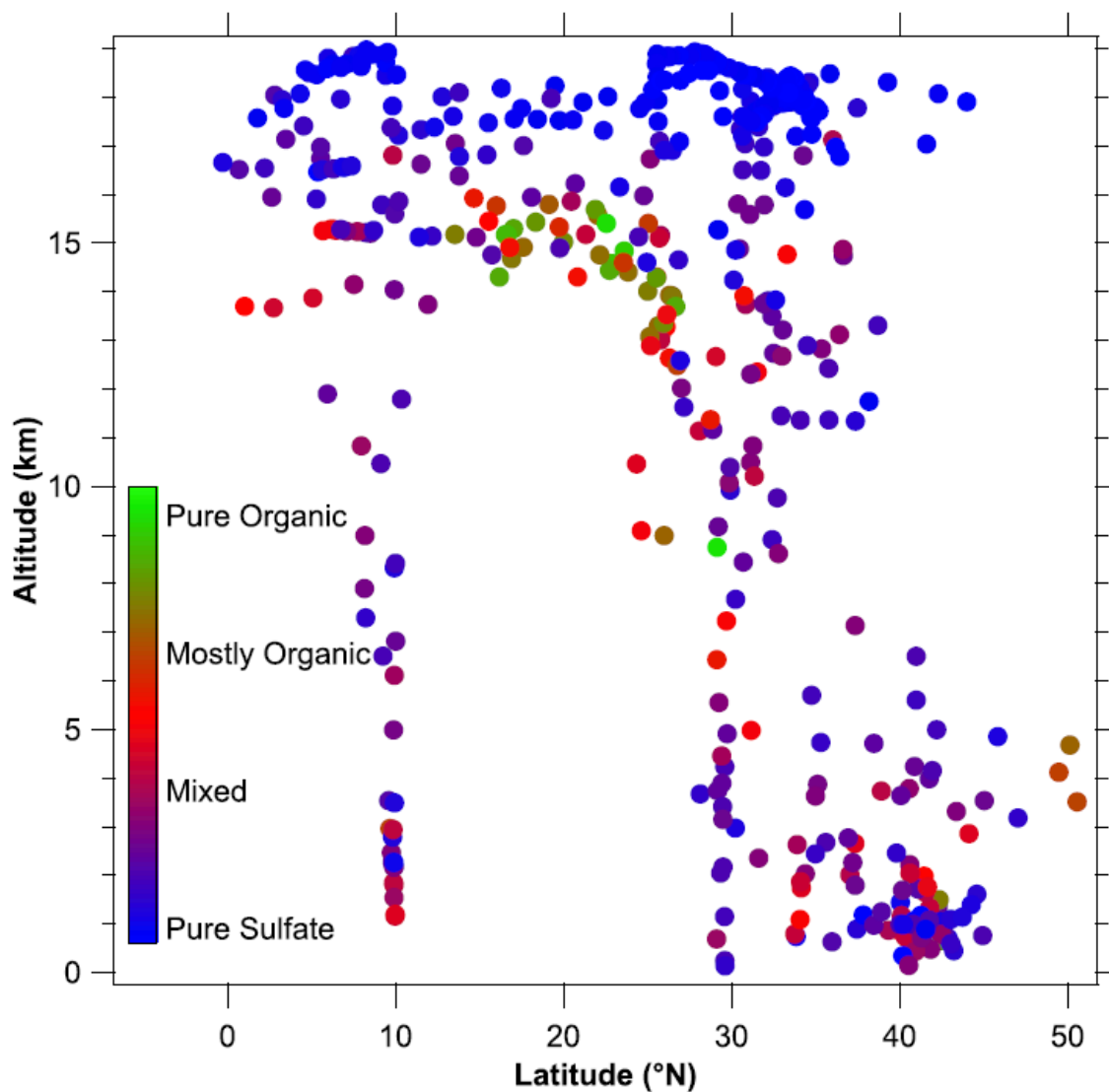


Figure 1.6: An altitude-latitude distribution of observed tropospheric aerosols and their mixing states [Murphy et al., 2006]

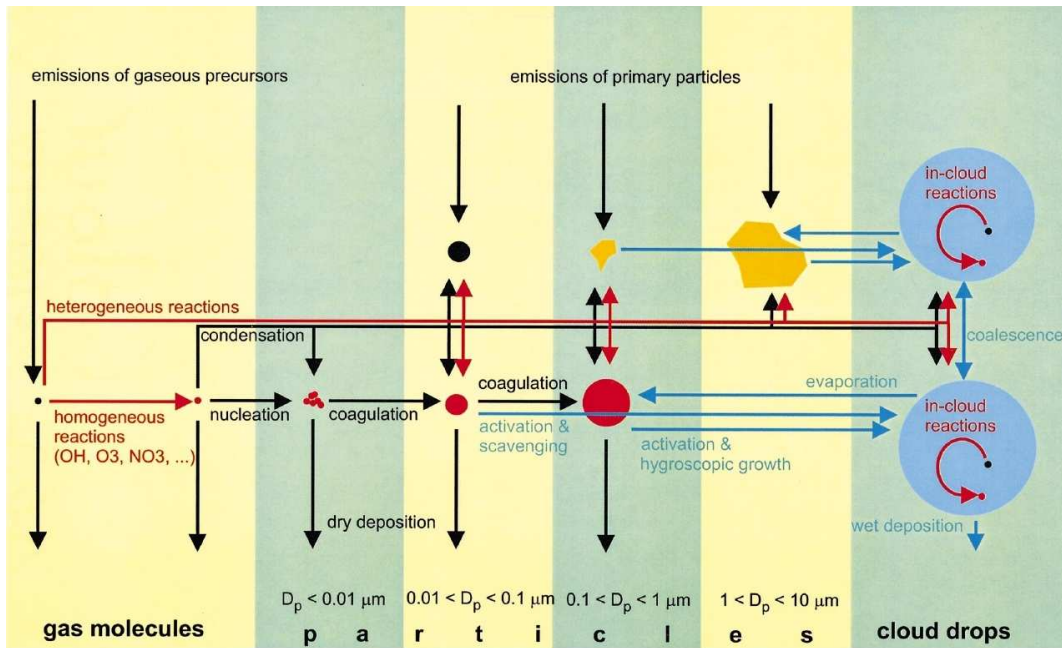


Figure 1.7: Scheme of aerosol dynamics processes. [Raes et al., 2000]

state of EC was found strongly related to the meteorological regimes (enhanced stagnation or enhanced ventilation). Leck and Svensson [2015] revealed the importance of aerosol composition and mixing state for CCN activation based on their observation and numerical reconstruction in the high Arctic. Fitzgerald et al. [2015] compared the mixing state between long-range transported Asian and African mineral dust. They found that Asian dust was better mixed with anthropogenic pollutants and more aged than African dust, which makes Asian dust a better candidate for CCN activation than the fresher African dust.

The particle mixing state is controlled by several aerosol dynamic processes which are addressed in the following section.

1.4 Aerosol dynamics

In the atmosphere, the size, the concentration and chemical composition of particles are constantly evolving with time as a result of many processes: transport (advection, diffusion), deposition (sedimentation, dry deposition, wet deposition), processes related to aerosol dynamics (nucleation, coagulation, condensation and evaporation), and processes related to the activation of particles into cloud droplets, see figure 1.7. Here, we focus on processes related to aerosol dynamics.

1.4.1 Nucleation

Homogeneous nucleation happens when a gaseous precursor is transformed to particle mass without a pre-existing particle surface. It generates unmixed particles into the atmosphere.

Nucleation requires a high supersaturation of precursor gases. Supersaturation occurs when a chemical compound has a higher partial pressure than the saturation vapour pressure of that compound. In the atmosphere, several processes can lead to such a state of supersaturation [Raes et al., 2000]:

1. Gas-phase chemical reactions leading to an increase in the gas-phase concentration of compounds with low saturation vapour pressure, such as sulfuric acid.
2. The decrease of ambient temperature leading to lower saturation vapour pressure of precursor gases.
3. The formation of additional vapour to the system may lower the saturation pressure of pre-existing compounds.

Under supersaturation conditions, some gas molecules may form small clusters. However, as the equilibrium vapour pressure over a spherical particle increases with increasing curvature of the particle (Kelvin effect), most of those small clusters generally evaporate. Only clusters exceeding a critical size can escape the evaporation fate and are able to grow rapidly to form stable particles. So the nucleation rate is defined as the net number of clusters per unit time that grow past a critical size [Seinfeld and Pandis, 2006].

Generally, homogeneous nucleation happens between two or more species rather than a single compound, as the necessary saturation pressure to induce nucleation is much lower for a mixed vapour than for each of its pure substance. An important binary nucleation system in the atmosphere is that of sulphuric acid and water [Doyle, 1961]. Other nucleation mechanisms that have been investigated include: sulphuric acid-ammonia-water ternary nucleation [Kulmala et al., 2000], ion-induced nucleation [Yu and Turco, 2000] and nucleation of organic vapours [Hoffmann et al., 1997].

New particles created by nucleation, may grow into microscopic size (around 0.001 μm). Nucleation originated particles may slowly grow into size larger than 0.1 μm within several days under general atmospheric conditions. However, such growth can occur within 24 hours under polluted, urban type conditions [Raes et al., 2000].

1.4.2 Coagulation

Coagulation happens when two particles collide together to form a new particle. Such collision is mostly caused by their Brownian motion. The Brownian motion is caused by the random collision of quickly moving gas molecules around particles due to their thermal motions. As a result, Brownian coagulation is often referred as thermal coagulation. Coagulation may significantly reduce particle number concentrations, while it has no effect on total particle mass concentration. Generally, coagulation is particularly efficient at mixing ultra-fine particles, as they tend to have high number concentrations increasing their collision probabilities. Beside, ultra-fine particles are more affected by Brownian motion than fine or coarse particles, which makes them more likely to collide between themselves than the coarse ones.

A key parameter to model the dynamic of coagulation is the Knudsen number:

$$K_n = \frac{2 \lambda}{d_p} \quad (1.7)$$

with λ is the mean free path of surrounding gas and d_p the particle diameter. The Knudsen number defines three different dynamical regimes that govern the behaviour of aerosols and their coagulation coefficient [Seinfeld and Pandis, 2006]:

1. Free molecular regime, $K_n \gg 1$. In this regime, particles behave similarly to gas molecules, as their diameters are relatively low compared to the mean free path of gas molecules. The coagulation coefficient between two particles within the free molecular regime is defined as follows:

$$K_{12}^f = \frac{\pi}{4}(d_{p1} + d_{p2})^2(\bar{c}_1^2 + \bar{c}_2^2)^{1/2} \quad (1.8)$$

where d_{pi} and \bar{c}_i are particle mean diameter and average thermal velocity respectively.

2. Continuum regime, $K_n \ll 1$. In this regime, surrounding gas molecules act as a continuous fluid flowing round the particles, as particle diameters are much larger than the free mean path of gas molecules. The coagulation coefficient in this regime is as follows:

$$K_{12}^c = 2\pi(d_{p1} + d_{p2})(D_1 + D_2) \quad (1.9)$$

where D_i is the diffusion coefficient.

3. Transition regime, $K_n \approx 1$. This regime includes all the particles between the free molecular and continuum regimes. They are influenced by a complex combination of macroscopic forces and microscopic interactions with gas molecules. The coagulation coefficient in this regime equals to the coefficient of continuum regime corrected by a factor β :

$$K_{12}^t = 2\pi(d_{p1} + d_{p2})^2(D_1 + D_2)\beta \quad (1.10)$$

$$\beta = \frac{d_{p1} + d_{p2}}{d_{p1} + d_{p2} + 2(g_1^2 + g_2^2)^{1/2}} + \frac{8(D_1 + D_2)}{(\bar{c}_1^2 + \bar{c}_2^2)^{1/2}(d_{p1} + d_{p2})} \quad (1.11)$$

with:

$$g_i = \frac{1}{3d_{pi}l_i}[(d_{pi} + l_i)^3 - (d_{pi}^2 + l_i^2)^{3/2}] - d_{pi}, \quad l_i = \frac{8D_i}{\pi\bar{c}_i} \quad (1.12)$$

1.4.3 Condensation and evaporation

Generally, particles constantly interact with surrounding gas, which can either condense or evaporate from the particle surface. Such interactions between gas and particles are controlled by the difference between the vapour pressure of the gas and its equilibrium vapour pressure at the particle surface. When the vapour pressure is higher than the surface equilibrium pressure, molecules go from the gas phase into the particle phase and

cause particle growth (condensation). On the contrary, when the vapour pressure is lower than the surface equilibrium pressure, evaporation occurs and particles shrink.

According to [Seinfeld and Pandis, 2006], the mass changing rate of a particle with diameter d_p as a result of condensation/evaporation of species i between the gas and particle phases can be described by:

$$I_i = \frac{dm_i}{dt} = \frac{2\pi d_p D_i M_i}{RT} f(K_n, \alpha_i) (p_i - p_i^{eq}) \quad (1.13)$$

where T is the temperature, R is the ideal gas constant, D_i represents the diffusion coefficient of species i in air, M_i is its molecular weight, and $f(K_n, \alpha)$ is a correction factor due to non-continuum effect and imperfect surface accommodation (α_i) [Dahneke, 1983]:

$$f(K_n, \alpha_i) = \frac{1 + K_n}{1 + 2K_n(1 + K_n)/\alpha_i} \quad (1.14)$$

The last term on the right hand side of equation (1.13) represent the driving force of condensation and evaporation as p_i is the vapour pressure and p_i^{eq} is the equilibrium vapour pressure. Based on the ideal gas law, equation (1.13) can also be expressed by the difference between the gas concentration c_i and the local equilibrium concentration c_i^{eq} :

$$I_i = \frac{dm_i}{dt} = 2\pi d_p D_i f(K_n, \alpha_i) (c_i - K_e(d_p) c_i^{eq}) \quad (1.15)$$

where $K_e(d_p)$ models the Kelvin effect which describes the influence of particle curvature on equilibrium vapour pressure (the vapour pressure of a curved surface is higher than a flat surface):

$$K_e(d_p) = \exp\left(\frac{4\sigma v_p}{RT d_p}\right) \quad (1.16)$$

with σ the particle surface tension and v_p the particle molar volume.

In opposite to coagulation, condensation and evaporation do not influence particle number, but they can significantly modify particle mass concentration as well as their chemical composition. Actually, the most abundant condensing gas is water vapour. Under high relative humidity, the condensation of water vapour can lead to a significant growth of particle wet diameter and activates it into a cloud droplet. The original particle is then referred to as a cloud condensation nuclei. Sulphuric acid gas, with extremely low surface equilibrium vapour pressure, is another important condensible gas. Once condensed, sulphuric acid rarely evaporates as its $p_i^{eq} \approx 0$. Other condensible species include nitric acid, ammonia, hydrogen chloride and semi-volatile organic species. Condensation is responsible for the formation of coating layers observed in many particles [Levin et al., 1996; Deboudt et al., 2010b]. One classical case of particle composition variation due to condensation and evaporation is the chloride depletion in sea salt particles when hydrogen chloride evaporates while nitric acid or sulfuric acid condense [McInnes et al., 1994].

1.4.4 General dynamic equation

The general dynamic equation (GDE) describes the time evolution of aerosol populations caused by the aerosol dynamic processes mentioned in former sections. The GDE has a fundamental importance in understanding and modelling aerosol dynamic processes.

Depending on whether the aerosol size distribution is represented as discrete or continuous and what physical and chemical phenomena are included, GDE can exist in many forms [Gelbard and Seinfeld, 1979]. Here, we represent the GDE in form of continuous number and mass distributions with nucleation, coagulation and condensation/evaporation(c/e) processes.

First, the particle size distribution at a given time t can be described by a continuous density function of particle number: $n(m, t)$, with $n(m, t)dm$ ($\# \text{ m}^{-3}$) representing the number concentration between m and $m+dm$, where m corresponds to the signal particle mass at a given size d_p . Similarly, the mass distribution of a species X_i can be described by $q_i(m, t)$, with $q_i(m, t)dm$ ($\mu\text{g m}^{-3}$) representing the mass concentration of X_i between m and $m+dm$. Under such assumption, the mass of X_i within particles can be determined by:

$$m_i(m, t) = \frac{q_i(m, t)}{n(m, t)} \quad (1.17)$$

While the total mass distribution can be expressed as:

$$q(m, t) = \sum_{i=0}^s q_i(m, t) = m n(m, t) \quad (1.18)$$

where s is the total number of species within the particle.

Based on the former assumptions, the GDE for number distribution can be expressed as follows:

$$\begin{aligned} \frac{\partial n}{\partial t}(m, t) = & \frac{1}{2} \underbrace{\int_{m_0}^{m-m_0} K(u, m-u)n(u, t)n(m-u, t)du}_{\text{coagulation gain}} \\ & - \underbrace{n(m, t) \int_{m_0}^{\infty} K(m, u)n(u, t)du}_{\text{coagulation loss}} \\ & - \underbrace{\frac{\partial(I_0 n)}{\partial m}}_{\text{c/e size advection}} + \underbrace{\delta(m, m_0)J_0(t)}_{\text{nucleation}} \end{aligned} \quad (1.19)$$

Here, the smallest particle mass is defined by m_0 , which corresponds to the mass of fresh particles generated by nucleation. The $K(u, v)$, expressed in $\text{m}^3 \cdot \text{s}^{-1}$, represent the coagulation coefficient between two particles of mass u and v . As discussed in section 1.4.2, the K value varies with the particle dynamical regimes and can be computed based on equations (1.8) to (1.10). The term $I_0(m, t)$ represents the particle growing rate due to c/e process, expressed in $\mu\text{g s}^{-1}$. Although the total number is not influenced by c/e process, the term $\frac{\partial(I_0 n)}{\partial m}$ represents the fact that the particle number distribution is shifted toward higher or lower mass regimes by c/e, due to their size evolution. Finally, the term $J_0(t)$ represent the nucleation rate, in $\# \text{ m}^{-3} \text{ s}^{-1}$, that is the number of particles created by nucleation within a unit volume of a unit time. The $\delta(m, m_0)$ is a Dirac function at m_0 , which limits the mass (and therefore size) of nucleated particles to particles of mass m_0 .

Similarly, the GDE for mass distribution of species X_i can be described as follows:

$$\begin{aligned}
\frac{\partial q_i}{\partial t}(m, t) = & \underbrace{\frac{1}{2} \int_{m_0}^{m-m_0} K(u, m-u) q_i(u, t) n(m-u, t) du}_{\text{coagulation gain}} \\
& - \underbrace{q_i(m, t) \int_{m_0}^{\infty} K(m, u) n(u, t) du}_{\text{coagulation loss}} \\
& - \underbrace{\frac{\partial(I_0 q_i)}{\partial m}}_{\text{c/e size advection}} + \underbrace{(I_i n)(m, t)}_{\text{c/e transport of } X_i} + \underbrace{\delta(m, m_0) J_0(t) m_i}_{\text{nucleation}}
\end{aligned} \tag{1.20}$$

The new term $(I_i n)(m, t)$ corresponds to the gain or lost of species X_i for the particle of mass m by condensation/evaporation. I_i is the mass transfer rate between the gas and aerosol phase as described in equation (1.15) and $I_0 = \sum_{i=0}^s I_i$.

1.5 Air quality modelling

1.5.1 Chemical transport models

A chemical transport model (CTM) is designed to investigate the evolution of chemical concentrations, including gas, particles, ice and water droplets, over predefined spatial scales, such as local, continental or global. Such evolution is related to multiple processes including emissions, meteorology, physico-chemical transformations, transport and removal processes. All those processes are usually included in CTMs as detailed in figure 1.8. A wide variety of CTMs have been developed since 1970s for air quality impact and scenario studies [Seinfeld, 2004]. They can be classified depending on whether or not they compute meteorology: in on-line models, such as WRF-CHEM [Grell et al., 2005], meteorological fields are computed in the CTM, whereas in off-line models, such as CMAQ [Byun and Schere, 2006], POLYPHEMUS [Sartelet et al., 2007] or CHIMERE [Schmidt et al., 2001], meteorology is an input data of the model. Off-line models do not allow to model the interactions between aerosols and meteorology, but they have shorter computational times than on-line models. This thesis focuses on off-line models.

The following equation describes the time evolutions of chemical concentrations which are solved in off-line CTMs [Seinfeld and Pandis, 2006]:

$$\frac{\partial c_i}{\partial t} = \left(\frac{\partial c_i}{\partial t}\right)_{adv} + \left(\frac{\partial c_i}{\partial t}\right)_{dif} + \left(\frac{\partial c_i}{\partial t}\right)_{cloud} + \left(\frac{\partial c_i}{\partial t}\right)_{dry} + \left(\frac{\partial c_i}{\partial t}\right)_{aeros} + R_{gi} + E_i \tag{1.21}$$

where c_i represents the concentration of species i ; $(\partial c_i / \partial t)_{adv} = \text{div}(V c_i)$ represents the time derivative of c_i due to advection, which can be express as a function of the wind velocity V ; $(\partial c_i / \partial t)_{dif}$ represents the time derivative of c_i due to diffusion; $(\partial c_i / \partial t)_{cloud}$ represents the influence of cloud processes including cloud scavenging, evaporation of cloud droplets, aqueous-phase reactions, wet deposition; the dry deposition due to gravitational sedimentation or interception is described by the term $(\partial c_i / \partial t)_{dry}$. Besides, aerosol processes (exchange between gas and particle phases, aerosol dynamics, etc.) is

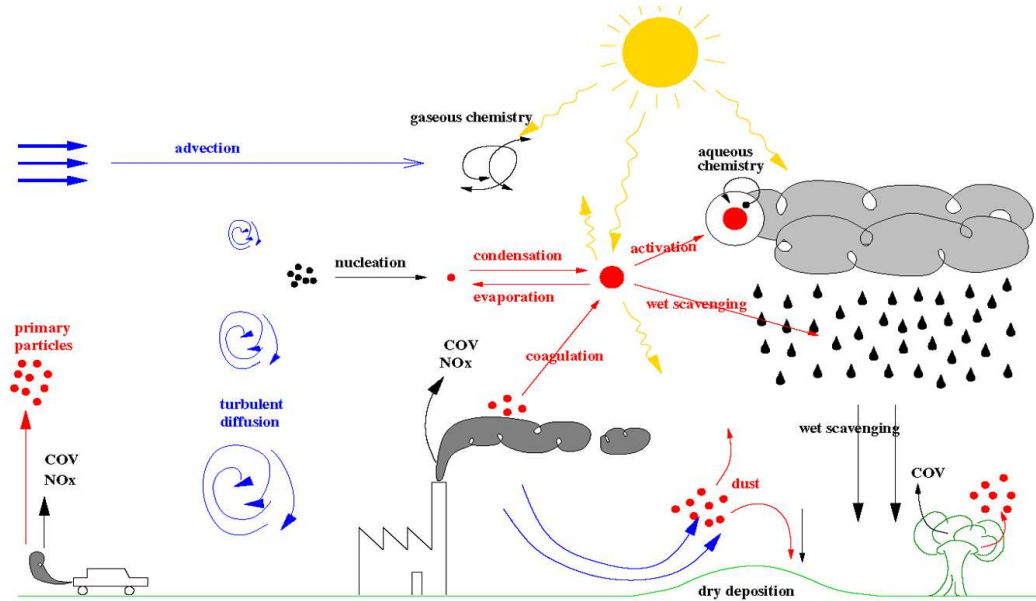


Figure 1.8: Processes described in CTMs. [Sportisse, 2008]

represented by $(\partial c_i / \partial t)_{aeros}$. Finally, R_{gi} is the net production from gas-phase reactions and E_i is the emission rate.

Thanks to the rapid advancement of computational abilities, CTMs are able to include more and more atmospheric processes as well as more detailed parametrizations. The Polyphemus air-quality platform [Mallet et al., 2007] includes a CTM and it is capable of implementing some advanced methods such as model coupling and data assimilation [Wang et al., 2013]. It is the hosting platform of the aerosol model developed in this thesis. The overall architecture of Polyphemus is now described.

In Polyphemus, an air quality simulation is conducted in three steps. First, as an off-line model, large amount of initial data is generated within the preprocessing step, including land-use informations, meteorological data, initial and boundary conditions, and emission inventories. The second part is the processing step, where numerical models (e.g., the Eulerian chemistry-transport model) solve the time integration of equation (1.21). During the simulation, concentrations at each simulation time step can be saved. A driver component is designed as a shell to manage numerical models and provides a possible interface for data assimilation and other high-level methods. Finally, concentrations and aerosol optical depths can be compared and analysed by Python scripts or additional programs contained in the post-processing component.

Several numerical models are available in the processing part, including Gaussian and Eulerian models. Here, the chemistry transport model Polair3D [Sartelet et al., 2007] is used. In the Polair3D/Polyphemus model, processes described in equation (1.21) are split and solved in a sequential way. Let Δt be the splitting time step, then at each time t , the splitting is performed in the following order: advection, diffusion, gas-phase chemistry, particle or cloud processes.

The advantage of using Polair3D is that it is well structured and very flexible to new solvers. Actually, most of processes within Polair3D is solved by independent modules, and it is easy to switch between different numerical methods/parameterizations. For ex-

ample, for the advection and diffusion, several transport modules have been developed with different numerical integration methods; for the gas-phase chemistry, multiple chemical mechanisms can be used such as RACM [Stockwell et al., 1997], RACM2 [Goliff and Stockwell, 2008] and CB05 [Yarwood et al., 2005]. Particles are solved using the sectional model SIREAM [Debry et al., 2007b]. The aerosol model developed in this thesis is integrated into Polair3D as an alternative of SIREAM.

1.5.2 Aerosol modelling

Since the early 1980s, efforts have been made to model aerosol dynamic processes in 3-D CTMs [Gelbard and Seinfeld, 1980]. Most of the existing aerosol models can be classified into two types based on the approach used to represent the particle size distribution: a modal approach (e.g., [Whitby and McMurry, 1997]; [Binkowski and Roselle, 2003]; [Sartelet et al., 2006]), where the overall size distribution is represented by a sum of log-normal modes, a sectional or size-resolved approach (e.g., [Gelbard et al., 1980]; [Zhang et al., 2004]; [Debry et al., 2007b]), where the overall size distribution is represented by a discrete number of size sections. One advantage of modal models is that they generally need less computational resources, as they use a limited number of modes. However, their abilities to represent the evolution of the size distribution may be more limited than sectional models [Mann et al., 2012], partly because of the difficulties associated to the modelling of the Kelvin effect [Devilliers et al., 2012]. The sectional model used in Polair3D/Polyphemus is SIREAM [Debry et al., 2007b]. Like most of current aerosol models, SIREAM assumes that particles are internally mixed. The internal-mixing assumption assumes that particles from different origins, but same size section, mix instantaneously when they meet: all particles within one size section are considered to have a homogeneous composition. However, as discussed in section 1.3, particles with different compositions may coexist in the atmosphere. In reality, only very aged particles may reach an homogeneous composition and can be considered as internally mixed. However, close to emission sources, particles are more likely to be externally mixed. The internal-mixing assumption requires less computational resources, but valuable information about particle origins as well as their mixing states is lost. Furthermore, the mixing state of particles could influence particle properties and their chemical evolutions. Thus, alternative schemes, which can represent multiple particle compositions within one size section, have been proposed and they are referred to as external-mixing models. A source-oriented model was developed by Kleeman et al. [1997] and Kleeman and Cass [2001] for regional modelling. In these models, each source is associated with a specific aerosol population, which may evolve in terms of size distribution and chemical composition, but does not mix with the other sources (i.e., particle coagulation is neglected). Riemer et al. [2009] modelled externally-mixed particles using a stochastic approach. However, such an approach is computationally expensive when the number of particle species is high. On the other hand, Stier et al. [2005] and Bauer et al. [2008] simulated externally mixed particles using modal aerosol models, where aerosol populations with different mixing states are represented by modes of different compositions (soluble/mixed or insoluble/not mixed). Although these models may be computationally efficient, they may not model accurately the dynamics of mixing. To represent externally-mixed particles independently of their sources and number concentrations, Jacobson et al. [1994] and Lu and Bowman [2010]

considered particles that can be either internally- or externally-mixed (i.e., composed of a pure chemical species). Lu and Bowman [2010] used a threshold mass fraction to define whether the species is of significant concentration. Jacobson [2002a] expanded on Jacobson et al. [1994] by allowing particles to have different mass fractions. Similarly, Oshima et al. [2009b] discretised the fraction of black carbon in the total particle mass into sections of different chemical compositions.

Dergaoui et al. [2013] further expanded on these modelling approaches by discretising the mass fraction of chemical species into sections, as well as the size distribution. For each size section, the mass fraction of each species is discretised into sections $F_{h-}^+ = [F_h^-, F_h^+]$ (h varies from 1 to the number of mass fraction sections n_f with $F_1^- = 0$, $F_{n_f}^- = 1$ and $F_h^- = F_{h-1}^+$), leading to a variety of possible particle compositions. Assuming that it is possible to have up to c chemical species in particles, let us denote f_i the mass fraction of species X_i ($1 \leq i \leq c$). Each particle is associated with a mass fraction vector $\vec{f} = (f_1, f_2, \dots, f_{(c-1)})$, which defines the particle composition/ $\vec{P}_g = (F_{g1-}^+, F_{g2-}^+, \dots, F_{g(c-1)-}^+)$ with $f_i \in F_{g_i-}^+$. For a particle composition to be valid, $\sum_{i=1}^{(c-1)} F_{g_i-}^+ \leq 1$ must be satisfied. Note that f_c is not specified because it is constrained by mass conservation ($f_c = 1 - \sum_{i=1}^{(c-1)} f_i$). Based on this discretization, Dergaoui et al. [2013] derived the equation for coagulation and validated their model by comparing the results obtained for internal and external mixing. However, processes such as condensation/evaporation and nucleation were not modelled.

1.5.3 Model performance evaluation

In order to assess the reliability of model simulations, it is necessary to have appropriate methods and criteria to evaluate the model performance. Doll [1991] and Russell and Dennis [2000] recommended to use the mean normalised bias error (MNBE) and the mean normalised gross error (MNGE) as the key statistics to evaluate simulated chemical concentrations (e.g., ozone) with observational data:

$$MNBE = \frac{1}{N} \sum_{i=1}^n \frac{s_i - o_i}{o_i} \quad (1.22)$$

$$MNGE = \frac{1}{N} \sum_{i=1}^n \frac{|s_i - o_i|}{o_i} \quad (1.23)$$

where n is the number of available observations, while s_i ($i=1, n$) and o_i ($i=1, n$) are the simulated and observed values, respectively. The suggested performance criteria is $MNBE \leq 15\%$ and $MNGE \leq 30\%$.

However, Seigneur et al. [2000] pointed out that using normalized error and bias may cause misleading conclusions about the model performance, as the error may be artificially high in case of over predictions (no limits) compared to the under-predictions case (limited by -1). So they suggested to use fractional error and bias for the statistical evaluations. The mean fractional bias MFB (%) and the mean fractional error MFE (%) are defined as follows:

$$MFB = \frac{1}{N} \sum_{i=1}^n \frac{s_i - o_i}{(s_i + o_i)/2} \quad (1.24)$$

$$MFE = \frac{1}{N} \sum_{i=1}^n \frac{|s_i - o_i|}{(s_i + o_i)/2} \quad (1.25)$$

Based upon an analysis of numerous PM modelling studies, Boylan and Russell [2006] proposed a PM model performance goal and criterion. The model performance goal is considered as the level of accuracy which is expected to be achieved by the best models. The model performance criterion corresponds to the level of accuracy that is considered to be acceptable for modelling applications, such as forecast of pollutants and regulatory applications. The criteria to meet the performance goal is defined as MFB in the range of [30 %, 30 %] and MFE in the range [0 %, 50 %]. If both the MFB and MFE are in the range [60 %, 60 %] and [0 %, 75 %] respectively, the model performance criterion is met.

In addition, other statistical measures such as the root mean square error (RMSE) and the (Pearson) correlation can also be helpful for the performance evaluation. The RMSE is defined as the square of the deviation of the model from observations. It is defined as follows:

$$RMSE = \sqrt{\frac{1}{N} \sum_{i=1}^n (o_i - s_i)^2} \quad (1.26)$$

The correlation can be computed with the following equation:

$$correlation = \frac{\sum_{i=1}^n (o_i - \bar{o})(s_i - \bar{s})}{\sqrt{\sum_{i=1}^n (o_i - \bar{o})^2 \sum_{i=1}^n (s_i - \bar{s})^2}} \quad (1.27)$$

with \bar{s} and \bar{o} the arithmetic averages of all simulated and observed values respectively.

1.6 Objectives and plan of thesis

This work presents an externally-mixed model that takes into account all the known processes related to aerosol dynamic and that can be used for air-quality simulations. The discretization scheme of Dergaoui et al. [2013] is used as it discretizes both the size and the composition distributions. The model developed by Dergaoui et al. [2013] takes into account coagulation. It is further developed to take into account condensation/evaporation and nucleation processes. The model is then integrated into the Polyphemus platform and its performance is evaluated through 3 Dimension (3-D) simulations and comparisons, with observations. This work aims at improving our understanding of mixing processes between different particle populations, as well as the influence of the mixing-state assumption on particle concentrations and properties, such as optical and hygroscopic properties. This thesis is organised as follows.

In chapter 2, the methodology and numerical structure of the Size-Composition Resolved Aerosol Model (SCRAM) is presented. The model is first validated by comparison with a reference solution and with results of simulations for internally-mixed particles. The degree of mixing of particles is investigated in a box model simulation using data representative of air pollution in Greater Paris. The relative influence of the different aerosol processes on the mixing state and of the algorithm used to model condensation/evaporation is studied.

In chapter 3, the ability of SCRAM to simulate externally-mixed particles in a 3-D environment is investigated, by integrating SCRAM into the Polyphemus air-quality

modelling platform. Simulation results with different mixing-state assumptions as well as different condensation/evaporation solvers are presented. The model performance to simulate $\text{PM}_{2.5}$, PM_{10} and aerosol optical depths are evaluated through comparisons between simulation results and observations. Besides, the evolution and the spatial distribution of the mixing state of black carbon (EC) particles are investigated. Furthermore, the influence of the mixing-state assumption on particles optical properties and on the formation of cloud condensation nuclei is studied.

In chapter 4, simulations are conducted during January 2010 where the compositions of individual particles were measured during the winter campaign of Megapoli. The simulation of both bulk concentrations of chemical species and the concentrations of individual particle classes are compared with the observations of [Healy et al., 2012]. Then, the single particle diversity and the mixing-state index are computed based on the quantification approach developed by [Riemer and West, 2013], and compared with the observation based analyses of [Healy et al., 2014].

Finally, in Chapter 5, we summarize the results found in the previous chapters and give conclusions of this work. This chapter also describes possible future directions and perspectives on the basis of the present simulation results.

Chapter 2

A size-composition resolved aerosol model for simulating the dynamics of externally-mixed particles: SCRAM (v 1.0)

Résumé

Ce chapitre présente un nouveau modèle SCRAM (Size and Composition Resolved Aerosol Model) pour simuler la dynamique des particules dans l'atmosphère (nucléation, coagulation, condensation / évaporation) en prenant en compte leur état de mélange. Le modèle SCRAM est un modèle 0-D basé sur le schéma de discrétisation défini par Dergaoui et al. [2013], où les particules sont classées à la fois selon leurs tailles et leurs compositions. Pour définir les compositions, on discrétise d'abord en sections les fractions massiques de composés chimiques des particules ou d'ensembles de composés chimiques. Les compositions des particules sont ensuite définies par les combinaisons des sections de fractions massiques. Les trois processus principaux impliqués dans la dynamique des aérosols (la coagulation, la condensation / évaporation et la nucléation) sont inclus dans SCRAM. SCRAM est validé par comparaison avec des simulations « académiques » publiées dans la littérature de coagulation et condensation/évaporation pour des particules en mélange interne. L'impact de l'hypothèse de mélange externe pour ces simulations est notamment étudié. L'impact du degré de mélange sur les concentrations de particules est ensuite étudié dans une simulation 0-D en utilisant des données représentatives d'un site trafic en Ile de France. L'influence relative sur l'état de mélange des différents processus influençant la dynamique des particules (condensation / évaporation, coagulation) et de l'algorithme utilisé pour modéliser la condensation / évaporation (hypothèse d'équilibre entre les phases gazeuse et particulaire, ou bien modélisation dynamique des échanges gaz/particules) est étudiée. Pour le moment, SCRAM ne peut modéliser dynamiquement les échanges gaz/particules que pour les composés inorganiques. Dans le cas étudié, on constate que la coagulation est très efficace à mélanger les particules (le pourcentage des concentrations en nombre et en masse des particules mélangées diminue lorsque la coagulation n'est pas prise en compte dans la simulation). La condensation peut éventuellement diminuer le pourcentage de particules mélangées, quand une grosse quantité de gaz peu

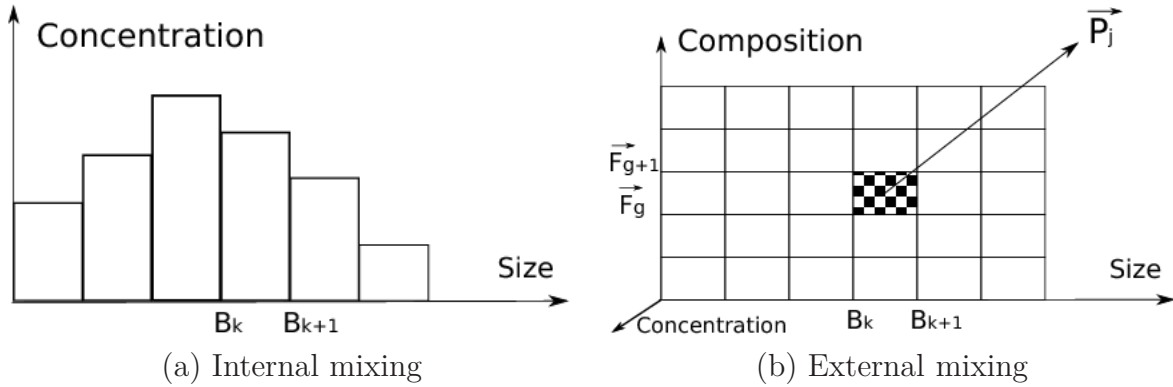


Figure 2.1: Particle discretization schemes used in internal (a) and external (b) mixing aerosol models.

volatiles (comme des organiques) condensent, créant des particules formées principalement par ces gaz. Des simulations faites avec l’hypothèse de mélange interne (MI) et mélange externe (ME) sont comparées. Utiliser l’approche équilibre pour la condensation/évaporation conduit à des distributions de particules en taille et en composition similaires entre ME et MI. De plus grandes différences entre MI et ME sont observées avec l’approche dynamique. Ce travail a été publié dans Geoscientific Model Development (GMD) [Zhu et al., 2015a].

Preamble

In this chapter, a model for simulating externally-mixed particles is developed based on the size-composition discretization scheme of Dergaoui et al. [2013]. As discussed in section 1.5.2, in most air-quality models, particles are only discretized based on their size (see figure 2.1 (a)) and the mixing state between different particle populations is not represented. In order to study the particle mixing state, externally-mixed aerosol models have been developed (e.g., Jacobson et al. [1994], Jacobson [2002a], Oshima et al. [2009b], Lu and Bowman [2010]), Dergaoui et al. [2013]). The discretization scheme of Dergaoui et al. [2013] is used here, as it discretizes both the size and the composition of particles, as shown in figure 2.1 (b).

To illustrate the discretization of Dergaoui et al. [2013], let us consider a given particle p of size d_p and mass m_p with sp chemical components or species. The particle can be categorized into the discretized section represented by the vector \vec{P}_j of size-section index j_s and composition-section index j_c . The size index j_s is such that d_p is within the size bounds $[d_{j_s}, d_{j_s+1}]$; the composition index j_c is such that the mass fraction $f_{c_{sp}} = m_{sp}/m_p$ of any chemical component sp is within the fraction bounds $[f_{j_{c_{sp}}}^-, f_{j_{c_{sp}}}^+]$. A composition section j_c is defined as a combination of the mass-fraction ranges of the different chemical components, i.e. $j_c = (j_{c_{sp}})$ for sp varying between 1 and the number of chemical components.

Let us take the example of two chemical components A, B and C, discretized with two mass-fraction sections: $[0\%, 50\%]$ and $[51\%, 100\%]$. If the mass fraction of the third species is computed through mass conservation, there are in total 4 possible combinations

of the mass-fraction sections: $(A[0\%, 50\%], B[51\%, 100\%])$, $(A[51\%, 100\%], B[0\%, 50\%])$, $(A[0\%, 50\%], B[0\%, 50\%])$, $(A[51\%, 100\%], B[51\%, 100\%])$. However, the last combination is unrealistic as the total mass fraction would be larger than 100%. Therefore, only the first three combinations can be considered as realistic compositions. The same method applies for c chemical components. When generating the particle composition sections, the mass fractions of the first $c - 1$ components are discretized into N_f fraction ranges each. The h^{th} fraction range is represented by $F_{h-}^+ = [f_h^-, f_h^+]$ where $F_{h-1}^+ = f_h^-$ ($f_1^- = 0$ and $f_{N_f}^+ = 1$). So in total N_f^{c-1} combinations exist. However, among them, only those satisfying $\sum_{sp=1}^{(c-1)} F_{h_{sp}}^- \leq 1$ is realistic and are kept as the final composition sections. In the work of Dergaoui et al. [2013] such generation and selection of composition sections are conducted manually, which is only feasible when c and N_f are small. So, one of our first work was to develop and integrate an automatic composition generation algorithm. In this algorithm, all the fraction combinations are determined, and the combination is kept only if it is realistic. All the possible combination sections are then automatically generated.

The external-mixing model is named the Size-Composition Resolved Aerosol Model (SCRAM). It includes all three main processes involved in aerosol dynamics (coagulation, condensation/evaporation and nucleation). The model is first validated by comparison with a reference solution and with results of simulations using internally-mixed particles. The degree of mixing of particles is investigated in a box model simulation using data representative of air pollution in Greater Paris. The relative influence on the mixing state of the different aerosol processes (condensation/evaporation, coagulation) and of the algorithm used to model condensation/evaporation (bulk equilibrium, dynamic) is also studied.

Ce chapitre est constitué de:

Zhu, S., Sartelet, K. N., Seigneur, C. : **A size-composition resolved aerosol model for simulating the dynamics of externally mixed particles: SCRAM (v 1.0)**, *Geosci. Model Dev.*, 8 (6), 1595-1612, 2015, doi:10.5194/gmd-8-1595-2015

Sommaire

2.1	Introduction	45
2.2	Model Description	46
2.2.1	Condensation-Evaporation Algorithm	47
2.2.2	Bulk equilibrium and hybrid approaches	51
2.2.3	Overall time integration and operator splitting in SCRAM	51
2.3	Model validation	52
2.4	Simulation with realistic concentrations	54
2.4.1	Simulation set-up	55
2.4.2	Aerosol dynamics and mixing state	58
2.4.3	External versus internal mixing	62
2.4.4	Bulk equilibrium and hybrid approaches	64
2.5	Conclusions	66

Abstract

A Size-Composition Resolved Aerosol Model (SCRAM) for simulating the dynamics of externally-mixed atmospheric particles is presented. This new model classifies aerosols by both composition and size, based on a comprehensive combination of all chemical species and their mass-fraction sections. All three main processes involved in aerosol dynamics (coagulation, condensation/evaporation and nucleation) are included. The model is first validated by comparison with a reference solution and with results of simulations using internally-mixed particles. The importance of representing the mixing state when modelling atmospheric aerosol concentrations is investigated in a box model simulation using data representative of air pollution in Greater Paris.

2.1 Introduction

Increasing attention is being paid to atmospheric particulate matter (PM), which is a major contributor to air pollution issues ranging from adverse health effects to visibility impairment [EPA, 2009; Pascal et al., 2013]. Concentrations of PM_{2.5} and PM₁₀ are regulated in many countries, especially in North America and Europe. For example, regulatory concentration thresholds of 12 and 20 $\mu\text{g m}^{-3}$ have been set for PM_{2.5} annual mass concentrations in the United States and Europe, respectively. Furthermore, particles influence the Earth’s energy balance and global climate change [Myhre et al., 2013].

Three-dimensional chemical-transport models (CTM) are often used to study and forecast the formation and distribution of PM. The size distribution of particles is often discretised into sections [e.g., Gelbard and Seinfeld, 1980; Zhang et al., 2004; Sartelet et al., 2007] or approximated by log-normal modes [e.g., Whitby and McMurry, 1997; Binkowski and Roselle, 2003]. Moreover, CTM usually assume that particles are internally-mixed, i.e. each size section or log-normal mode has the same chemical composition, which may vary in space and time.

The internal-mixing assumption implies that particles of a same diameter (or in the same size section or log-normal mode) but originating from different sources have undergone sufficient mixing to achieve a common chemical composition for a given model grid cell and time. Although this assumption may be realistic far from emission sources, it may not be valid close to emission sources where the composition of new emitted particles can be very different from either background particles or particles from other sources. Usually, internally- and externally-mixed particles are not differentiated in most measurements, which may be size-resolved (e.g., cascade impactors) but not particle specific [McMurry, 2000]. The use of mass spectrometers for individual particle analysis has shed valuable information on the chemical composition of individual particles. Consequently, there is a growing body of observations indicating that particles are mostly externally mixed [e.g., Hughes et al., 2000; Mallet et al., 2004; Healy et al., 2012; Deboudt et al., 2010a].

The mixing state assumption may strongly influence aerosol chemistry and the hygroscopic characteristics of particles. Particles from different origins may not be well mixed, and their chemical composition may vary with their origins, leading to variations in their hygroscopic characteristics. This chemical identity of particles is gradually lost as the degree of mixing increases (or completely lost under the internal mixing assumption). By influencing the hygroscopic characteristics of particles, the mixing state also influences the formation of secondary organic aerosols (SOA), because condensation/evaporation differs for species that are hydrophilic and/or hydrophobic [Couvidat et al., 2012]. As the particle wet diameter is strongly related to the hygroscopic properties of particles, the mixing state also impacts particle wet diameters and the number of particles that become cloud condensation nuclei (CCN), because the activation of particles into CCN is strongly related to the particle wet diameter [Leck and Svensson, 2015]. By influencing CCN, the mixing state also affects aerosol wet removal and thus the aerosol spatial/temporal distribution. Besides, the mixing state influences the particle optical properties, which depend on both the particle size distribution (wet diameters) and composition (different chemical species possess different absorption/scattering properties). Lesins et al. [2002a] found that the percentage difference in the optical properties between an internal mixture and external mixture of black carbon and ammonium sulphate can be over 50%

for wet aerosols. The mixing state may also influence radiative forcing, as shown by Jacobson [2001] who obtained different direct forcing results between external and internal mixing simulations of black carbon.

Although CTM usually assume that particles are internally-mixed, several models have been developed during the last sesquidecade to represent the external mixture of particles. A source-oriented model was developed by Kleeman et al. [1997] and Kleeman and Cass [2001] for regional modelling. In these models, each source is associated with a specific aerosol population, which may evolve in terms of size distribution and chemical composition, but does not mix with the other sources (i.e., particle coagulation is neglected). Riemer et al. [2009] modelled externally-mixed particles using a stochastic approach. However, such an approach is computationally expensive when the number of particle species is high. On the other hand, Stier et al. [2005] and Bauer et al. [2008] simulate externally mixed particles using modal aerosol models, where aerosol populations with different mixing states are represented by modes of different compositions (soluble/mixed or insoluble/not mixed). Although these models may be computationally efficient, they may not model accurately the dynamics of mixing. To represent externally-mixed particles independently of their sources and number concentrations, Jacobson et al. [1994] and Lu and Bowman [2010] considered particles that can be either internally- or externally-mixed (i.e., composed of a pure chemical species). Lu and Bowman [2010] used a threshold mass fraction to define whether the species is of significant concentration. Jacobson [2002a] expanded on Jacobson et al. [1994] by allowing particles to have different mass fractions. Similarly, Oshima et al. [2009b] discretised the fraction of black carbon in the total particle mass into sections of different chemical compositions. Dergaoui et al. [2013] further expanded on these modelling approaches by discretising the mass fraction of any chemical species into sections, as well as the size distribution (see Section 2.2.1.3 for details). Based on this discretisation, Dergaoui et al. [2013] derived the equation for coagulation and validated their model by comparing the results obtained for internal and external mixing, as well as by comparing both approaches against an exact solution. However, processes such as condensation/evaporation and nucleation were not modelled.

This work presents a new Size-composition Resolved Aerosol Model (SCRAM), which expands on the model of Dergaoui et al. [2013] by including condensation/evaporation and nucleation processes. Section 2 describes the model. Equations for the dynamic evolution of particles by condensation/evaporation are derived. A thermodynamic equilibrium method may be used in SCRAM to compute the evolution of the particle chemical composition by condensation/evaporation. Redistribution algorithms, which allow section bounds not to vary, are also presented for future 3D applications. Model validation is presented in Section 3 by comparing the changes in the particle size distribution due to condensational growth for both externally- and internally-mixed particles. Section 4 presents an application of the model with realistic concentrations over Greater Paris.

2.2 Model Description

This section presents the aerosol general dynamic equations and the structure of the model. First, the formulation of the dynamic evolution of the aerosol size distribution and chemical composition by condensation-evaporation is introduced. Since it is nec-

essary in 3D CTM to maintain fixed size and composition section bounds, we present algorithms to redistribute particle mass and number according to fixed section bounds. For computational efficiency, a bulk equilibrium method, which assumes an instantaneous equilibrium between the gas and particle phases, is introduced. Finally, the overall structure of the model is described. In particular, the treatment of the different mixing processes to ensure the numerical stability of the model is discussed.

Particle dynamics is mostly governed by three processes: coagulation, condensation/evaporation, and nucleation. Nucleation refers to the formation of ultra fine particles from gaseous molecules. SCRAM uses the parametrisation of Vehkamäki et al. [2002] for the homogeneous binary nucleation of sulphate and water. It was adopted from the existing SIREAM code [Debry et al., 2007a]. It may be replaced by a better parametrisation in future versions, because it may lead to unrealistic results under some extreme conditions [Zhang et al., 2010]. For coagulation, SCRAM uses the code of Dergaoui et al. [2013] to simulate the collisions of particles caused by Brownian motion. Condensation/evaporation describe the mass transfer process between the gas and the particle phases. It is essentially to include condensation/evaporation, because this process not only largely influences the size distribution of aerosols, but may also change the composition of particles significantly.

2.2.1 Condensation-Evaporation Algorithm

The focus of the following subsections is the formulation and implementation of the condensation/evaporation process. A lagrangian approach is used to solve the equations of change for the mass and number concentrations, which are redistributed onto fixed sections through a redistribution algorithm (moving diameter, Jacobson [1997]). Equations are derived to describe the change with time of the mass concentrations of chemical species in terms of particle compositions.

2.2.1.1 Dynamic equation for condensation/evaporation

Let us denote m_i the mass concentration of species X_i ($1 \leq i \leq c$) in a particle and \vec{x} the vector representing the mass composition of the particle $\vec{x} = (m_1, m_2, \dots, m_c)$. Following Riemer et al. [2009], the change with time of the number concentration $n(\vec{x}, t)$ ($\text{m}^{-3} \mu\text{g}^{-1}$) of multi-species particles by condensation/evaporation can be represented by the following equation:

$$\frac{\partial n}{\partial t} = - \sum_{i=1}^c \frac{\partial(I_i n)}{\partial m_i} \quad (2.1)$$

where I_i ($\mu\text{g s}^{-1}$) is the mass transfer rate between the gas and particle phases for species X_i . It may be written as follows:

$$I_i = \frac{\partial m_i}{\partial t} = 2\pi D_i^g d_p f(K_n, \alpha_i)(c_i^g(t) - K_e(d_p) c_i^{eq}(\vec{x}, t)) \quad (2.2)$$

where D_i^g is the molecular diffusivity of condensing/evaporating species in the air, and d_p and c_i^g are the particle wet diameter and the gas phase concentration of species X_i , respectively. Non-continuous effects are described by $f(K_n, \alpha_i)$ [Dahneke, 1983] which

depends on the Knudsen number, $K_n = \frac{2\lambda}{d_p}$ (with λ the air mean free path), and on the accommodation coefficient $\alpha_i = 0.5$:

$$f(K_n, \alpha_i) = \frac{1 + K_n}{1 + 2K_n(1 + K_n)/\alpha_i} \quad (2.3)$$

$K_e(d_p)$ represents the Kelvin effect (for ultra fine particles, the curvature tends to inhibit condensation):

$$K_e(d_p) = \exp\left(\frac{4 \sigma v_p}{R T d_p}\right) \quad (2.4)$$

with R the ideal gas constant, σ the particle surface tension and v_p the particle molar volume. The local equilibrium gas concentration c_i^{eq} is computed using the reverse mode of the thermodynamic model ISORROPIA V1.7 [Nenes et al., 1998] for inorganic compounds. In the current version of SCRAM, organic compounds are assumed to be at thermodynamic equilibrium with the gas phase and condensation/evaporation is computed as described in Section 2.2.2.

2.2.1.2 Dynamic equation as a function of mass fractions

Following the composition discretisation method of Dergaoui et al. [2013] (detailed in Section 2.2.1.3), each particle is represented by a vector $\vec{p}=(\vec{f}, m)$, which contains the mass fraction vector $\vec{f}=(f_1, f_2, \dots, f_{(c-1)})$ of the first $(c - 1)$ species and the total mass $m = \sum_{i=1}^c m_i$.

In Equation (2.1), the chemical composition of particles is described by the vector \vec{x} , which contains the mass concentration of each species. After the change of variable through a $[c \times c]$ Jacobian matrix from $n(\vec{x}, t)$ to $\bar{n}(\vec{p}, t)$ (see Appendix A for detail), Equation (2.1) becomes:

$$\frac{\partial \bar{n}}{\partial t} = - \sum_{i=1}^{(c-1)} \frac{\partial(H_i \bar{n})}{\partial f_i} - \frac{\partial(I_0 \bar{n})}{\partial m} \quad (2.5)$$

with $I_0 = \sum_{i=1}^c I_i$, $H_i = \frac{\partial f_i}{\partial t}$. As $f_i = \frac{m_i}{m}$ is the mass fraction of species (or group of species) X_i , we may write:

$$H_i = \frac{1}{m} \frac{\partial m_i}{\partial t} - \frac{m_i}{m^2} \frac{\partial m}{\partial t} = \frac{I_i - f_i I_0}{m} \quad (2.6)$$

The change with time of $q_i = n m_i$, the mass concentration of species X_i , can be expressed as follows:

$$\frac{\partial q_i}{\partial t} = \frac{\partial n}{\partial t} m_i + \frac{\partial m_i}{\partial t} n \quad (2.7)$$

After the change of variables from $q_i(\vec{x}, t)$ to $\bar{q}_i(\vec{p}, t)$ (see Appendix A), Equation (2.7) becomes:

$$\frac{\partial \bar{q}_i}{\partial t} = -m f_i \frac{\partial \bar{n}}{\partial t} + \bar{n} I_i \quad (2.8)$$

2.2.1.3 Discretisation

As SCRAM is a size-composition resolved model, both particle size and composition are discretised into sections, while the numbers and bounds of both size and composition sections can be customised by the user. The particle mass distribution $Q[m_{min}, m_{max}]$ is first divided into N_b size sections $[m_k^-, m_k^+]$ ($k = 1, \dots, N_b$ and $m_{k-1}^+ = m_k^-$), defined by discretising particle diameters $[d_{min}, d_{max}]$ with d_{min} and d_{max} , the lower and upper particle diameters, respectively, and $m_k = \frac{\pi \rho d_k^3}{6}$. For each of the first $(c-1)$ species or species groups, the mass fraction is discretised into N_f fraction ranges. The h^{th} fraction range is represented by the range $F_{h-}^+ = [f_h^-, f_h^+]$ where $f_{h-1}^+ = f_h^-$, $f_{min} = 0$ and $f_{max} = 1$. Within each size section k , particles are categorised into N_p composition sections, which are defined by the valid combinations of the fraction ranges of the $(c-1)$ species. The g^{th} composition section can be represented by $\vec{P}_g = (F_{g1-}^+, F_{g2-}^+, \dots, F_{gc-1-}^+)$. Given the mass fraction discretisation, those composition sections are automatically generated by an iteration on all possible combinations ($N_f^{(c-1)}$) of the $(c-1)$ species and N_f fraction ranges. Only the composition sections that satisfy $\sum_{i=1}^{(c-1)} F_{gi}^- \leq 1$ are kept.

The particle mass distribution is discretised into $(N_b \times N_p)$ sections. Each section j ($j = 1, \dots, N_b \times N_p$) corresponds to a size section k ($k = 1, \dots, N_b$) and to a composition section $g = (g_1, \dots, g_{(c-1)})$ with $g = 1, \dots, N_p$, $g_h = 1, \dots, N_f$ with $h = 1, \dots, (c-1)$. The total concentration Q_i^j of species i in the j^{th} section can be calculated as follows:

$$Q_i^j = \int_{m_k^-}^{m_k^+} \int_{f_{g_1}^-}^{f_{g_1}^+} \dots \int_{f_{g_{(c-1)}}^-}^{f_{g_{(c-1)}}^+} \bar{q}_i(m, f_{g_1}, \dots, f_{g_{(c-1)}}) dm df_{g_1} \dots df_{g_{(c-1)}} \quad (2.9)$$

Similarly, the number concentration N^j of the j^{th} section may be written as follows:

$$N^j = \int_{m_k^-}^{m_k^+} \int_{f_{g_1}^-}^{f_{g_1}^+} \dots \int_{f_{g_{(c-1)}}^-}^{f_{g_{(c-1)}}^+} \bar{n}(m, f_{g_1}, \dots, f_{g_{(c-1)}}) dm df_{g_1} \dots df_{g_{(c-1)}} \quad (2.10)$$

After a series of derivations (see Appendix B for details), we obtain the time derivation of Equation (2.10):

$$\frac{\partial N^j}{\partial t} = 0 \quad (2.11)$$

as well as the time derivation of Equation (2.9):

$$\frac{\partial Q_i^j}{\partial t} = N^j I_{g_i} \quad (2.12)$$

Thus, in each section, the change with time of number and mass concentrations is given by Equations (2.11) and (2.12).

2.2.1.4 Numerical implementation

According to Debry and Sportisse [2006], the condensation/evaporation process may have characteristic time-scales of different magnitudes, because the range of particle diameters is large. Such feature induces strong stiffness of the numerical system. As suggested by

Debry et al. [2007a], the stiff condensation/evaporation equations are solved using the second-order Rosenbrock (ROS2) method [Verwer et al., 1999; Djouad et al., 2002].

In addition, potentially unstable oscillations may occur when a dramatic change of the particle pH occurs. To address this issue, a species flux electro-neutrality constraint [Pilinis et al., 2000; Debry et al., 2007a] is applied in SCRAM to ensure the numerical stability of the system.

2.2.1.5 Size and composition redistribution

By condensation/evaporation, the particles in each size section may grow or shrink. Because the bounds of size sections should be fixed for 3D applications, it is necessary to redistribute number and mass among the fixed size sections during the simulation after condensation/evaporation. Similarly, the chemical composition also evolves by condensation/evaporation and an algorithm is needed to identify the particle composition and redistribute it into the correct composition sections.

Two redistribution methods for size sections may be used in SCRAM: the HEMEN (Hybrid of Euler-Mass and Euler-Number) scheme of Devilliers et al. [2013] and the moving diameter scheme of Jacobson [1997]. According to Devilliers et al. [2013], both redistribution methods may accurately redistribute mass and number concentrations.

The HEMEN scheme divides particle size sections into two parts: the number is redistributed for sections of mean diameter lower than 100 nm and mass is redistributed for sections of mean diameter greater than 100 nm. The section mean diameters are kept constant and mass concentrations are diagnosed for sections where number is redistributed, while number concentrations are diagnosed for sections where mass is redistributed. The advantage of this scheme is that it is more accurate for number concentrations over the size range where number concentrations are the highest and more accurate for mass concentrations where mass concentrations are the highest. In SCRAM, the algorithm of Devilliers et al. [2013] was modified to take into account the fact that after condensation/evaporation, the diameter of a section may become larger than the upper bound of the next section. In that case, the mean diameter of the section after condensation/evaporation is used to diagnose in which fixed-diameter sections the redistribution is performed. This feature allows us to use larger time steps for condensation/evaporation before redistribution.

In the moving diameter method, although size section bounds are kept fixed, the representative diameter of each size section is allowed to vary. If, after condensation/evaporation, the diameter grows or shrinks outside section bounds, both the mass and number concentrations of the section are redistributed entirely into the new size sections bounding that diameter.

For the composition redistribution, a scheme based on the moving diameter method is applied (i.e., moving mass fraction). First, after condensation/evaporation, the mass fraction of each species is re-evaluated within each section. For each section, if the new composition does not match the section composition (i.e., if the mass fraction of each species does not fit into the mass fraction bounds of the species for that section), the section that has a composition that matches the new composition is identified, and both number and mass concentrations of each species are transferred to that section.

The composition redistribution is applied first, followed by the size redistribution for

each of the composition sections.

2.2.2 Bulk equilibrium and hybrid approaches

Bulk equilibrium methods assume an instantaneous thermodynamic equilibrium between the gas and bulk-aerosol phases. For semi-volatile species, the mass concentration of both gas and bulk-aerosol phases after condensation/evaporation are obtained using the forward mode of ISORROPIA for inorganics and the H²O model [Couvidat et al., 2012] for organics. Because time integration is not necessary, the computational cost is significantly reduced compared to the dynamic method. Weighting factors W are designed to distribute the semi-volatile bulk-aerosol mass across the aerosol distribution [Pandis et al., 1993]. In SCRAM, for each semi-volatile species i , we redistribute the bulk aerosol evaporating or condensing mass, $\delta Q_i = Q_i^{\text{after bulk eq.}} - Q_i^{\text{before bulk eq.}}$, between the sections j , using factors that depend on the ratio of the mass transfer rate in the aerosol distribution (Equation 2.2). Because of the bulk equilibrium assumption, the driving force of $(c_i^g - K_e c_i^{eq})$ is assumed to be the same for all size and composition sections, and the weighting factors are as follows.

$$W_i^j = \frac{N_j d_p^j f(K_n, \alpha_i)}{\sum_{k=1}^{N_s} N_k d_p^k f(K_n, \alpha_i)} \quad (2.13)$$

where N_j is the number concentration of section j and d_p^j is the particle wet diameter of section j . In case of evaporation, these weighting factors may not be appropriate, as they may lead to over-evaporation of some species in some sections, i.e. $Q_i^j \text{ after bulk eq.} = Q_i^{\text{before bulk eq.}} + \delta Q_i \times W_i^j < 0$. In the case of over-evaporation, we use a weighting scheme that redistributes the total bulk aerosol mass rather than the bulk aerosol evaporating or condensing mass

$$W_i^j = \frac{Q_i^j}{\sum_{k=1}^{N_s} Q_i^k} \quad (2.14)$$

and $Q_i^j \text{ after bulk eq.} = Q_i^{\text{after bulk eq.}} \times W_i^j$.

In fact, due to their larger ratios between surface area and particle mass, small particles may reach thermodynamic equilibrium much faster than large particles. Particles of diameters larger than 1 μm could require hours or even days to achieve equilibrium [Wexler and Seinfeld, 1990], which makes the bulk equilibrium assumption inappropriate for them. In order to maintain both the computational efficiency of the equilibrium method and the accuracy of the dynamic one, a hybrid method is adopted in SCRAM based on the work of Capaldo et al. [2000] and Debry and Sportisse [2006]. This method uses the equilibrium method for small particles ($d_p < 1 \mu\text{m}$) and uses the dynamic method to calculate the mass transfer for larger particles.

2.2.3 Overall time integration and operator splitting in SCRAM

In order to develop a system that offers both computational efficiency and numerical stability, we perform operator splitting for changes in number and mass concentrations

with time due to emission, coagulation, condensation/evaporation and nucleation, as explained below.

Emissions are first evaluated with an emission time step, which is determined by the characteristic time-scales of emissions obtained from the ratio of emission rates to aerosol concentrations. The emission time step evolves with time to prevent adding too much emitted mass into the system within one time step. Within each emission time step, coagulation and condensation/evaporation/nucleation are solved and the splitting time step between coagulation and condensation/evaporation/nucleation is forced to be lower than the emission time step. Time steps are obtained from the characteristic time steps of coagulation (t_{coag}) and condensation/evaporation/nucleation (t_{cond}). The larger of the time steps t_{coag} and t_{cond} determines the time step of splitting between coagulation and condensation/evaporation/nucleation. As coagulation is usually the slower process, the change due to coagulation is first calculated over its time step. Then, condensation/evaporation/nucleation are solved simultaneously. The change due to condensation/evaporation/nucleation is calculated, using time sub cycles, starting with the sub time step t_{cond} . The next sub time step for condensation/evaporation/nucleation is estimated based on the difference between the first and second order results provided by the ROS2 solver. Redistribution is computed after each time step of splitting of coagulation and condensation/evaporation/nucleation.

When the bulk thermodynamic equilibrium approach is used to solve condensation/evaporation, coagulation then nucleation are solved after each emission time step. The resolution is done as previously explained, except that the dynamic condensation/evaporation solver is disabled: sub time steps are used to solve coagulation and nucleation during one emission time step. Condensation/evaporation is then solved using the bulk equilibrium approach and the redistribution process is applied after the bulk equilibrium algorithm.

When the hybrid approach is used to solve condensation/evaporation, a time loop is added with a fixed time step of 600 s outside the emission time loop to compute bulk equilibrium condensation/evaporation for equilibrium sections. This additional time loop is designed to ensure that bulk equilibrium condensation/evaporation of equilibrium sections is not applied too often, so that the dynamic condensation/evaporation of dynamic sections has time to evolve. Redistribution is applied after the bulk equilibrium algorithm. Within this time loop, the aerosol dynamics is solved as previously explained using the dynamic condensation/evaporation algorithm for dynamic size sections: emissions are solved followed by coagulation and condensation/evaporation/nucleation. As in the fully dynamic approach, redistribution is applied after dynamic condensation/evaporation.

2.3 Model validation

To validate the model, the change with time of internally- and externally-mixed aerosol models are compared. The simulations use initial conditions for number and mass concentrations that are typical of a regional haze scenario, with constant sulphuric acid vapour source that gives a sulphuric acid condensation rate of $5.5 \mu\text{m}^3\text{cm}^{-3}$ per 12 hours [Seigneur et al., 1986; Zhang et al., 1999].

Simulations were conducted for 12 h at a temperature of 298 K and a pressure of 1

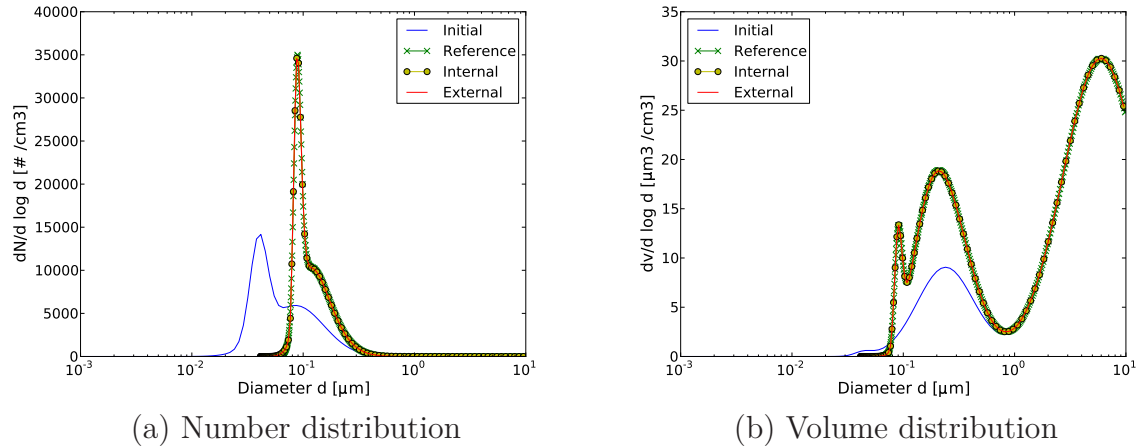


Figure 2.2: Simulation of condensation for hazy conditions: initial distribution and after 12 hours.

atm. The original reference simulation [Seigneur et al., 1986; Zhang et al., 1999] was first reproduced for internally-mixed sulphate particles (redistribution is not applied). For the sake of comparison between internally- and externally-mixed simulations, half of the particles were assumed to consist of sulphate (species 1) and the other half of another species of similar physical properties as sulphate (species 2). For internal mixing, the initial particles are all 50% species 1 and 50% species 2; and for external mixing, half of the initial particles are 100% species 1 and the other half are 100% species 2. As both species have the same physical properties, for any given size section, the sum over all composition sections of number and mass concentrations of externally-mixed particles should equal the number and mass concentrations of the internally-mixed particles. Particles were discretised into 100 size sections and 10 composition sections for the externally-mixed case. Figure 2.2 shows the initial and final distributions for the number and volume concentrations as a function of particle diameters. Both the internally-mixed and externally-mixed results are presented in Figure 2.2, along with the reference results of Zhang et al. [1999] (500 size sections were used in the original reference simulation). For the externally-mixed simulation, the results were summed up over composition sections to obtain the distributions as a function of particle diameter. As expected, an excellent match is obtained between internal and external mixing distributions, with an almost 100% Pearson's correlation coefficient. Furthermore, the accuracy of the SCRAM algorithm is proved by the good match between the results of these simulations and the reference simulation of Zhang et al. [1999]. In order to investigate the influence of the composition resolution on simulation results, two additional tests are conducted using 2 and 100 composition bins. The mean mass fraction of species 1 is computed for all particles within each size section, as well as their standard deviations. Figure 2.3 shows the size distribution of these statistics. The mean mass fraction is barely affected by the different composition resolutions as the condensation rate of sulphate is independent of the particle compositions. However, a different composition resolution does lead to different standard deviation distributions, as only particles with larger fraction difference ($d > 0.2\mu\text{m}$ for 2 compositions and $d > 0.09\mu\text{m}$ for 10 compositions) can be distinguished

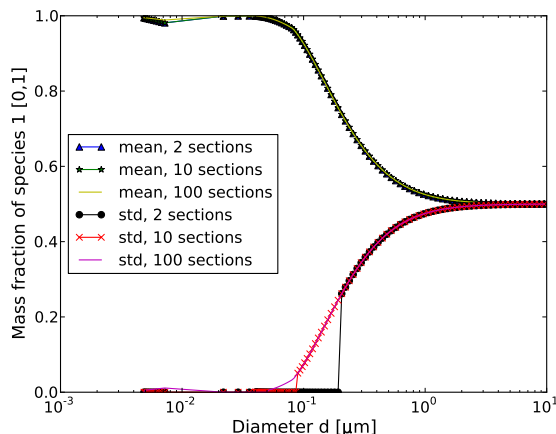


Figure 2.3: Mean and standard deviations of species 1 mass fraction as functions of particle diameter using 2, 10 and 100 composition sections.

from each other under coarser composition resolutions.

Using the same initial conditions and sulphuric acid condensation rate, a second comparison test was performed, with both coagulation and condensation occurring for 12 hours. As the coagulation algorithm requires size sections to have fixed bounds [Der-gaoui et al., 2013], size redistribution was applied for both the internally- and externally-mixed cases using the HEMEN method. As in the first comparison test, Figure 2.4 shows that there is a good match between the internally- and externally-mixed distributions as a function of particle diameter (no reference simulation was available for these simula-tions). This test validates the algorithm of SCRAM to simulate jointly the coagulation and condensation of externally-mixed particles.

The mixing states of both internally- and externally-mixed particles at the end of the simulations of the second test are shown in Figure 2.5. Sulphuric acid condenses to form particulate sulphate (species 1). During the simulation, pure species 2 particles mix with pure sulphate particles by coagulation and condensation of sulphuric acid. Figure 2.5 shows that, at the end of the simulation, the sulphate mass fraction is greater for particles of lower diameters, because the condensation rate is greater for those particles. Particles with diameters greater than 10 μm remain unmixed. However, the external mixing state provides a more detailed mixing map, from which it is possible to distinguish mixed particles from unmixed ones and to trace the origin of each particle. In this test case where the effect of condensation dominates that of coagulation, most mixed particles are originally pure species 2 particles coated with newly condensed sulphuric acid (Figure 2.5).

2.4 Simulation with realistic concentrations

To test the impact of external mixing on aerosol concentrations, simulations of coag-ulation, condensation/evaporation and nucleation were performed with SCRAM using realistic ambient concentrations and emissions extracted from a simulation performed over Greater Paris for July 2009 during the MEGAPOLI (Megacities: Emissions, urban,

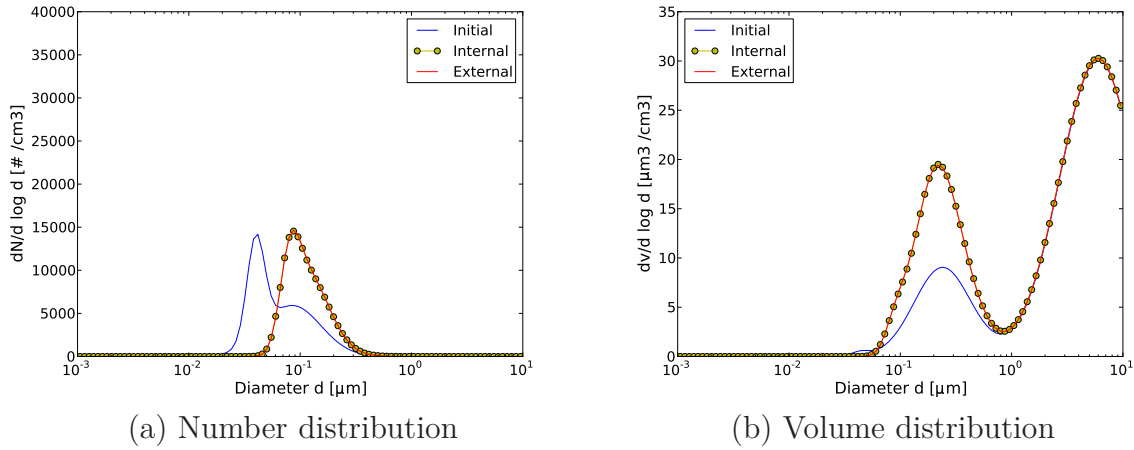


Figure 2.4: Simulation of both coagulation and condensation for hazy conditions: initial distribution and after 12 hours.

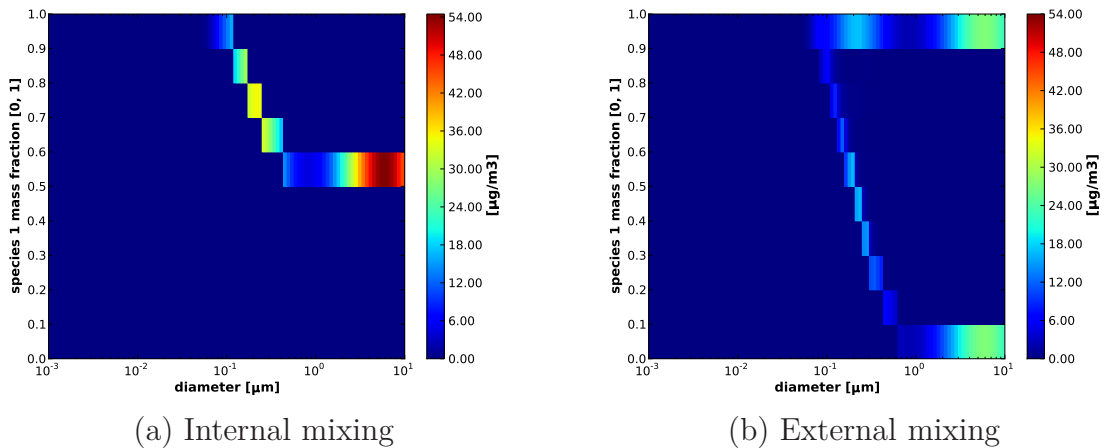


Figure 2.5: Distribution after 12 hours: particle mass concentration as a function of diameter and mass fraction of species 1.

regional and Global Atmospheric POLution and climate effects, and Integrated tools for assessment and mitigation) campaign [Couvidat et al., 2013].

2.4.1 Simulation set-up

Data were extracted from one grid cell of the 3D simulation performed by Couvidat et al. [2013] over Greater Paris. This surface grid cell was chosen because black carbon (EC) emissions are high in that location, due to high traffic emissions. Figure 2.6 shows the EC emission map at 2 UT, on 1 July 2009. The highest emission rate is located at the grid cell center of longitude and latitude (2.28° E, 48.88° N), which was selected here to extract the SCRAM simulation input data for emissions, background gas and aerosol concentrations, and initial meteorological conditions (temperature and pressure). In the absence of specific information on individual particle composition, all initial aerosol

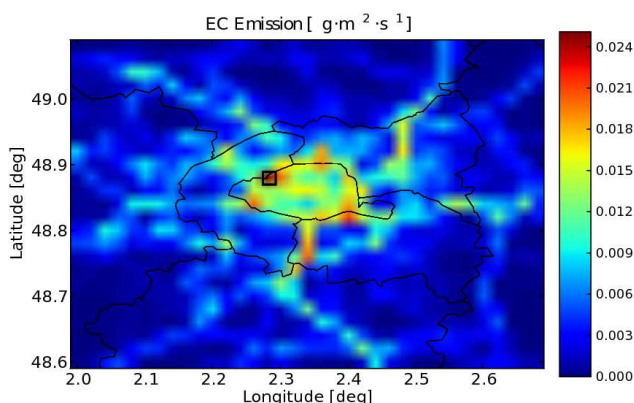


Figure 2.6: EC emissions over Greater Paris at 2 UT, 1 July 2009.

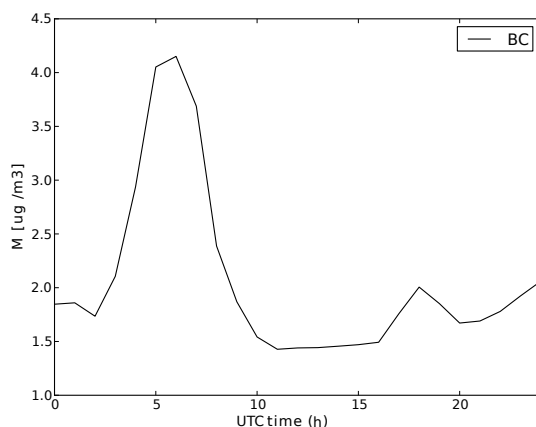


Figure 2.7: Transport EC concentrations profile of on 1 July 2009.

concentrations extracted from the database were assumed to be 100% mixed (i.e., aged background aerosols).

Simulations start at 2 UT (1 July 2009), i.e., just before the morning peak of traffic emissions, and last 12 hours. As our simulations are 0D, the transport of gases and particles and the deposition processes are not taken into account. Therefore, emissions accumulate, potentially leading to unrealistically high concentrations. To avoid this artifact, the duration of the emissions was limited to the first 40 min of simulation. This time duration is calculated using the average EC emission rate between 2 UT and 3 UT, so that EC emissions lead to an increase in EC concentrations equal to the difference between EC concentrations after and before the morning traffic peak, i.e., between 6 UT and 2 UT (Figure 2.7). Besides, gas-phase chemistry (such as SOA formation) is not included in SCRAM, and is expected to be solved separately using a gas-phase chemistry scheme. In the simulations of this work, SOA originates either from initial conditions or they are emitted as semi-volatile organic compounds during the simulation. They partition between the gas and the aerosol phases by condensation/evaporation.

The size distribution ranging from 0.001 to 10 μm was discretised into 7 sections with bounds at 0.001, 0.005, 0.01, 0.0398, 0.1585, 0.6310, 2.5119, and 10 μm . As in Couvidat et al. [2013], 31 particulate species were included in our simulations. In order to reduce the computational cost of the externally-mixed simulations, these species were grouped into 5 groups based on their chemical nature, which influences the formation of particles and their optical properties. Black carbon, organic species, inorganic species and dust are separated. Although sulphate could be separated from nitrate and ammonium for optical properties or for comparisons to observations of mixing state [Healy et al., 2012], and although chloride and sodium could be grouped together in a marine environment, all inorganic species are grouped together here for the sake of simplicity. However, because the hydrophylic properties of the particles strongly influence their formation and cloud condensation nuclei, hydrophylic and hydrophobic organic species are separated. In summary, the hydrophilic inorganic group (HLI) contains five inorganic species (sodium, sulphate, nitrate, ammonium and chloride); the hydrophilic organic group (HLO) contains 9 hydrophilic surrogate organic species (BiA2D, BiA1D, BiA0D, GLYOXAL, MGLY, BiMT, BiPER, BiDER and BiMGA); the hydrophobic organic group (HBO) contains 14 hydrophobic surrogate organic species (AnBIP, AnBmP, BiBIP, BiBmP, BiNGA, NIT3, BiNIT, AnCLP, SOAIP, SOAmP, SOAhP, POAIP, POAmP and POAhP); the black carbon group (EC) contains only black carbon; and the dust group (DU) contains all the neutral particles made up of soil, dust and fine sand. Refer to Couvidat et al. [2012] for detailed nomenclature of the organic species. For each of the first four groups, the mass fraction of the group over the total mass is discretised into 3 mass fraction ranges ($[0.0, 0.2)$, $(0.2, 0.8]$, $(0.8, 1.0]$), leading to 20 possible particle composition sections, as shown in Table 4.1. Among them, there are 5 unmixed particles and 15 mixed particles. Here unmixed is used in an approximate sense: it means that the mass fraction of one chemical component group is high (between 0.8 and 1), while the mass fraction of the other chemical component groups are low (between 0 and 0.2). The dust mass fraction is not discretised, as it is obtained by mass conservation. Note that although as an example we chose dust to be the group for which mass fraction is not treated explicitly, another group could be chosen as the group for which mass fraction is not treated explicitly. If all groups need to have their mass fraction treated explicitly, additional composition sections for the last group could be added to the current composition list without any modification to the main structure of the SCRAM code. The mass fraction of the last group would still be obtained by mass conservation, and the composition section of the particles would be chosen depending on this mass fraction.

In each group, water may also be present, although it is not considered when computing the mass fractions (it is calculated separately with the thermodynamic equilibrium models).

The model memorizes the relationship between each species index and group index, and it stores the mass concentrations separately for each species within each size-composition sections. The total mass concentration of each group is computed from the mass concentration of each species based on the species-group relations, allowing the computation of the mass fraction of each group.

Table 2.1: 20 Externally-mixed particle compositions

composition Index	Mixing state	Mass fraction of each groups (%)				
		HLI	HLO	HBO	EC	DU
1	unmixed(DU)	0-20	0-20	0-20	0-20	0-100
2	mixed	0-20	0-20	0-20	20-80	0-80
3	unmixed(EC)	0-20	0-20	0-20	80-100	0-20
4	mixed	0-20	0-20	20-80	0-20	0-80
5	mixed	0-20	0-20	20-80	20-80	0-60
6	unmixed(HBO)	0-20	0-20	80-100	0-20	0-20
7	mixed	0-20	20-80	0-20	0-20	0-80
8	mixed	0-20	20-80	0-20	20-80	0-60
9	mixed	0-20	20-80	20-80	0-20	0-60
10	mixed	0-20	20-80	20-80	20-80	0-40
11	unmixed(HLO)	0-20	80-100	0-20	0-20	0-20
12	mixed	20-80	0-20	0-20	0-20	0-80
13	mixed	20-80	0-20	0-20	20-80	0-60
14	mixed	20-80	0-20	20-80	0-20	0-60
15	mixed	20-80	0-20	20-80	20-80	0-40
16	mixed	20-80	20-80	0-20	0-20	0-60
17	mixed	20-80	20-80	0-20	20-80	0-40
18	mixed	20-80	20-80	20-80	0-20	0-40
19	mixed	20-80	20-80	20-80	20-80	0-20
20	unmixed(HLI)	80-100	0-20	0-20	0-20	0-20

2.4.2 Aerosol dynamics and mixing state

To understand how initial concentrations mix with emissions, four scenarios were simulated. In scenario (A), only emissions are taken into account in the simulation. Only coagulation is added to emissions in scenario (B), while only condensation/evaporation(C/E) is added to emissions in scenario (C). In scenario (D), emissions and all the aerosol dynamic processes are taken into account including nucleation (however, no nucleation occurred during the simulation due to low sulphuric acid gas concentrations).

The mass and number distributions of each chemical composition after 12 hours of simulation are shown in Figures 2.8 and 2.9 as a function of particle diameter, as well as their initial distributions in sub-figure (e). Bars with grayscale represent unmixed particles, while bars with colours are mixed particles. Each bar corresponds to a chemical composition index (CI). However, any CI with small number or mass concentrations are not really visible from the plot, so they are regrouped into mixed-other (for mixed CI) and unmixed-other (for unmixed CI) in the plot. The chemical compositions and the

Table 2.2: Mixing state after 12hs simulation

Process	No Dynamic scenario (A)	Coagulation scenario (B)	C/E scenario (C)	C/E+Coag+Nucl scenario (D)
Mixed particle number (%)	42	79	48	51
Mixed particle mass (%)	83	85	64	76

CI value associated with colour bars are listed in Table 2.1. All emitted particles are unmixed: CI 1 (100% DU) into size section (4-6), CI 3 (100% EC) into size section (3-6). So any mixed particles represented in sub-figure (a) of Figure 2.8 and 2.9 are due to initial condition instead of emissions. Besides, emissions also involve gas-phase POA and H_2SO_4 , which can not be observed in sub-figure (a) of Figure 2.8 and 2.9 as they has no interaction with particle phase under scenario (A). Organic vapours which may lead to the production of SOA is not included in the emissions, while certain concentration of such vapours is defined within the initial condition.

As shown by the simulation of scenario (A), emissions lead to high number concentrations of EC in the sections of low diameters (mostly below $0.631 \mu\text{m}$) and to high mass concentrations of dust and EC in the sections of high diameters (mostly above $0.631 \mu\text{m}$).

The comparison of scenarios (A) and (B) shows that coagulation does not affect much mass concentrations, but significantly reduces the number concentrations of particles in the sections of diameters lower than $0.631 \mu\text{m}$. Also, due to coagulation, small particles migrated to higher sections. For example, Figure 2.9 shows the mixed CI 15 particles that originate from the third size section migrated to the fourth size section, and this could result from coagulation between CI 14 size section 4 particles with CI 3 size section 3 particles, or between two CI 15 size section 3 particles.

As shown by the simulation of scenario (C), C/E leads to high mass and number concentrations of unmixed HBO (CI 6 – mass fraction of HBO (81.2%) above 80% (exact mass fraction of the dominate group will be specified within the parentheses right after the group name here after)), increasing the amount of unmixed particles. Organic matter of low and medium volatilities is emitted in the gas phase following Couvidat et al. [2013]. This organic matter condenses subsequently on well-mixed particles (CI 14 with mixed HLI (31%) and HBO (41%)), in sufficient amount to increase the mass fraction of HBO (81%) to over 80% and, therefore, transferring particles to the unmixed category CI 6 (these particles are not exactly unmixed since up to 20% may correspond to HLI (10%), but a finer composition resolution would be required to analyse their mixed characteristics). The condensation of organic matter on freshly emitted EC particles (CI 3) also occurs, as shown by the mixed EC (26%) and HBO (68%) particles (CI 5) which appear in the third and fourth size sections.

As shown by comparing scenarios (A) and (B) and scenarios (C) and (D), coagulation significantly reduces number concentrations. The mass concentrations of fine particles (diameters lower than $0.631 \mu\text{m}$) are also reduced. Furthermore, the composition diversity increases. For example, as demonstrated by the difference between scenarios (C) and (D), newly mixed particles of CI 4 (between 20% and 80% of HBO (78% for size 4 and 73% for size 5)) are formed by the coagulation of unmixed particles from CI 6 with others within the fourth and fifth size sections.

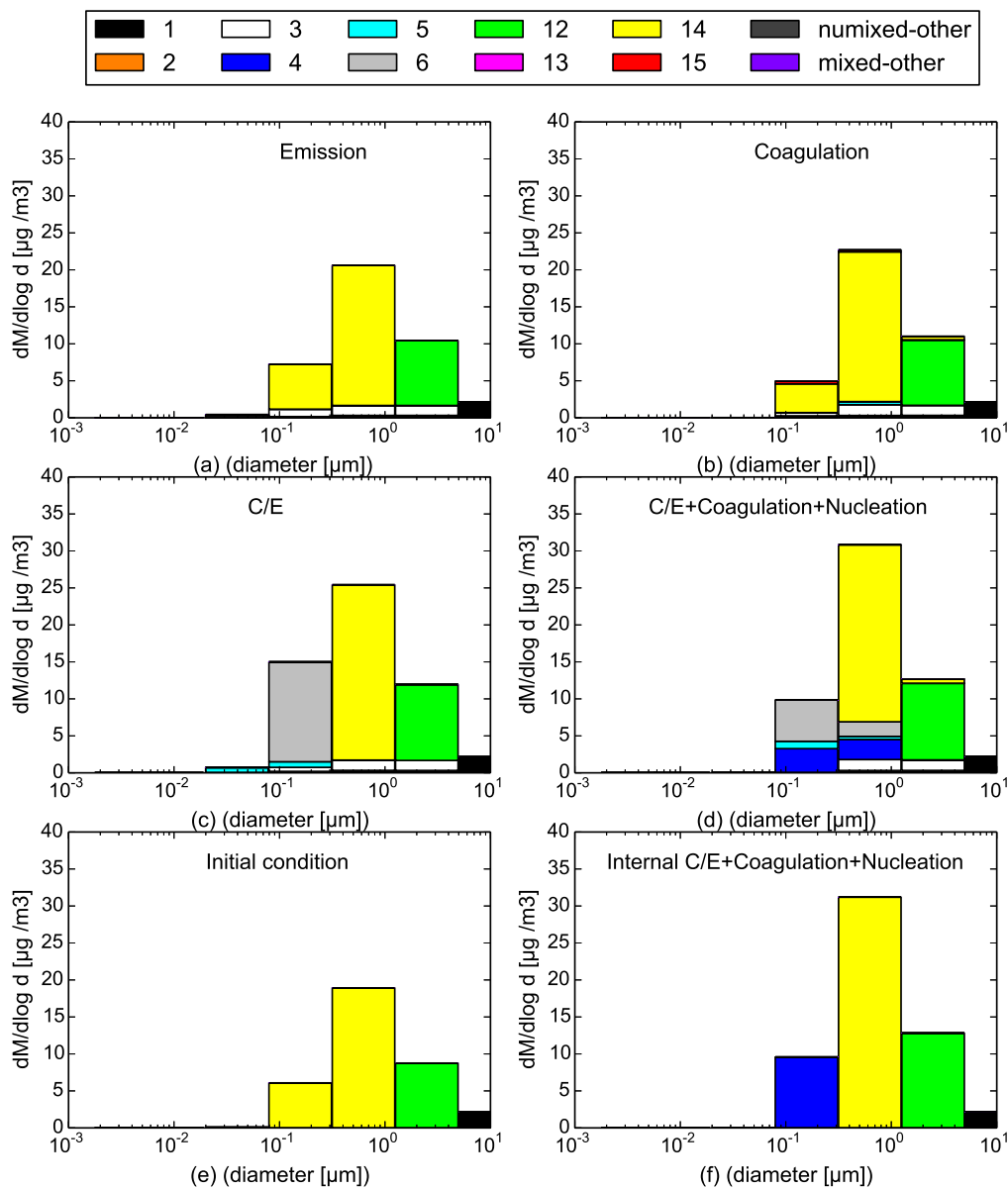


Figure 2.8: Result mass distributions of externally-mixed particles as a function of particle diameter for the different chemical compositions for 6 different simulation scenarios: (a) Emission only; (b) Emission+Coagulation; (c) Emission+C/E; (d) Emission+Coagulation+C/E+nucleation; (e) Initial Condition; (f) Internal mixing result.

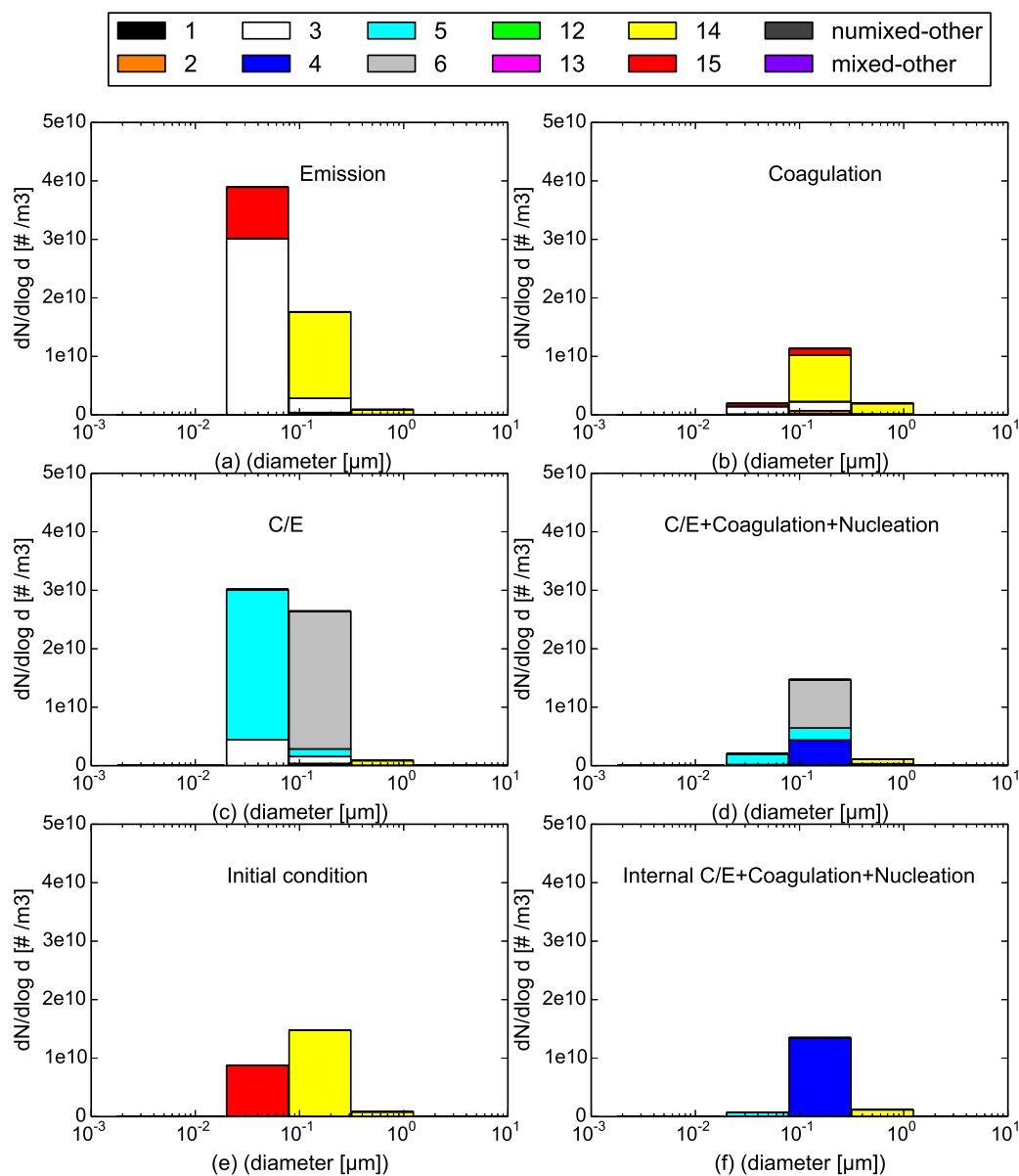


Figure 2.9: Result number distributions of externally-mixed particles as a function of particle diameter for the different chemical compositions for 6 different simulation scenarios: (a) Emission only; (b) Emission+Coagulation; (c) Emission+C/E; (d) Emission+Coagulation+C/E+nucleation; (e) Initial Condition; (f) Internal mixing result.

Table 2.2 shows the percentage of mixed particles for each scenario based on both particle number and mass concentrations. It seems that large particles are better mixed than small particles as the mixing percentages of mass are always higher than those of number. However, this phenomenon is specific to this case study; it is caused by the assumption of all initial particles being internally mixed and the initial conditions dominating for large particles due to their low emissions and the short duration of the simulations.

The number/mass mixing percentages after emission only (scenario (A)) provide a baseline for the analysis of the three other scenarios. In scenario (A), 42% (resp. 83%) of the particle number (resp. mass) originates from initial conditions and is mixed, while the remaining particles are due to emissions and are unmixed. The comparison of scenarios (A) and (B) shows that coagulation increases the mixing percentages, especially for small particles of high number concentrations. The mass mixing percentages decrease in scenario (C) because the condensation of freshly emitted organic matter on large mixed particles leads to particles with a mass fraction of organic matter (HBO) higher than 80%, i.e. unmixed. When all aerosol dynamic processes are taken into account (scenario (D)), only 51% of particle number concentration and 76% of particle mass concentration are mixed. The mixing percentages are greater than those of scenario (C), as mixing increases by coagulation, but the mass mixing percentage is lower than in scenario (A) (emissions only) because of the strong condensation of HBO emitted in the gas phase.

2.4.3 External versus internal mixing

To investigate the consequence of the internal mixing hypothesis, a simulation of scenario (D) (all aerosol dynamic processes are taken into account) is conducted by assuming all particles to be internally mixed. Externally- and internally-mixed 12-hour simulations lead to a similar total aerosol mass concentration after 12 h ($33.09 \mu\text{gm}^{-3}$ for internal mixing and $33.35 \mu\text{gm}^{-3}$ for external mixing) as well as to similar total number concentrations ($1.16 \times 10^{10} \text{ #m}^{-3}$ for internal mixing and $1.07 \times 10^{10} \text{ #m}^{-3}$ for external mixing). The bulk mass concentrations of individual species are also similar, although external mixing leads to slightly lower ammonium concentrations (2.68 #m^{-3} versus 2.70 #m^{-3}), slightly higher nitrate concentrations (3.19 #m^{-3} versus 3.03 #m^{-3}) and higher chloride concentrations (0.36 #m^{-3} versus 0.25 #m^{-3}). The size distributions for number and for individual species masses are also very similar in the internal and external mixing simulations.

Figure 2.8 (d) and (f) compares the mass distributions and compositions within each size section after 12 h of the internal and external mixing simulations. External mixing provides more detail about the particle mixing state, as within each size section particles have different compositions. For example, in the case of internal mixing, particles in size section 4 (diameter between $0.0398 \mu\text{m}$ and $0.1585 \mu\text{m}$) are all mostly hydrophobic organics (CI 4: HBO (76%) between 20% and 80%). The particle compositions are more detailed in the external mixing simulation: while less than half of the particles are mostly hydrophobic organics (HBO 78%) (CI 4) as in internal mixing, a large amount are unmixed particles (CI 6: HBO (82%) between 80% and 100%), and some are equally mixed with EC and hydrophobic organics (CI 5). In size section 5, as in the internal mixing simulation, mixed particles dominate (CI 14 - HLI 46%, HBO 36%), but many

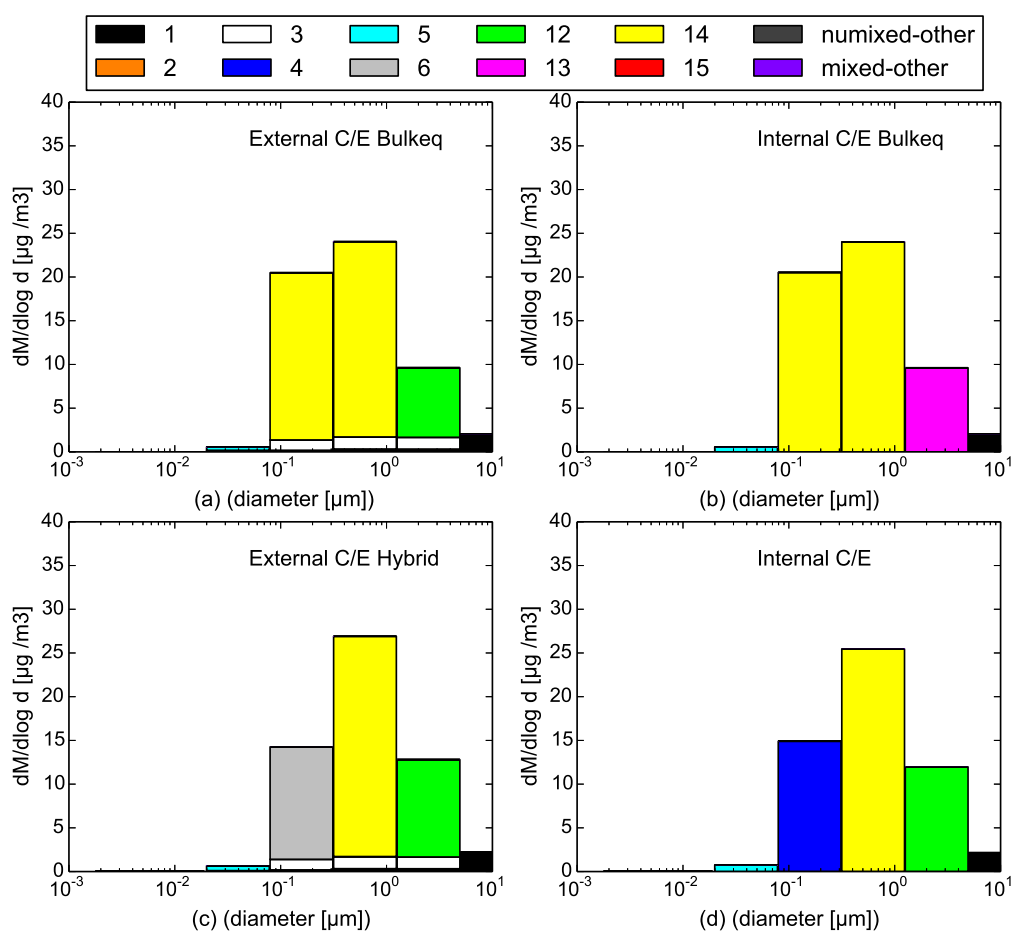


Figure 2.10: Result mass distributions of externally-mixed particles as a function of particle diameter for the different chemical compositions for 4 different C/E simulation scenarios: (a) External bulk-equilibrium; (b) Internal bulk-equilibrium; (c) External hybrid method; (d) Internal dynamic.

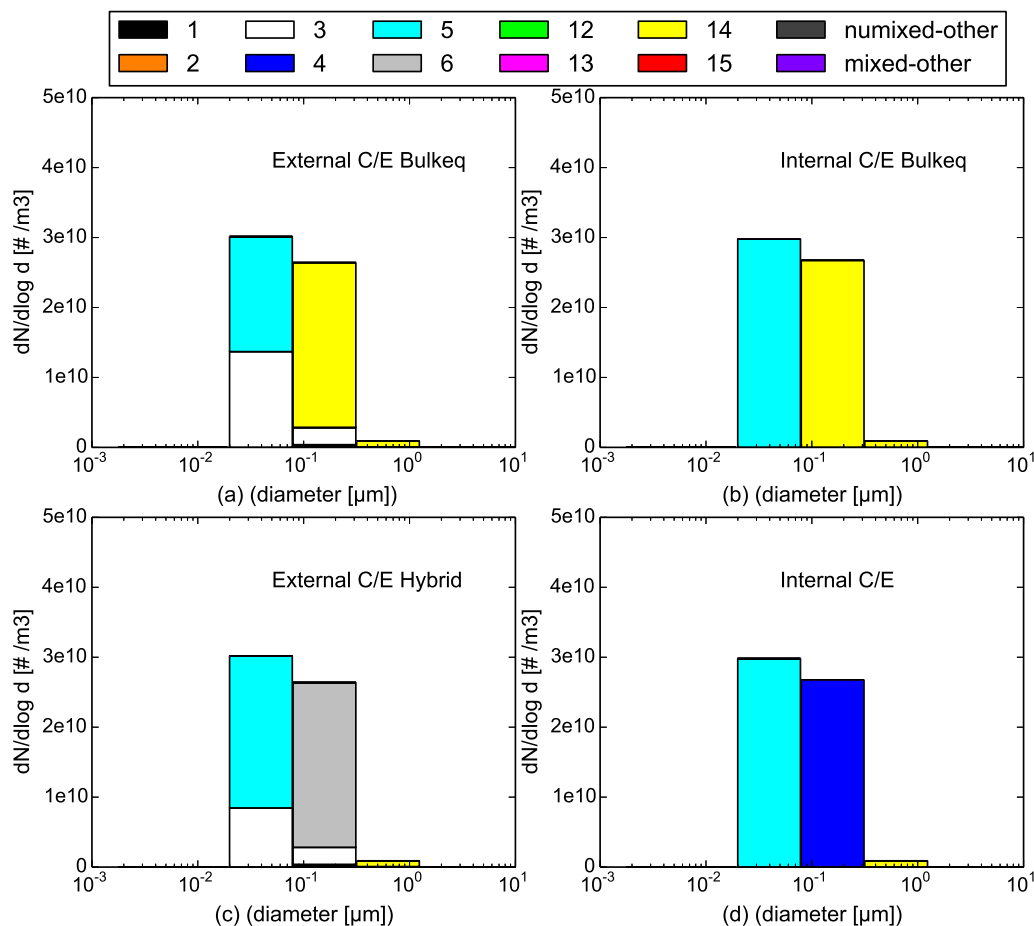


Figure 2.11: Result number distributions of externally-mixed particles as a function of particle diameter for the different chemical compositions for 4 different C/E simulation scenarios: (a) External bulk-equilibrium; (b) Internal bulk-equilibrium; (c) External hybrid method; (d) Internal dynamic.

have a different composition (CI 4 and 5) and some are unmixed HBO 83% (CI 6), EC 91% (CI 3) and dust 90% (CI 1). For particles in size section 6, particles are mixed particles of CI 12 (HLI 54%,DU 29%), while external mixing also shows that some particles are unmixed (EC 99% (CI 3) and dust 98% (CI 1)) and there are CI 14 (HLI 46%, HBO 35%) particles that originated from size section 5 through coagulation.

2.4.4 Bulk equilibrium and hybrid approaches

Additional external mixing tests were conducted using the bulk equilibrium and hybrid approaches for C/E to evaluate both their accuracy and computational efficiency. In the hybrid approach, the lowest four sections are assumed to be at equilibrium (up to diameters of $0.1585 \mu\text{m}$), whereas the other sections undergo dynamic mass transfer between the gas and particle phases .

The accuracy of these approaches is evaluated by comparing the mass and number

Table 2.3: Computational times

Process	C/E	C/E bu	C/E hy	Cg	C/E+Cg	C/E+Cg bu	C/E+Cg hy
Internal mixing (s)	7.1	0.11	0.4	0.06	7.3	0.14	0.5
External mixing (s)	63.2	0.3	54.2	48.4	122.8	31.5	113

distributions after 12 hour simulations with the bulk equilibrium or the hybrid approaches to the mass and number distributions computed dynamically (see Figures 2.10 and 2.11).

For externally-mixed particles, the dynamic mass distribution is shown in Figure 2.8(c); the bulk equilibrium and hybrid mass distributions are shown in Figure 2.10(a) and Figure 2.10(c), respectively. The dynamic number distribution is shown in Figure 2.9(c); the bulk equilibrium and hybrid mass distributions are shown in Figure 2.11(a) and Figure 2.11(c), respectively. For internally mixed particles, the dynamic mass/number distributions are shown in Figures 2.10(d) / 2.11(d) and the bulk equilibrium mass/number distributions in Figures 2.10(b) / 2.11(b), respectively.

For internally-mixed particles, the comparisons between Figures 2.10(b) and 2.10(d) and between Figures 2.11(b) and 2.11(d) indicate that the bulk equilibrium approach leads to significantly different distributions and compositions than the dynamic approach. This result also holds for externally-mixed particles, as shown by the comparisons between Figures 2.8(c) and 2.10(a) and between Figures 2.9(c) and 2.11(a). For example, more inorganic species condense on particles in the fourth size section (between 0.0398 μm and 0.1585 μm) in the case of bulk equilibrium compared to the fully dynamic case. This section is dominated by CI 14 (HLI 33%, HBO 61%) (equal mixture of inorganic and hydrophobic organics) for bulk equilibrium, instead of CI 6 (HBO 81%) (unmixed hydrophobic organics) for dynamic. Internal and external distributions are similar with the dynamic approach, as well as with the bulk equilibrium approach. Although internal and external compositions are different with the dynamic approach, they are quite similar with the bulk equilibrium approach. However, with the bulk equilibrium approach, similarly to the dynamic approach, unmixed particles of CI 3 (unmixed EC) remain present in most size sections for externally-mixed particles.

The mass and number distributions and compositions obtained with the hybrid approach are similar to the fully dynamic approach. For example, the over-condensation of inorganic species in the fourth size section (leading to particles of CI 14 (HLI 33%, HBO 61%) with bulk equilibrium) is restrained with the hybrid approach, as the fourth size section is computed dynamically, and particles consist of CI 6 (HBO 81%), as with the dynamic approach.

Table 2.3 shows the computational times (CPU) required for each simulation on a DELL Precision T3500 workstation (the lowest integration time step: 1). External mixing requires more CPU, especially for computing coagulation and dynamic C/E. The largest difference between internal and external mixing occurs for computing coagulation, which is almost 800 times slower with external mixing. Bulk equilibrium C/E provides a huge economy in CPU time for all simulations compared to dynamic C/E, while the computational advantage of hybrid C/E is more obvious for internal mixing (17 times faster than dynamic C/E) than external mixing (15% faster than dynamic C/E). This significant speed degradation of the hybrid C/E scheme in the external mixing case

is probably a consequence of small time steps used in the ROS2 solver because of the redistribution among the different composition sections performed after each time step. In other words, it takes CPU time to compute the dynamic distribution among the different composition sections.

2.5 Conclusions

A new Size-Composition Resolved Aerosol Model (SCRAM) has been developed to simulate the dynamic evolution of externally-mixed particles due to coagulation, condensation/evaporation, and nucleation. The general dynamic equation is discretised for both size and composition. Particle compositions are represented by the combinations of mass fractions, which may be chosen to correspond either to the mass fraction of the different species or to the mass fraction of groups of species (e.g. inorganic, hydrophobic organics...). The total numbers and bounds of the size and composition sections are defined by the user. An automatic classification method is designed within the system to determine all the possible particle compositions based on the combinations of user-defined chemical species or groups and their mass-fraction ranges.

The model was first validated by comparison to internally-mixed simulations of condensation / evaporation of sulphuric acid and of condensation / evaporation of sulphuric acid with coagulation. It was also validated for condensation against a reference solution.

The model was applied using realistic concentrations and typical emissions of air pollution over Greater Paris, where traffic emissions are high. Initial concentrations were assumed to be internally mixed. Simulations lasted 12 h.

Although internally- and externally-mixed simulations lead to similar particle size distributions, the particle compositions are different. The externally-mixed simulations provide details about particle mixing states within each size section when compared to internally mixed simulations. After 12 h, 49% of number concentrations and 24% of mass concentrations are not mixed. These percentages may be higher in 3D simulations, because initial aerosol concentrations should not be assumed as entirely internally mixed over an urban area. Coagulation is quite efficient at mixing particles, as 52% of number concentrations and 36% of mass concentrations are not mixed if coagulation is not taken into account in the simulation. On the opposite, condensation may decrease the percentage of mixed particles when low-volatility gaseous emissions are high.

Assuming bulk equilibrium when solving condensation/evaporation leads to different size and composition distributions than the dynamic approach under both the internally- and externally-mixed assumptions. With the bulk equilibrium approach, internally- and externally-mixed assumptions lead to similar average compositions as a function of size, and unmixed particles remain under the externally-mixed assumption, which were also observed with the dynamic C/E approach.

Although the simulation of externally mixed particles increases the computational cost, SCRAM offers the possibility to investigate particle mixing state in a comprehensive manner. Besides, its mixing state representation is flexible enough to be modified by users. Better computational performance could be reached with fewer, yet appropriately specified species groups and more optimised composition discretisations. For example, about half of the 20 compositions designed in this work have really low mass concentra-

tions (e.g. see Figures 2.8, 2.9, 2.10 and 2.11). Those compositions might be dynamically deactivated in the future version of SCRAM to lower computational cost by using an algorithm to skip empty sections during coagulation and C/E processing.

Future work will focus on the optimisation and incorporation of SCRAM into the air quality modelling platform Polyphemus for 3D simulations. In order to investigate its performance in modelling air quality over Greater Paris, model simulation results will be compared to observations [Healy et al., 2012].

Code availability

The SCRAM source code related to this article is available under the URL: <http://cerea.enpc.fr/polyphemus/src/scram-1.0.tar.gz> , as a supplement package together with Read Me file, where hardware and software requirements, source code files and model output files are fully described.

SCRAM is a free software. You can redistribute it and/or modify it under the terms of the GNU General Public License as published by the Free Software Foundation.

Chapter 3

Three-dimensional modelling of the mixing state of particles over Greater Paris

Résumé

SCRAM est intégré dans la plate-forme de qualité de l'air Polyphemus et utilisé pour effectuer des simulations sur l'Ile de France pendant l'été 2009. Une évaluation par comparaison à des observations montre que SCRAM/Polyphemus simule de manière satisfaisante les concentrations de $PM_{2.5}$ et de PM_{10} , ainsi que l'épaisseur optique des aérosols. Le modèle est utilisé pour analyser l'état de mélange des particules, ainsi que l'impact de l'hypothèse de mélange faite dans le modèle sur la formation des particules et leurs propriétés. Deux simulations sont effectuées et comparées : une avec l'hypothèse de mélange interne (MI) et l'autre en mélange externe (ME). En comparant les résultats des simulations MI et ME avec l'approche dynamique pour modéliser la condensation/évaporation, on constate que ME conduit à une concentration de nitrate supérieure ($1,24 \mu\text{g m}^{-3}$ en moyenne) que MI ($0,76 \mu\text{g m}^{-3}$ en moyenne), et les différences sont particulièrement élevées pour les pics (près de 100% dans le cas du nitrate). L'état de mélange de carbone élémentaire (EC) est également étudié. Au site urbain de Paris, le pourcentage de particules d'EC non mélangées est toujours supérieur à 35% avec un pic autour de 80% pendant les heures de pointe, lorsque les émissions de la circulation sont les plus élevées. Des analyses sur les propriétés optiques des particules montrent que, en général, la simulation MI mène à des épaisseurs optiques d'aérosols (AOD) supérieures à celles de la simulation ME, et à des albédos de simple diffusion (SSA) inférieurs à ceux de la simulation ME. Pour SSA, les différences entre les simulations EM et IM sont inférieures à 11%, et elles sont concentrées sur la ville de Paris, en zone urbaine, car les particules de EC y sont le plus souvent non mélangées dans la simulation ME. Pour AOD, les différences entre MI et ME sont causées principalement par des différences de concentrations de la teneur en eau des aérosols, causées par des différences de formation des aérosols inorganiques comme mentionné plus haut. Par exemple, une différence de 22% en concentrations d'inorganiques peut conduire à une différence de 80% de la concentration en eau et 72% en AOD. Concernant la formation des nuages et l'activation des particules en gouttes d'eau (noyaux de condensation), à faible sursaturation, MI conduit à un

pourcentage d'activation de noyaux de condensation plus bas que ME, car la présence de composés hydrophobes dans les particules de MI limite l'activation et seules les particules hydrophiles de la simulation ME peuvent être activées. A forte sursaturation, MI conduit à un pourcentage d'activation de noyaux de condensation plus élevé que ME, parce que la plupart des particules sont activées à l'exception des particules qui sont essentiellement hydrophobes et non mélangées dans la simulation ME. En outre, en cas de forte sursaturation, les différences entre les simulations MI et ME dans la répartition spatiale des particules activées sont plus importantes sur les régions urbaines. Ce travail a été soumis à *Journal of Geophysical Research (JGR): Atmospheres*.

Preamble

After the development of the 0-D version of SCRAM and its validation through comparisons between internal and external mixing simulations, the ability of SCRAM to model particle concentrations and the particle mixing state in three-dimensional air quality models is investigated. The aim is to evaluate the model performance by comparisons of the simulations to measurements of PM_{10} , $PM_{2.5}$ and aerosol optical depth, as well as to investigate the impact of the mixing-state assumption made in modelling on aerosol formation, composition, optical properties and cloud condensation nuclei (CCN) formation.

The SCRAM model is first integrated into the Polyphemus air-quality modelling platform. In order to support the additional composition dimension introduced by SCRAM compared to the currently used aerosol model (SIREAM), all aerosol related data structures and functions in Polyphemus are updated. The number of particles and the chemical components of each size/composition sections are transported. The model is very flexible, as it allows simulations with either the internal or the external mixing assumption. For input data, both initial and boundary conditions of the simulation can be specified as either internally mixed (data without composition information) or externally mixed (data with composition information). In case of internally-mixed data, the composition index of each section is computed based on the composition of particles in that section. However, emissions are considered as externally mixed (particles are only made of the emitted chemical component).

Four simulations are carried out for one week from 28 June to 5 July 2009, over Greater Paris. Meteorology is generated with WRF (v3.6) model using an urban canopy model and the Corine land-use with the YSU parametrization. Initial and boundary conditions inputs are from internal mixing simulation, which were obtained from nested simulations over Europe and France, as detailed in [Couvidat et al., 2013]. Emissions are generated based on the Airparif and EMEP inventories. Two simulations assume that particles are internally mixed (IM), while two other simulations simulate externally-mixed particles (EM). Within each of these two groups of simulations (IM and EM), one simulation uses the fully dynamic approach for condensation/evaporation, while the other one uses the bulk equilibrium approach for solving condensation/evaporation.

The concentrations from IM and EM simulations are similar when bulk equilibrium is assumed for condensation/evaporation. Comparisons therefore focus on differences from IM and EM simulations when condensation/evaporation is computed dynamically. Note that only the condensation/evaporation of inorganics can be computed dynamically

here. EM leads to higher nitrate concentration ($1.24 \mu\text{g m}^{-3}$ on average) than IM ($0.76 \mu\text{g m}^{-3}$ on average) and lower ammonium concentration ($1.23 \mu\text{g m}^{-3}$ on average) than IM ($1.33 \mu\text{g m}^{-3}$ on average). Furthermore, the differences are especially high for peak concentrations. Between 3 and 4 July, the peak concentration of nitrate for the EM simulation is twice the one for the IM simulation.

We define the unmixed EC percentage as the ratio of the EC mass of unmixed EC particles to the EC mass of all particles. At the urban site of Paris, the unmixed EC percentage does not drop to low values: it is higher than 35% with peaks around 80% during rush hours when emissions are the highest.

Detailed analyses are also conducted to investigate the impact of the mixing state on particle optical properties as well as on the cloud condensation nuclei (CCN) based on the dynamic IM and EM simulations. Using the same aerosol optical depth (AOD) computation method (core or mix), the IM simulation leads to higher AOD values and lower Single Scattering Albedo (SSA) values than the EM simulation. However, the differences between AOD computed using a core or a mix method and AOD are lower than differences between AOD computed from the IM and EM simulations. For SSA, the largest differences, up to 11% between IM and EM simulations, are concentrated in the city of Paris, where a large percentage of EC is unmixed in the EM simulation, affecting the absorption and scattering properties of particles. For AOD, differences between IM and EM are rather low over the city of Paris, but they are high over some regions such as the north east and the south west of Paris. Differences are due to differences in inorganic concentrations resulting from differences in the mixing-state assumption, and leading to differences in water aerosol concentration. For example, a difference of 22% in inorganic concentrations can lead to a difference as high as 80% in water concentration and 72% in AOD. Concerning CCN, at low supersaturation, IM leads to lower CCN activation percentage than EM, because the hydrophobic components of IM particles inhibit activation and only the hydrophilic particles of the EM simulation may be activated. At high supersaturation, IM leads to higher CCN activation percentage than EM, because most particles are activated except for the particles that are mostly hydrophobic in the EM simulation. Moreover, in case of high supersaturation, the difference in the spatial distribution between IM and EM simulations are more significant over urban regions. However, such distribution pattern is opposite in case of low supersaturation.

This chapter consists of

Zhu, S., Sartelet, K. N., Zhang, Y., Nenes, A. : **Three-dimensional modelling of the mixing state of particles over Greater Paris**, Journal of Geophysical Research, 2015, submitted.

Sommaire

3.1	Introduction	73
3.2	Model description and simulation setup	74
3.3	Particle concentrations	77
3.3.1	PM concentrations	77
3.3.2	Inorganic aerosol formation	80
3.3.3	Mixing state of EC	81
3.4	Aerosol optical properties	83
3.4.1	Computation of aerosol optical properties	83
3.4.2	Comparisons to AERONET measurements	84
3.4.3	Influence of the mixing state	85
3.4.4	Contributions of particle types	88
3.5	Cloud Condensation Nuclei	89
3.5.1	Computation of CCN	89
3.5.2	Impact of the mixing state on CCN	90
3.5.3	Contribution of particle types	92
3.6	Conclusions	93

Abstract

A size-composition resolved aerosol model (SCRAM) is coupled to the Polyphemus air quality platform and evaluated over Greater Paris. SCRAM simulates the particle mixing state and solves the aerosol dynamic evolution taking into account the processes of coagulation, condensation/evaporation and nucleation. Both the size and mass fractions of chemical components of particles are discretized. For a given particle size section, particles may have distinct chemical compositions. When discretizing mass fractions, chemical components are grouped into several aggregates to reduce computational cost. SCRAM has been integrated into the Polyphemus air quality modelling platform, and its performance to model air quality over Greater Paris is evaluated by comparison of model prediction to the measurements of PM₁₀, PM_{2.5} and aerosol optical depth. Because air quality models usually uses simplifying treatments with an assumption that particles are internally mixed, the impact of the mixing state assumption on aerosols formation, composition, optical properties and their ability to be activated as cloud condensation nuclei (CCN) is investigated. The simulation results show that more than half (up to 80% during rush hours) of black carbon particles are unmixed at the urban site of Paris, while they are more mixed with organic species at a rural site. The comparisons of simulations run with the internal-mixing (IM) assumption and with modelling of the mixing state (external-mixing (EM) assumption) show that IM assumption leads to lower nitrate and higher ammonium in the particulate phase. Besides, the IM assumption leads to lower

single scattering albedo, and the difference of aerosol optical depth caused by different mixing states can be as high as 72.5%. Moreover, the IM assumption leads to lower CCN activation percentage at low supersaturation, but higher CCN activation percentage at high supersaturation.

3.1 Introduction

Airborne particulate matter (PM) is regulated in many countries due to its adverse impact on human health, visibility and climate [Pascal et al., 2013; Davidson et al., 2005; Jacobson, 2002c]. Hence, air quality models are used to simulate and forecast its concentration. Most of existing models assume that particles are internally mixed (i.e., particles of the same size mix instantaneously when they meet and have the same chemical composition), largely for computational reasons. However, field measurements [Murphy et al., 2006; Healy et al., 2012] have proved that a wide range of particle compositions can coexist in the atmosphere, namely they are externally mixed, and the internal-mixing (IM) assumption may be inaccurate especially close to emission sources. For example, the measurements of Healy et al. [2012] showed that particles from different sources may have different compositions, and particles with local or transported origins have distinct mixing states [Healy et al., 2013]. The mixing state of particles may influence aerosol properties, such as absorption and scattering properties [Lesins et al., 2002b; Mallet et al., 2004], as well as the global radiative forcing [Jacobson, 2001]. By influencing the particle composition, the mixing state also influences the hygroscopicity and the potential of particles to be activated as cloud condensation nuclei [Wex et al., 2010; Lance et al., 2013; Leck and Svensson, 2014].

To simulate the evolution of externally-mixed particles by aerosol dynamics (coagulation and condensation/evaporation), models of different complexity have been developed. Limited by the complexity and computational abilities, most of the earlier attempts are 0D box models [Jacobson et al., 1994; Russell and Seinfeld, 1998; Jacobson, 2002a; Lu and Bowman, 2010; Dergaoui et al., 2013; Zhu et al., 2015a]. In the 3-d eulerian model of Kleeman and Cass [2001], each source is associated to an aerosol distribution. The different aerosol distributions are transported in the atmosphere, but they only interact with the gas phase by condensation and evaporation. In the global atmospheric models of Stier et al. [2005] and Bauer et al. [2008], the aerosol distribution is represented by mixed and unmixed modal modes of predefined compositions. Oshima et al. [2009b] discretized into sections both the particle size distribution and the fraction of black carbon in the total particulate mass. However they did not model coagulation. Riemer et al. [2009] model externally-mixed particles using a stochastic approach. Although this approach is accurate and takes into account coagulation as well as condensation/evaporation, it is computationally expensive when the number concentration of particles is high, limiting its 3-d applications.

Extended from the discretization scheme of Dergaoui et al. [2013], the Size-Composition Resolved Aerosol Model (SCRAM) [Zhu et al., 2015a] solves the aerosol dynamic evolution for external mixtures taking into account the processes of coagulation, condensation/evaporation and nucleation. In this work, the SCRAM model is integrated into the Polyphemus air-quality modelling platform, and its performance to model air quality

over Greater Paris is evaluated by comparison to the measurements obtained during the Megapoli campaign in July 2009. The impact of the mixing-state assumption on aerosol formation, composition as well as on aerosol optical properties and ability to be activated as cloud condensation nuclei is investigated.

3.2 Model description and simulation setup

SCRAM uses the sectional representation to discretize the particle size distribution. Within each size section, the composition of particles is also discretized. For a given chemical component or aggregate of chemical components, the mass fraction is discretized into mass fraction sections. The possible combinations of the mass fraction sections of each chemical component or aggregate of chemical components are generated to define all possible particle compositions. A combination of mass fractions is possible only if the sum of the lower bound of each fraction section within the combination is lower than 100%. In SCRAM, particle compositions can either be defined manually or automatically generated by giving the number of mass fraction sections of each chemical component or aggregate of chemical components. Three aerosol dynamic processes are taken into account in SCRAM: coagulation, condensation/evaporation and nucleation. The parametrisation of Vehkamäki et al. [2002] for the homogeneous binary nucleation of sulphate and water is used to simulate nucleation. For coagulation, the collisions of particles caused by Brownian motion is simulated using the module developed by Dergaoui et al. [2013]. Three different approaches may be used in SCRAM for condensation/evaporation: the fully dynamic approach, the bulk equilibrium approach or the hybrid approach. The fully dynamic approach computes the mass transfer rate due to condensation/evaporation for each particle size and composition section. It is the most accurate of the 3 approaches but it has the largest computational cost. The bulk equilibrium approach computes the mass partition between the gas and the bulk particle concentration by assuming an instantaneous thermodynamic equilibrium. After this bulk condensation/evaporation, the bulk particle concentration is redistributed between the particle sections. The bulk equilibrium approach is more computationally efficient, but it is less accurate than the dynamic approach, because particles may not be at thermodynamic equilibrium with their surrounding and the composition identity of each particle is not considered during the computation. Finally, the hybrid approach provides a compromise by assuming bulk equilibrium for small particles while dynamically computing the mass transfer rate for large particles. In this work, after condensation/evaporation, the moving-center algorithm is used for mass-number redistribution among fixed size sections. For more details about the discretization method, the mathematical derivation and model validations please refer to Zhu et al. [2015a].

SCRAM was integrated into the Polair3D air quality model [Sartelet et al., 2007] of the Polyphemus air-quality platform [Mallet et al., 2007] for 3D simulation over the Paris area. The Carbon Bond 05 model (CB05) [Yarwood et al., 2005] is used for gas phase chemistry. The thermodynamic model used for condensation/evaporation of inorganic aerosol is ISORROPIA [Nenes et al., 1998], while the H₂O model [Couvidat et al., 2012] is used for the secondary organic aerosol (SOA) formation. Although the condensation/evaporation of inorganics may be computed dynamically, bulk equilibrium is always assumed for

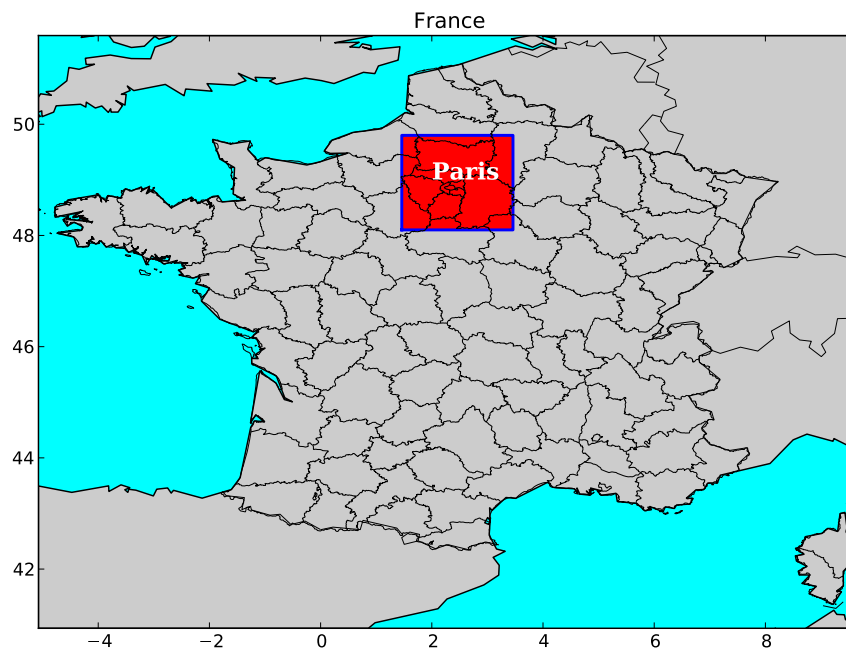


Figure 3.1: Simulated domain located within the red rectangle

organics, because a dynamic approach is not available in H_2O . For in-cloud processing of aerosols, the VSRM model [Fahey and Pandis, 2001] is used.

The Polair3D/Polyphemus air-quality model was modified to take into account both size and composition sections. The number of particles and the chemical components of each size/composition sections are transported. For input data, both initial and boundary conditions of the simulation can be specified as internally mixed (data without composition information) or externally mixed (data with composition information). In case of internally-mixed data, the composition index of each section is computed based on the composition of particles in that section. Emissions are considered as externally mixed (particles are only made of the emitted chemical component). Simulations in this work assume that initial and boundary conditions are internally mixed as they are obtained from a larger-scale simulation, which assumes that particles are internally mixed.

The simulation domain is the same as in Couvidat et al. [2013] and Wang et al. [2014]. As shown in figure 3.1, it covers the Paris area ($[1.2^\circ\text{E}, 3.5^\circ\text{E}] \times [47.9^\circ\text{N}, 50.1^\circ\text{N}]$) with a horizontal resolution of $0.02^\circ \times 0.02^\circ$, and 9 vertical layers from the ground to 12 000 m. The meteorology data are obtained from the Weather Research and Forecasting (WRF) [Skamarock et al., 2008] model using an urban canopy model and the Corine land-use data base [Kim et al., 2013] with the YSU parametrization [Hong et al., 2006] for the planetary boundary layer. Initial and boundary conditions inputs for aerosols and gas are from Couvidat et al. [2013], which were obtained from nested simulations over Europe and France. Biogenic VOC emissions are generated from the MEGAN emission model [Guenther et al., 2006], while anthropogenic emissions of gases and particles are obtained from the Airparif inventory [Airparif, 2010]. Four simulations are carried out for

Table 3.1: 20 Externally-mixed particle compositions

Composition Index	Pseudo Names	Mass fraction of each groups (%)			
		IL	OL	OB	EC
1	DUST	0-20	0-20	0-20	0-20
2	EC+	0-20	0-20	0-20	20-80
3	EC	0-20	0-20	0-20	80-100
4	OB+	0-20	0-20	20-80	0-20
5	OB+EC	0-20	0-20	20-80	20-80
6	OB	0-20	0-20	80-100	0-20
7	OL+	0-20	20-80	0-20	0-20
8	OL+EC	0-20	20-80	0-20	20-80
9	OM+	0-20	20-80	20-80	0-20
10	OM+EC	0-20	20-80	20-80	20-80
11	OL	0-20	80-100	0-20	0-20
12	IL+	20-80	0-20	0-20	0-20
13	IL+EC	20-80	0-20	0-20	20-80
14	IL+OB	20-80	0-20	20-80	0-20
15	IL+OB+EC	20-80	0-20	20-80	20-80
16	IL+OL	20-80	20-80	0-20	0-20
17	IL+OL+EC	20-80	20-80	0-20	20-80
18	IL+OM	20-80	20-80	20-80	0-20
19	IL+OM+EC	20-80	20-80	20-80	20-80
20	IL	80-100	0-20	0-20	0-20

one week from 28 June to 5 July 2009. The first two simulations assume that particles are internally mixed (IM), while the other two simulations simulate externally-mixed (EM) particles. Within each of the two groups of simulations, one simulation uses the fully dynamic approach for condensation/evaporation, while the other one uses the bulk equilibrium approach for solving condensation/evaporation.

The size distribution is discretized into 5 size sections between 0.01 and 10 μm . As in Zhu et al. [2015a], 31 aerosol species are grouped into 5 groups: inorganic hydrophilic (IL), organic hydrophilic (OL), organic hydrophobic (OB), black carbon (EC) and dust (DUST). The IL group includes sodium, sulphate, nitrate, ammonium and chloride. The 23 organic model species are divided into two groups (9 OB and 14 OL species) based on their hygroscopic characters as detailed in Couvidat et al. [2012]. EC and DUST contains respectively black carbon and dust. For the EM simulations, the mass fraction of each of the first four groups (IL, OL, OB, EC) is discretized into three mass-fraction sections ([0.0, 0.2],[0.2, 0.8],[0.8, 1.0]). In total 20 possible particle compositions are generated, as

presented in Table 3.1. DUST is not discretized and its mass fraction is obtained by mass conservation. The names assigned to the particle compositions are chosen depending on the main chemical groups (with mass fraction greater than 20%) of each composition. Particles with more than 80% of one chemical group are considered as unmixed, they are referred as DUST, EC, OB, OL and IL. Besides, EC+, OB+, OM+, OL+ and IL+ represent compositions that are partly mixed as they do not have a chemical group which dominates the mass fraction by more than 80%, but only one chemical group has a mass fraction larger than 20%. When both hydrophilic and hydrophobic organics are equally present in the composition, they are referred as organic matter (OM). In each group, water may also be present, although it is not considered when computing the mass fractions (it is calculated separately with the thermodynamic models).

3.3 Particle concentrations

This section analyses the simulated particle concentrations from all four simulations. First, $PM_{2.5}$ and PM_{10} are compared to observational data. The influences on $PM_{2.5}$ and PM_{10} of the mixing-state assumption and of the approach used to model condensation/evaporation (equilibrium vs dynamic) are investigated. Secondly, as only inorganic concentrations may be computed dynamically, a more specific analysis is performed on inorganic aerosol formation. Finally, the mixing state of EC is studied. Because EC is an inert species and it is emitted by traffic, which is an important source of pollution over Paris, it is a good candidate to demonstrate the ability of SCRAM to study the particle mixing state.

3.3.1 PM concentrations

The model performance to simulate PM concentration over Greater Paris is evaluated based on the criteria proposed by Boylan and Russell [2006]: PM performance goal is met when the mean fractional bias (MFB) is in range of [-30%, 30%] and the mean fractional error (MFE) is in range of [0%, 50%]; the PM performance criterion is met when the mean fractional bias (MFB) is in range of [-60%, 60%] and the mean fractional error (MFE) is in range of [0%, 75%]. The PM performance goal corresponds to the level of accuracy that is considered to be close to the best level that can be expected to achieve, while the PM performance criterion corresponds to the level of accuracy that is considered to be acceptable for modelling applications. The root-mean-square error (RMSE) and correlation coefficient are also used as statistical indicators in this work. Definitions about MFB, MFE, RMSE and correlation are detailed in table 3.2.

Statistics of the four simulations are presented in table 3.3 for both $PM_{2.5}$ and PM_{10} . For all the simulations, the PM performance goal is met for $PM_{2.5}$ and the PM criterion is met for PM_{10} . In other words, the model simulates well $PM_{2.5}$, while PM_{10} is slightly under estimated as expected from the former simulations which use the same setup and input data [Couvidat et al., 2013; Wang et al., 2014]. The reasons for this underestimation of coarse particles may be that re-suspension is not modelled and dust boundary conditions may be underestimated.

Although the statistics of the different simulations are very similar, they are always better for the dynamic approach than for the equilibrium approach no matter what mixing

Table 3.2: Definitions of the statistics used in this work. $(o_i)_i$ and $(c_i)_i$ are the observed and the model concentrations at time and location i , respectively. n is the number of data

Statistic indicator	Definition
Root mean square error (RMSE)	$\sqrt{\frac{1}{n} \sum_{i=1}^n (c_i - o_i)^2}$
Correlation	$\frac{\sum_{i=1}^n (c_i - \bar{c})(o_i - \bar{o})}{\sqrt{\sum_{i=1}^n (c_i - \bar{c})^2} \sqrt{\sum_{i=1}^n (o_i - \bar{o})^2}}$
Mean fractional bias (MFB)	$\frac{1}{n} \sum_{i=1}^n \frac{c_i - o_i}{(c_i + o_i)/2}$
Mean fractional error (MFE)	$\frac{1}{n} \sum_{i=1}^n \frac{ c_i - o_i }{(c_i + o_i)/2}$

Table 3.3: Statistics between simulation results and the measurements of the BDQA (Base de Données sur la Qualité de l Air) network during the MEGAPOLI summer experiment. (Obs. stands for observation. Sim. stands for simulation. Corr. stands for correlation.)

Simulations	PM _{2.5}					
	Obs.	Sim.	RMSE	Corr.	MFB	MFE
	mean	mean				
	$\mu\text{g m}^{-3}$	$\mu\text{g m}^{-3}$	$\mu\text{g m}^{-3}$	%	%	%
Internal-eq	21.35	17.15	9.5	56.5	-15.8	32.8
Internal-dy	21.35	17.14	9.6	56.1	-15.4	32.7
External-eq	21.35	17.18	9.5	56.5	-15.6	32.7
External-dy	21.35	17.42	9.3	57.9	-13.9	31.9
Simulations	PM ₁₀					
	Obs.	Sim.	RMSE	Corr.	MFB	MFE
	mean	mean				
	$\mu\text{g m}^{-3}$	$\mu\text{g m}^{-3}$	$\mu\text{g m}^{-3}$	%	%	%
Internal-eq	35.54	18.96	23.3	36.3	-53.8	59.4
Internal-dy	35.54	19.11	23.2	34.7	-52.7	58.5
External-eq	35.54	18.97	23.3	36.2	-53.7	59.3
External-dy	35.54	19.35	22.9	38.5	-51.6	57.4

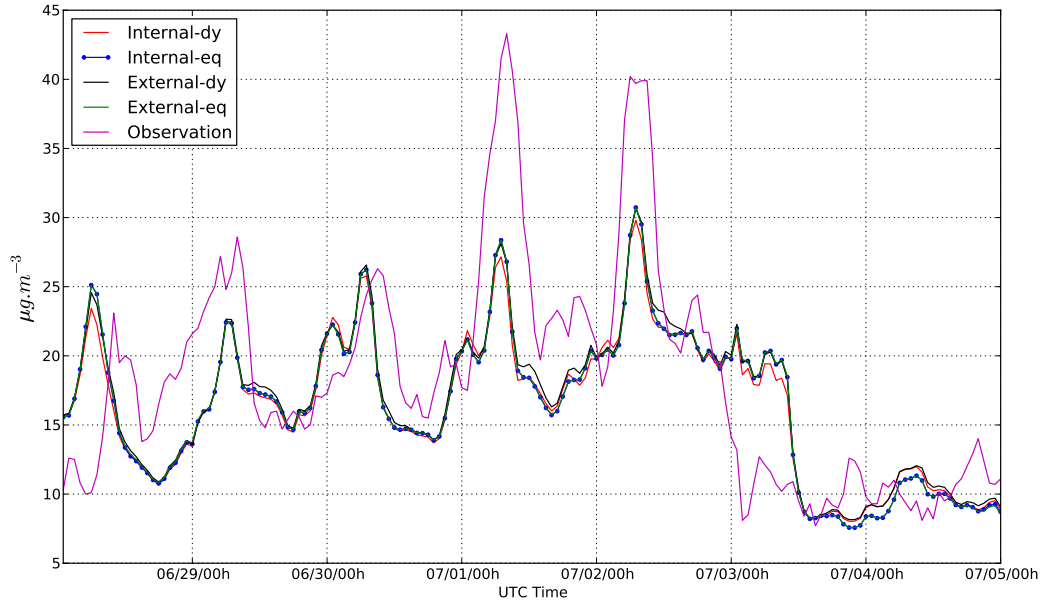


Figure 3.2: Time evolution of $\text{PM}_{2.5}$ at BDQA site Gennevilliers (48.93°N , 2.29°E) between 28 June and 5 July 2009

assumption is used. Besides, in general EM simulations have better statistics than the IM ones, especially with the dynamic approach, partly because the EM simulations lead to slightly higher PM concentrations than the IM simulations. This is a consequence of differences of inorganic aerosol concentrations, as discussed in the next section.

The dynamic approach leads to larger differences between the IM and EM simulations than the equilibrium approach. This can be observed from Figures 3.2 and 3.3, where the time evolutions of $\text{PM}_{2.5}$ and inorganic concentrations at Gennevilliers (48.93°N , 2.29°E) (marked in Figure 3.4) respectively are presented for the four simulations. The concentrations from IM and EM simulations are similar when bulk equilibrium is assumed, because the mass transfer by condensation/evaporation between particles and gas depends on the total bulk mass of inorganic components and it is independent of the mixing state. Condensation/evaporation is the main process leading to differences in the mixing state here, because internal and external mixing simulations have the same initial and boundary concentrations. Furthermore, coagulation and transport treat similarly all particles, independently of their mixing state. Under the dynamic approach, the mass transfer rate varies with particle composition during condensation/evaporation, leading to differences in PM concentrations between IM and EM simulations. Because only the condensation/evaporation of inorganics is computed dynamically here, the differences of $\text{PM}_{2.5}$ concentrations between the IM and EM simulations are relatively low. Because organics may not be at thermodynamic equilibrium [Couvidat and Sartelet, 2015] and because they make a significant part of the total particle mass, larger differences would be observed if the condensation/evaporation of organics is computed dynamically.

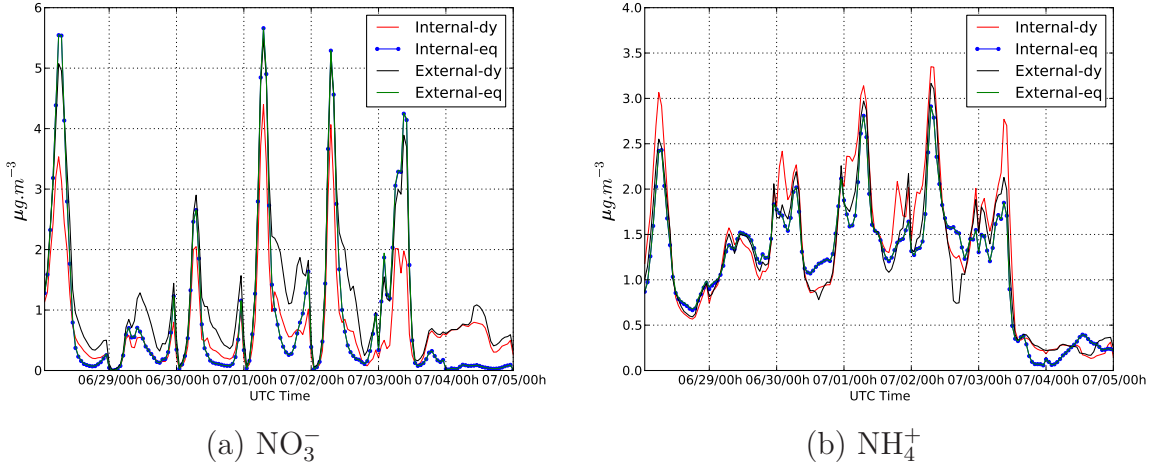


Figure 3.3: Time evolution of NO_3^- and NH_4^+ at BDQA site Gennevilliers (48.93°N , 2.29°E) between 28 June and 5 July 2009

3.3.2 Inorganic aerosol formation

The impact of the mixing state assumption and the condensation/evaporation approach on the formation of inorganic aerosols is studied here, with a focus on nitrate and ammonium. The sodium and sulphate concentrations are found to be very similar for all simulations, because they are not volatile (with an averaged concentration of $0.165 \mu\text{g m}^{-3}$ for sodium and $3.11 \mu\text{g m}^{-3}$ for sulphate). Chloride is ignored in the comparison because its concentration is very small.

Figure 3.3 compares the time evolution of nitrate (NO_3^-) and ammonium (NH_4^+) between the four simulations at Gennevilliers. For both the EM and the IM simulations, the dynamic approach for condensation/evaporation leads to lower peaks and higher troughs for NO_3^- , but higher peaks and lower troughs for NH_4^+ , compared to the bulk equilibrium approach. Similarly to the $\text{PM}_{2.5}$ concentration results, if bulk equilibrium is assumed for condensation/evaporation, the mixing-state assumption makes almost no difference on both NO_3^- concentrations ($0.88 \mu\text{g m}^{-3}$ in average) and NH_4^+ ($1.19 \mu\text{g m}^{-3}$ in average). Using the dynamic approach for condensation/evaporation, EM leads to higher NO_3^- concentration ($1.24 \mu\text{g m}^{-3}$ in average) than IM ($0.76 \mu\text{g m}^{-3}$ in average) and lower NH_4^+ concentrations ($1.23 \mu\text{g m}^{-3}$ in average) than IM ($1.33 \mu\text{g m}^{-3}$ in average). Furthermore, the differences are especially high for peak concentration. Between 3 July and 4 July, the peak concentration of NO_3^- for the EM simulation is twice the one for the IM simulation. Using the dynamic approach, the impact of the mixing-state assumption is larger (average difference of $0.48 \mu\text{g m}^{-3}$ for NO_3^- and $0.1 \mu\text{g m}^{-3}$ for NH_4^+) than the impact of the condensation/evaporation approach (average difference of $0.35 \mu\text{g m}^{-3}$ for NO_3^- and $0.04 \mu\text{g m}^{-3}$ for NH_4^+ with external mixing).

Because sulphate concentrations do not change between the IM and EM simulations, an increase of NO_3^- would lead to an increase of NH_4^+ if bulk equilibrium is considered for condensation/evaporation. However, in the EM simulations, NH_4^+ decreases because the amount neutralized by sulphate is lower. This leaves more ammonia available to react with nitric acid, leading to an increase of NO_3^- . For a better understanding, let us

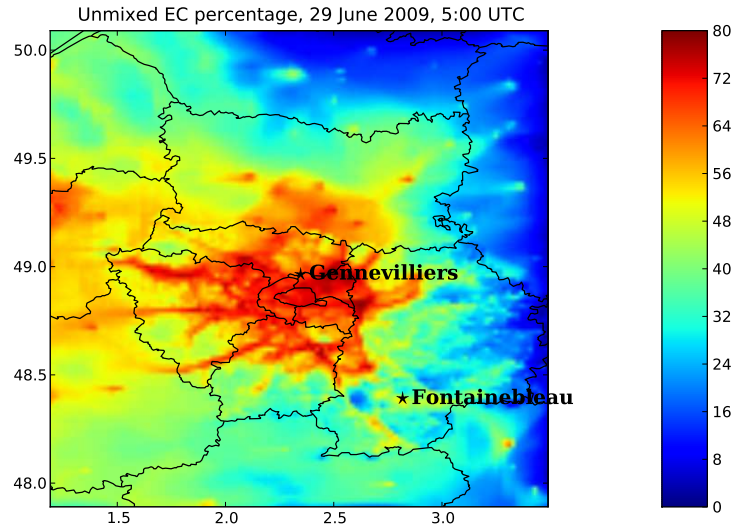


Figure 3.4: Spatial distribution of EC mixing state over Paris region

define $[TA]$, $[TS]$, and $[TN]$ the total (gas + particle) molar concentrations of ammonium, sulphate, and nitrate, respectively. Two different chemical environments around particle surface may exist. If $[TA] > 2 [TS]$, then the local environment is ammonia rich, and all sulphate is in the form of $(NH_4)_2SO_4$. On the contrary, if $[TA] < 2 [TS]$, then the environment is ammonia-poor, sulphate is not fully neutralized and it may be in the form of both $(NH_4)_3H(SO_4)_2$ and $(NH_4)_2SO_4$. Because $(NH_4)_3H(SO_4)_2$ has lower NH_4^+ to SO_4^{2-} ratio than $(NH_4)_2SO_4$, less NH_4^+ is formed in ammonia-poor environment than in ammonia-rich environment. In the IM simulation, within a size section, the mass of sulphate is the same for each particle, and each particle neutralizes the same amount of ammonia. Once sulphate is fully neutralized, then the remaining ammonia reacts with nitric acid to condense, which means that ammonium nitrate can only be formed under an ammonia-rich environment. However, in the EM simulation, particles may contain different amounts of sulphate. For particles that contain a high fraction of sulphate, the local environment may be ammonia poor, reducing the amount of ammonium neutralized by sulphate compared to the IM simulation, and increasing the amount of ammonia available for particles that contain a low fraction of sulphate. For those particles, more ammonia is left in the gas phase after neutralization of sulphate, favouring the formation of $NH_4^+NO_3^-$ and leading to more nitrate in the particle phase than in the IM simulation.

3.3.3 Mixing state of EC

The external mixing model provides the opportunity to investigate particle mixing state. As EC is an inert component of particles and as it is the most strongly light-absorbing one, the mixing state of EC is studied here, using the EM simulation with the dynamic approach.

We define the unmixed EC percentage as the ratio of the EC mass of unmixed EC

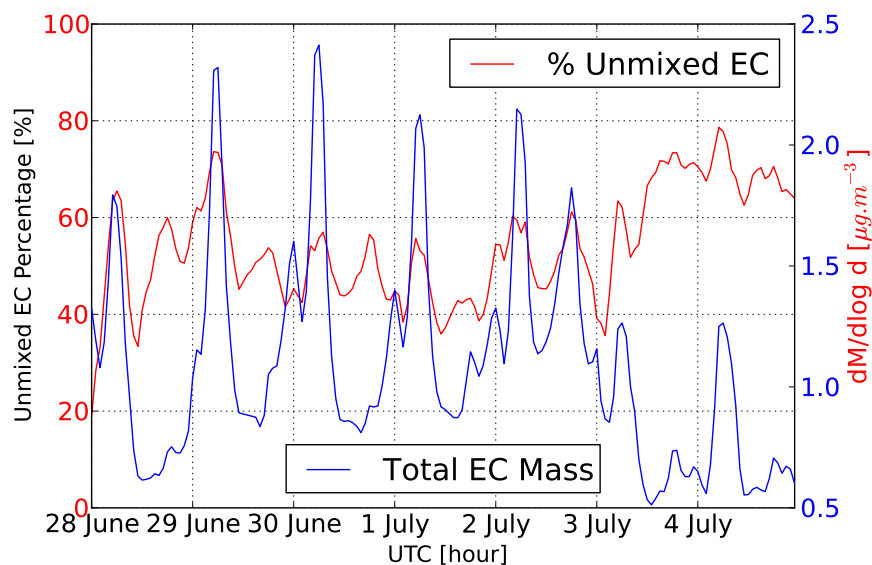


Figure 3.5: Temporal evolution of EC mixing state over Paris region

particles to the EC mass of all particles. Figure 3.4 shows the spatial distribution of the unmixed EC percentage during the morning rush hour at 5:00 AM UTC on 29 June 2009. Regions with strong traffic emissions have high unmixed EC percentages, such as the highways and ring roads around the city. Up to 80% of the EC mass may be unmixed. Figure 3.5 shows the time evolution of the total EC mass as well as the unmixed EC percentage at an urban site Gennevilliers. These two curves are strongly correlated: the unmixed EC percentage is the highest when the total EC mass is the highest, mostly during morning rush hours. Peaks of unmixed EC percentages are also observed in the late afternoon during the evening rush hours, although the increase of the total EC mass during the evening rush hours is low. Between 28 June and 3 July, the unmixed EC percentage does not drop to low values: it is higher than 35% with a peak at 72%. Between 3 July and 4 July, the unmixed EC percentage increases to values above 60% with a peak at 80%. This is caused by a strong wind event on 3 July, which clears out most of the background particles and the total EC mass is lower than between 28 June and 3 July. The same decrease can also be observed in the time evolution of $PM_{2.5}$ in Figure 3.2. Particles are therefore less mixed on 3 and 4 July than between 28 June and 3 July.

The EC mixing state at an urban and a rural sites is compared in Figure 3.6, which presents the week-averaged partition of EC mass amongst the particle types at both the urban site of Gennevilliers and the rural site of Fontainebleau (48.35 N°, 2.77 E°) (south east of Paris, see Figure 3.4). At the urban site, more than half (53.8%) of the total EC mass is unmixed on average, whereas at the rural site, only 32.2% of the total EC mass is unmixed. EC particles are more mixed at the rural site, because it is further apart from emission sources, such as traffic emissions. At both the urban and the rural sites, a large percentage of mixed EC particles contains inorganic species (IL), which are often mixed with organics (IL+OB, IL+OL, and IL+OM). A larger percent of EC particles

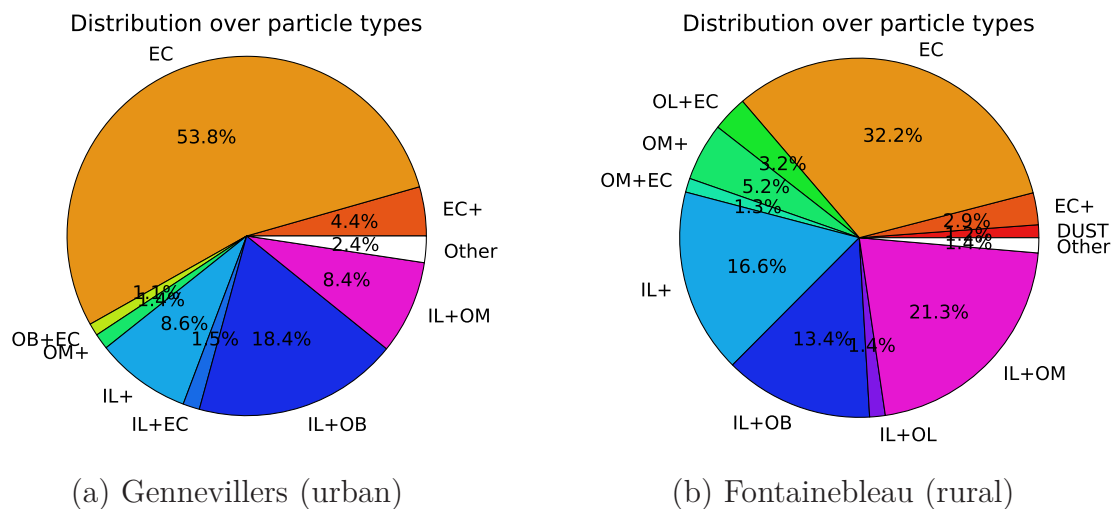


Figure 3.6: Comparison between partition of EC mass amongst the particle types at urban and rural site (Week averaged at ground level)

are mixed with organics (9.7% of OM+, OM+EC, and OL+EC) at the rural site than at the urban site (2.5% of OM+ and OB+EC). This may correspond to stronger biogenic emissions and higher SOA concentrations at the rural site.

3.4 Aerosol optical properties

Particles attenuate the solar radiation, influencing the earth radiative budget and affecting the climate. This attenuation is modelled using aerosol optical properties, such as the Aerosol Optical Depth or Thickness (AOD / AOT) and the Single Scattering Albedo (SSA). The AOD represents the attenuation of solar radiation, while the SSA represents the importance of scattering during such attenuation. Both the AOD and SSA values are determined by the vertical particle concentrations. They depend on the size, the composition and the mixing state of particles. In this section, the computation of aerosol optical properties is first detailed. The AOD values are then compared to AERONET measurements, and the influence of the mixing-state assumption is studied. Finally, the particle types that contribute the most to high AOD values are determined. AODs and SSAs are computed from the concentrations of both the IM and EM simulations with the dynamic approach (AOD_{int} and AOD_{ext} ; SSA_{int} and SSA_{ext}).

3.4.1 Computation of aerosol optical properties

When light reaches a particle, it might be scattered into other directions or absorbed by particles. The ability to scatter or absorb radiations is described by the extinction coefficient $b_{ext} = b_{scat} + b_{abs}$ which depends on both the size and composition of particles. The Complex Refractive Index (CRI) is used to represent the optical property of each particle chemical component. It is a complex number whose real part describes the scattering ability of the component while the imaginary part describes the absorbing ability. The CRI are sensitive to the wavelength of incident light, in this study the optical properties at

Table 3.4: CRI of simulated species at $\lambda=550$ nm in dry state

Species	Real	Imaginary
Nitrate	1.60	0.0
Ammonium	1.53	-6.0×10^{-3}
Sulphate	1.53	0.0
Sodium	1.50	-1.0×10^{-8}
Chlorate	1.50	-1.0×10^{-8}
EC	1.95	-0.79
Mineral Dust	1.52	-1×10^{-3}
Hydrophilic Organics	1.53	-6.0×10^{-3}
Hydrophobic Organics	1.53	-8.0×10^{-3}

550 nm are investigated. Table 3.4 shows the CRI used in this study. They are obtained from the ADIENT/APPRAISE technical report (<http://www.met.rdg.ac.uk/adiant>) for inorganics and from the OPAC software package [Hess et al., 1998] for organics (water soluble type for hydrophilic organics and insoluble for hydrophobic organics).

Because particles are often made of several chemical components, an Aerosol Complex Refractive Index (ACRI) is determined from the CRI. Two methods may be used to do so: one method assumes that the chemical components are well mixed, and the other assumes that EC is a non-mixed core at the center of each EC containing particles. In the first method, the ACRI is computed by a simple volume averaged procedure. The second method uses the Maxwell-Granett approximation [Maxwell, 1904]. After computed the ACRI value m , the extinction and the scattering coefficients are computed based on the Mie theory [Mie, 1908], using the Mie code of Bohren and Huffman [1983]. Finally the AOD and the aerosol scattering depth (ASD) at a wavelength λ are calculated as the integral of the extinction coefficient and the scattering coefficient respectively through the vertical of atmosphere. The single scattering albedo (SSA) is defined by $\frac{ASD}{AOD}$. The algorithm for computing the AOD and aerosol optical properties is obtained from Tombette et al. [2008] and Wang et al. [2014].

3.4.2 Comparisons to AERONET measurements

AERONET (AErosol RObotic NETwork) is a ground-based remote sensing network, with aerosol optical measurements performed by sun photometers [Holben et al., 1998]. Its database provides accurate AOD measurements at different wavelengths, with a measurement uncertainty lower than 0.02 [Holben et al., 2001]. Three data quality levels are available: level 1.0 (unscreened), level 1.5 (cloud-screened), and level 2.0 (cloud-screened and quality assured). Three AERONET stations are available over Greater Paris: one urban station Paris (48.87° N, 2.33° E; 50 m a.s.l.) and two suburban stations Palaiseau (48.70° N, 2.21° E; 156 m a.s.l.) and Créteil (48.78° N, 2.44° E; 59 m a.s.l.) (marked in Figure 3.8). In this study, level 2.0 AOD data at 500 and 675 nm are used to derive

Table 3.5: Statistics between AOD values computed from simulation results and the measurements of the AERONET. (Obs. stands for observation. Sim. stands for simulation. Corr. stands for correlation.)

Simulations	Obs. mean	Sim. mean	RMSE	Corr.	MFB	MFE
Internal-core	0.30	0.28	0.18	49.3%	-14.4%	38.7%
Internal-mix	0.30	0.29	0.18	48.2%	-11.9%	37.8%
External-core	0.30	0.28	0.18	49.2%	-16.1%	39.3%
External-mix	0.30	0.28	0.18	48.3%	-13.6%	38.2%

AOD_{obs} data at 550 nm following the Ångström law:

$$AOD(550) = AOD(500) \times \left(\frac{550}{500}\right)^{-\alpha} \quad (3.1)$$

with α the Ångström exponent:

$$\alpha = \ln\left(\frac{AOD(500)}{AOD(675)}\right) / \ln\left(\frac{675}{500}\right). \quad (3.2)$$

Table 3.5 presents the statistics of the comparison of computed AOD values to AERONET measurements at the three available stations. Internal-core and external-core denote results of respectively the IM and EM simulations, with AOD computed using the EC core hypothesis. Internal-mix and external-mix denote results of respectively the IM and EM simulations, with AOD computed using the well-mixed hypothesis. The statistics of results with different mixing states (internal-core, external-core, internal-mix and external-mix) are similar. Simulated AODs compare well to measurements, with a mean simulated value of 0.28 and a mean observed value of 0.30. The correlations are between 48% and 50%. The MFB and MFE values satisfy the model performance goal criterion of Boylan and Russell [2006]. Figure 3.7 shows the daily variations of AOD and SSA at the urban station Paris. AOD values are very similar for internal-core, external-core, internal-mix and external-mix and the daily variations compare well to observations. Both the simulated and the observed AOD are highest in 2 July and lowest in 30 June. Higher differences between the results of different mixing states are observed for SSA at the station Paris. The next section studies in more details the influence of the mixing state on AOD and SSA at the station Paris and over the domain of study (Greater Paris).

3.4.3 Influence of the mixing state

Because the AERONET station Paris is located down-town Paris where particles and especially EC are largely unmixed, it is a good location to study the influence of the particle mixing state on AOD and SSA. As discussed in the previous section, Figure 3.7 shows that the influence of the mixing state is larger on SSA than on AOD at Paris. Using the same AOD computation method (core or mix), the IM simulation leads to higher AOD values and lower SSA values than the EM simulation. However, for the same mixing-state assumption in the simulation, the EC core hypothesis in the AOD

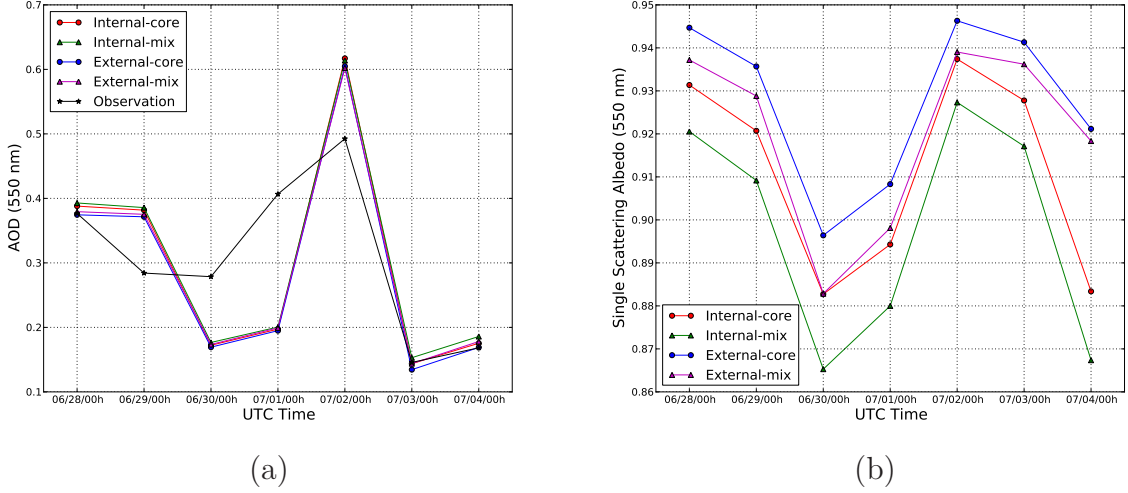


Figure 3.7: (a) Comparison of AOD between different mixing assumptions and the observation; (b) comparison of SSA between internal and external mixing case; Both plot is based on the data collected from the location of AERONET site Paris (48.87° N, 2.33° E; 50 m a.s.l.)

computation method leads to slightly lower AOD and higher SSA than the well-mixed hypothesis. However, the differences are lower than differences between the EM and IM simulations using the same AOD computation method.

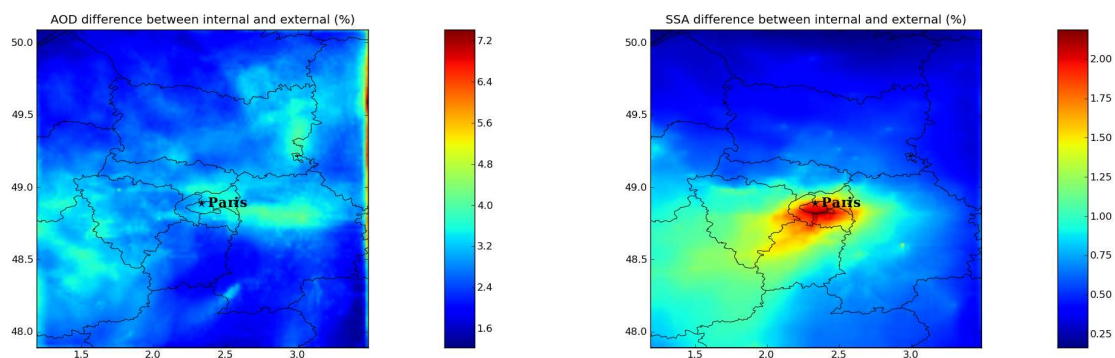
The higher SSA values and lower AOD values observed for externally-mixed EC particles are explained by the fact that for a given mass of EC within a particle, its absorption cross section is greater when other non-absorbing materials are also present than when the particle is made of pure EC. Hence, as discussed in Seinfeld and Pandis [2012], in the EM simulations, EC is highly concentrated in several EC dominated particle types, while EC is present in all particles in the IM simulations, leading to larger total absorption cross sections and larger absorption effects.

The influence on SSA is in good agreement with the results of Mallet et al. [2004], which indicate that IM reduces SSA by about 15% compared to EM. The SSA difference between different mixing assumptions is lower in this study than in Mallet et al. [2004], because in Mallet et al. [2004] SSA is computed by assuming that EC is either completely mixed or not mixed at all with other components. However, in our EM simulations, EC can have different mixing states (see section 3.3.3).

Figure 3.8 shows the spatial distribution of the weekly averaged AOD and SSA differences between the IM and EM simulations with the well-mixed hypothesis for optical calculations. Using the EC core rather than the well-mixed hypothesis leads to slightly lower differences for AOD and SSA between the IM and EM simulations (about 2.0% lower for AOD and about 0.7% lower for SSA). AOD and SSA differences are calculated using the following equation:

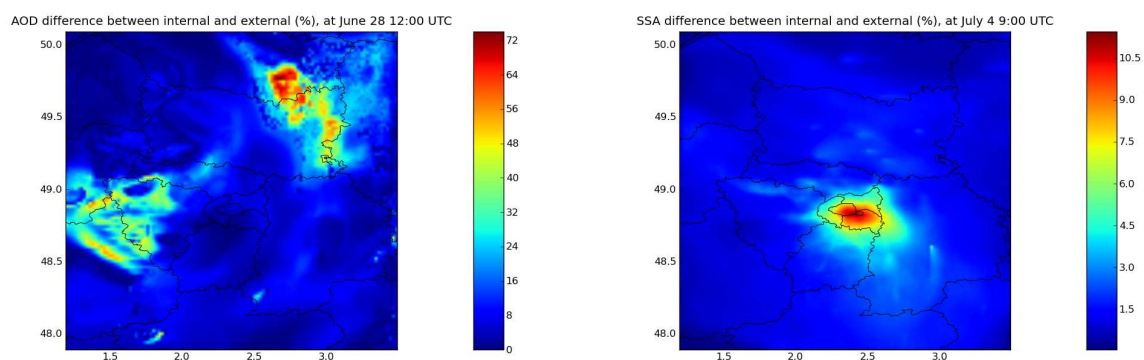
$$Difference = \left| \frac{\omega_{ext} - \omega_{int}}{\omega_{int}} \right| \times 100\% \quad (3.3)$$

where ω_{int} and ω_{ext} are either AOD or SSA obtained from the IM and EM simulations



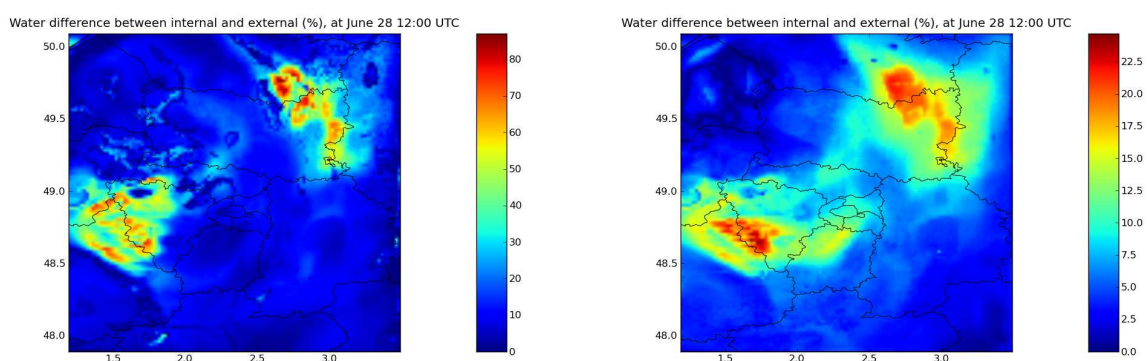
(a) Weekly averaged AOD difference (%)

(b) Weekly averaged SSA difference (%)



(c) Maximum AOD difference (%)

(d) Maximum SSA difference (%)



(e) Water difference (%)

(f) Inorganics difference (%)

Figure 3.8: Spatial distribution of differences between different mixing assumptions of different parameters

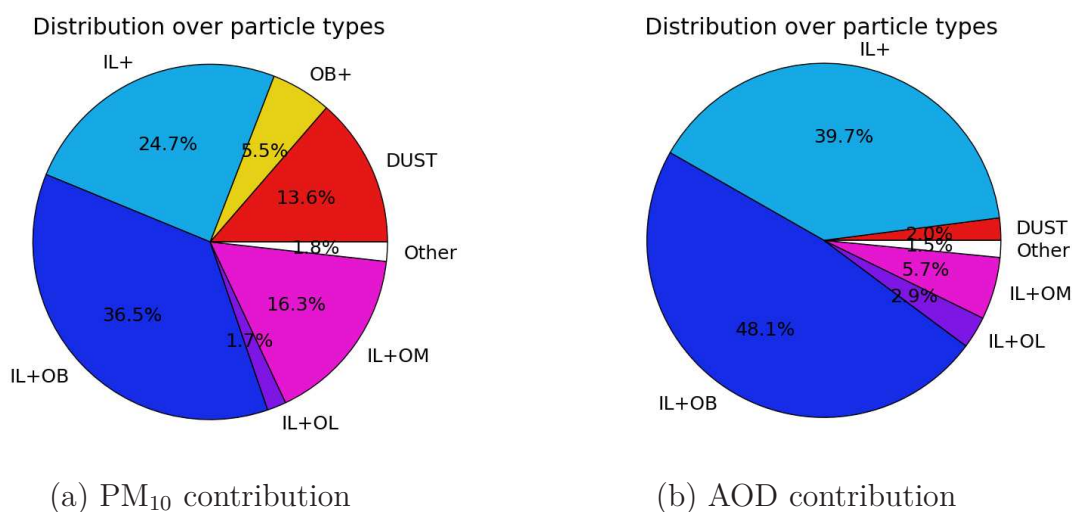


Figure 3.9: (a) Averaged mass fraction of each particle types (all level); (b) Averaged AOD fraction contribute by each particle types

respectively. For SSA, the larger differences between IM and EM are concentrated in the city of Paris, where a large percentage of EC is unmixed in the EM simulation, affecting the absorption and scattering properties of particles. Although, on average over the week of simulation, the highest SSA difference is only 2.15%, Figure 3.8 (d) shows that for specific time periods (e.g. during rush hour at 9:00 AM on 4 July when 80% of EC is unmixed) the difference can be as high as 10.7%. For AOD, differences between IM and EM are rather low over the city of Paris, but they are high over some regions such as the north east and the south west of Paris. Although the weekly-averaged AOD difference is at most of 7.25%, the hourly-averaged difference can be as high as 72.5%, for example at 12:00 AM on 28 June (see Figure 3.8 (c)). The differences in AOD are mostly related to differences in mass concentrations between the IM and EM simulations. Water plays an important role in light scattering and the AOD difference is mostly caused by the difference of aerosol water content. Indeed, the comparison of Figures 3.8 (c), 3.8 (e) and 3.8 (f) shows that the AOD difference is strongly correlated to difference in aerosol water concentration, and also correlated to difference in inorganic concentrations, although the correlation to the difference in inorganic concentrations is not as high as the correlation to difference in water concentration. Differences in inorganic concentrations result from differences in the mixing-state assumption as discussed in section 3.3.2, and they lead to differences in water aerosol concentration, which is computed based on inorganic aerosol concentrations using ISORROPIA. As shown in Figures 3.8 (e) and 3.8 (f), a difference of 22% in inorganic concentrations can lead to differences as high as 80% in water concentration and 72% in AOD.

3.4.4 Contributions of particle types

Figure 3.9 compares the contribution of each particle type to PM₁₀ and AOD. Particles containing inorganic species (IL+OB and IL+) are the main contributors to AOD, with a contribution fraction of 88%. Their contribution to PM₁₀ is lower, although high (60%). Besides, there are only three particle types whose AOD contribution exceed their

mass contribution: IL+, IL+OB and IL+OL. Let us define the ratio between the AOD contribution fraction (AOD_{frac}) and the PM_{10} contribution fraction (PM_{frac}) as the AOD contribution efficiency (AOD_{eff}) of one particle type: $AOD_{eff} = \frac{AOD_{frac}}{PM_{frac}} \times 100\%$. The IL+OL particles have the highest AOD contribution efficiency (170.6%), followed by the IL+ particles (160.7%) and the IL+OB particles (131.8%). This is a consequence of the hygroscopic property of particles. For a given dry particle diameter, hydrophilic particles have a larger water concentration than hydrophobic particles, thus larger wet diameter, leading to higher particle scattering ability. Therefore, the particle types with the three highest AOD contribution efficiency contain inorganic hydrophilic species and the particle type containing both inorganics and hydrophilic organics (IL+OL) has the highest AOD contribution efficiency. Although the contribution of unmixed EC particles is not large enough to be seen in Figure 3.9 (b), further analyse reveals that with less than 0.45% of the total PM mass, the unmixed EC particles contribute to around 2.1% of the total AOD.

3.5 Cloud Condensation Nuclei

Cloud condensation nuclei or CCN are particles that can become cloud droplets by condensation of water vapour when the surrounding atmosphere is supersaturated. They are very important for cloud formation, as they provide the non-gaseous surface which is necessary for water vapour to condense. Without such surface, the spontaneously nucleation of water vapour is very difficult. In above freezing temperatures the air would have to be supersaturated to around 400% before the droplets could form without the presence of CCN [?]. Based on Köhler equation [Köhler, 1921; Köhler, 1926], the percentage of particles that are activated as cloud droplets is controlled by both particle wet diameter (Kelvin effect) and composition (solute effect). The Kelvin effect is related to the curvature of particles: the surface vapour pressure is higher for particles of lower diameter, inhibiting the condensation of water vapour. The solute effect decreases the surface vapour pressure depending on the dissociation ability of the chemical components of the particle. Hydrophilic particles are more easily activated than hydrophobic particles. Because the mixing state of particles influences the particle composition and water content as seen in the previous section, its impact on the formation of CCN may be important. This section first explains briefly the activation of particles in CCN. Then, the impact of the mixing state on the formation of CCN is studied, as well as the contribution of the different particle types to the CCN formation.

3.5.1 Computation of CCN

A particle is activated into a cloud droplet when the supersaturation of its surrounding environment is larger than a critical supersaturation s_c , which depends on the size and the composition of the particle [Seinfeld and Pandis, 1998]:

$$s_c = \exp\left[\left(\frac{4A^3 \rho_w M_s}{27\nu \rho_s M_w d_s^3 f_{vs}}\right)^{1/2}\right] - 1 \quad (3.4)$$

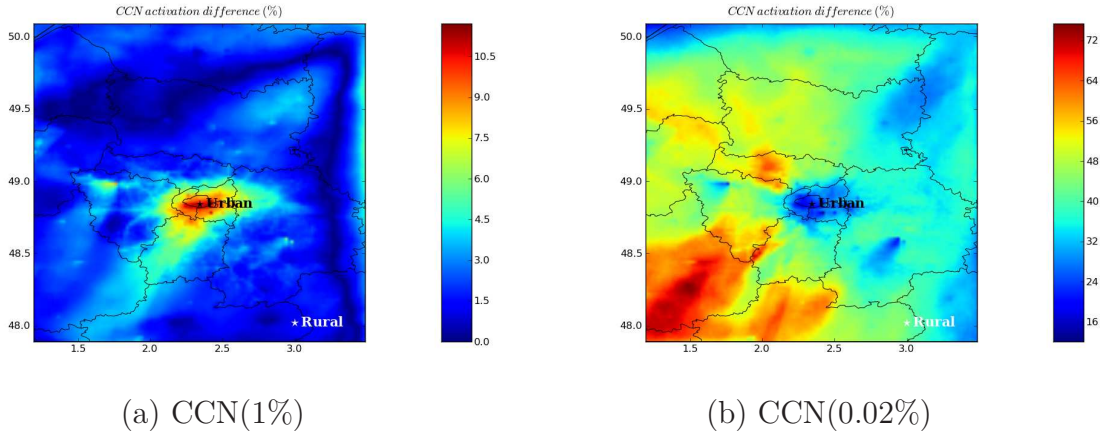


Figure 3.10: Spatial distribution of weekly averaged CCN activation percentage differences (%) between internal and external mixing under (a) high supersaturation (1%), (b) low supersaturation (0.02%)

where $A = \frac{4M_w\sigma_w}{RT\rho_w}$, d_s is the particle dry diameter, f_{vs} is the volume fraction of soluble components, ν is the Van't Hoff factor, which represents the averaged number of ions resulting from the dissociation of one solute molecule, M_s and M_w are the molecular weights of solute and water respectively, ρ_s and ρ_w are their densities, T is the temperature, R is the ideal gas constant, and σ_w the water air surface tension.

In this study, only the species of groups IL and OL are considered as soluble species, others are considered as insoluble. The routine of Nenes and Seinfeld [2003] is used for computing the critical supersaturation s_c of particles based on their size and composition. As the computation of CCN is very sensitive to particle size, each size section is divided into 10 size sections of same composition to obtain a smooth CCN spectrum. The number of CCN is computed at six hypothetical supersaturation (0.02, 0.005, 0.1, 0.2, 0.5, 1.0) for the whole simulation domain. Then, the CCN activation percentage is computed based on the ratio of the number of particles that have been activated as CCN to the total number of particles.

3.5.2 Impact of the mixing state on CCN

To investigate the impact of the mixing state on CCN, CCN activation percentages are computed at different supersaturations for both the IM and EM simulations. Figure 3.10 shows the spatial distribution of the difference between IM and EM simulations of the absolute value of the weekly-averaged CCN activation percentage at a high supersaturation (1%) and at a low supersaturation (0.02%). This CCN activation difference is computed based on equation (3.3) by replacing ω_{int} and ω_{ext} by the CCN activation percentage computed from the IM and EM simulations respectively. The absolute value of the CCN activation percentage difference between IM and EM simulations is lower at 1% supersaturation (between 0 and 11%) than at 0.02% supersaturation (between 12 and 75%), because at 1% supersaturation, hydrophobic particles are more easily activated than at 0.02%, reducing the impact of differences of particle compositions. The spatial

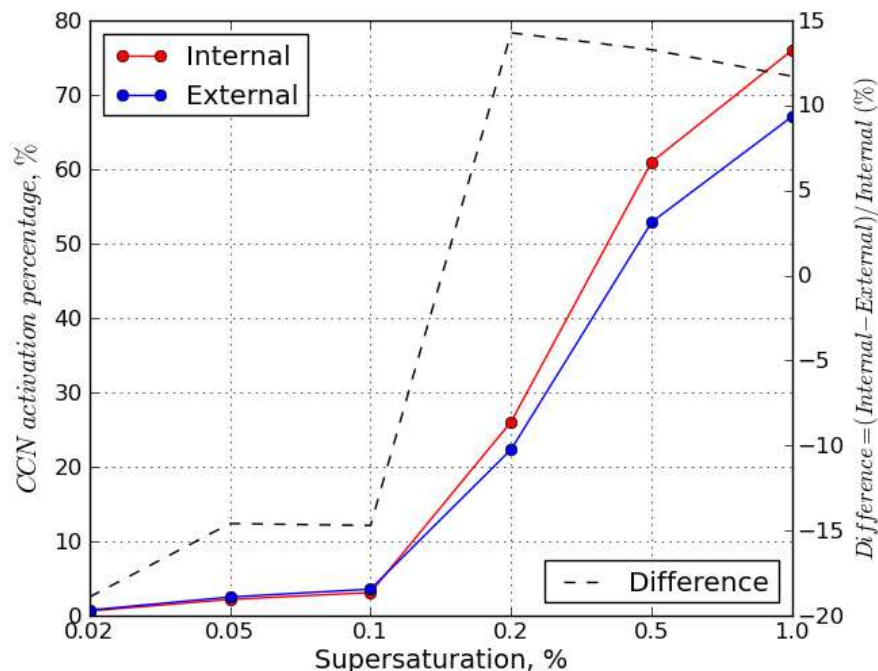


Figure 3.11: Averaged CCN activation percentage and CCN activation difference (%) for different supersaturation % at urban site.

pattern of the absolute value of the CCN activation percentage difference is also very different at 1% and at 0.02% supersaturations. At 1% supersaturation, high differences are concentrated over Paris and the near vicinity, where they reach up to 11%. However, at 0.02% supersaturation, differences are larger outside Paris over rural area. The differences over urban regions are a consequence of high concentrations of freshly emitted insoluble particles such as EC particles from traffic. In the EM simulation, these particles are hardly activated because they are hydrophobic. However, in the IM simulation, EC is always mixed with hydrophilic components, enhancing the particle activation. Over rural regions, particles are more aged and mixed than over urban regions, leading to a lower percentage of unmixed hydrophobic EC particles in the EM simulations. Hence, at high supersaturation, the difference between EM and IM simulations is lower than over urban regions and most particles are activated. At low supersaturation, the difference between EM and IM simulations is high over rural regions, because only particles with very low s_c can be activated, such as large-diameter soluble-rich particles. In the IM simulation, all particles contain both hydrophilic and hydrophobic species, with the hydrophobic components enhancing the activation of particles. However, in the EM simulations, the particles that are made exclusively of hydrophilic species do get activated.

The relative difference between IM and EM simulations is also illustrated in Figure 3.11, which shows the CCN activation percentage as well as the CCN activation relative difference at six supersaturations at the urban site (48.82° N, 2.34° E) of Figure 3.10. The relative difference changes sign at around 0.15% supersaturation. Its variations depend on the mass repartition of soluble/insoluble species over particles, which depends on the

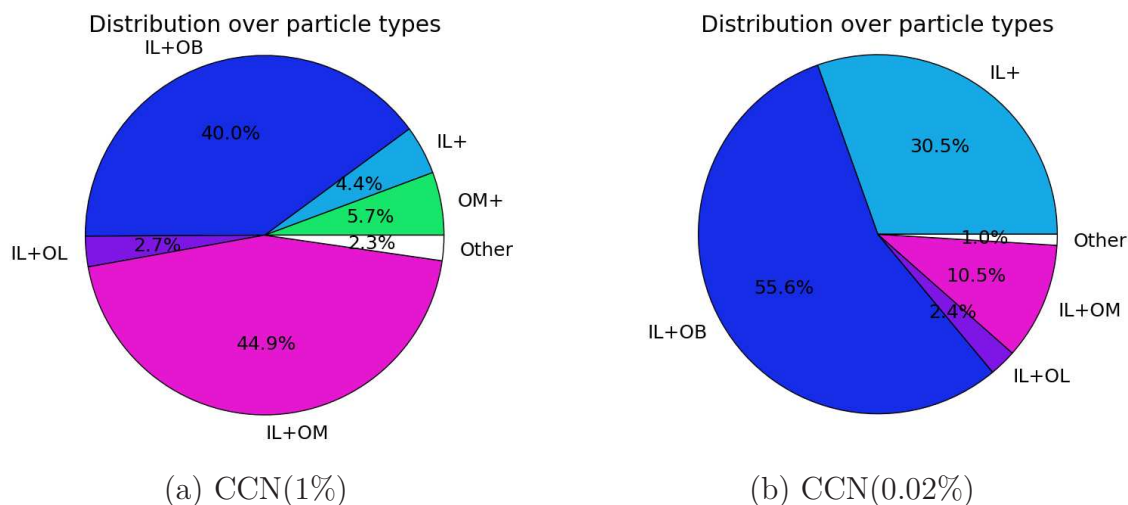


Figure 3.12: CCN contribution of each particle types under 1% and 0.02% of supersaturation.

mixing state. At low supersaturation, IM leads to lower CCN activation percentage than EM, because the hydrophobic components of IM particles inhibit activation and only the hydrophilic particles of the EM simulation may be activated. At high supersaturation, IM leads to higher CCN activation percentage than EM, because most particles are activated except for the particles that are mostly hydrophobic in the EM simulation.

3.5.3 Contribution of particle types

Figure 3.12 compares the relative contribution of the different particle types to the number of CCN activated particles at 0.02% and 1% supersaturations. Inorganic (IL+) particles are activated at lower supersaturation than organic (OM+) particles. At 0.02% supersaturation, the IL+ particles contribute to around 30.5% of the total CCN activation and the fraction of activated organic particles is negligible, while at 1% supersaturation, the IL+ contribution is only 4.4%, and almost 6% of activated particles are organic particles (OM+). This is quite reasonable, as IL+ particles are mostly made of soluble materials, thus have low s_c and can easily be activated. At higher supersaturation, a larger percentage of less soluble particles are activated. Thus the relative contribution IL+ is lower. Besides, most activated particles contain inorganic species or at least hydrophilic species, as hydrophilic species favour CCN activation. Activated OM+ particles at 1% supersaturation contain more than 20% of hydrophilic species.

The relative contribution of the different particle types to the total number concentration is presented in Figure 3.13. There are 5 particle types that mostly contribute to total number concentration: IL+OM, IL+OB, OM+, IL+, IL+OL. The comparison to Figure 3.12 shows that these 5 particle types are activated at 1% supersaturation, while only OM+ is not activated at 0.02% supersaturation. Furthermore, at 1% supersaturation, the comparison shows that the relative contribution of IL+OB and IL+OM to the number of activated particle is higher than their contribution to the total number of particles, while the contribution of IL+ to the number of activated particles is slightly lower than its contribution to the total number of particles. These differences in relative con-

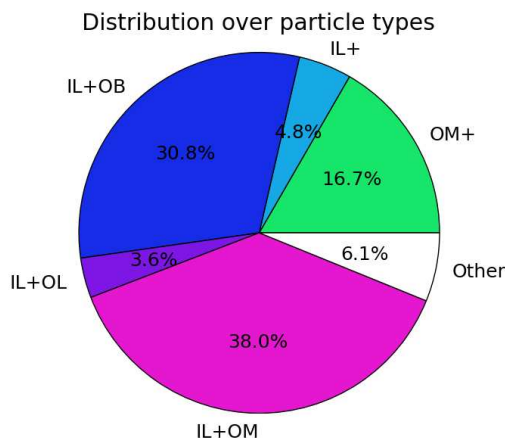


Figure 3.13: Averaged fraction of each particle type to total aerosol number concentration

tribution may not be explained by the hydrophilic properties of the species, as particles that contain hydrophobic materials (OB or OM) are less easily activated than particles that do not. These differences in relative contribution are explained by differences in the size distribution of chemical species: a great number (42.7%) of IL+ particles are concentrated in the smallest size section ($d_p < 0.0398 \mu m$), which is very difficult to be activated, whereas this percentage drops to 9.9% for IL+OB particles and to 19% for IL+OM particles.

3.6 Conclusions

The size-composition resolved aerosol model (SCRAM) coupled to the Polyphemus air-quality platform is evaluated over Greater Paris. Four simulations with different mixing-state assumption (internal mixing IM or external mixing EM) and condensation/evaporation algorithms (bulk equilibrium or dynamic) are compared. The four simulations model well the total mass of PM₁₀ and PM_{2.5} and aerosol optical depths, as assessed from comparisons to observations from the BDQA and AERONET networks.

The concentrations from IM and EM simulations are similar when bulk equilibrium is assumed for condensation/evaporation. Comparisons therefore focuses on differences from IM and EM simulations arise when condensation/evaporation is computed dynamically. Note that only the condensation/evaporation of inorganics is computed dynamically here. EM leads to higher nitrate concentration ($1.24 \mu g m^{-3}$ on average) than IM ($0.76 \mu g m^{-3}$ on average) and lower ammonium concentration ($1.23 \mu g m^{-3}$ on average) than IM ($1.33 \mu g m^{-3}$ on average). Furthermore, the differences are especially high for peak concentration. Between 3 July and 4 July, the peak concentration of nitrate for the EM simulation is twice the one for the IM simulation.

We define the unmixed EC percentage as the ratio of the EC mass of unmixed EC particles to the EC mass of all particles. At the urban site of Paris, the unmixed EC percentage does not drop to low values: it is higher than 35% with peak around 80% during rush hours when emissions are the highest.

Detailed analyses are also conducted to investigate the impact of the mixing state on

particle optical properties as well as on the cloud condensation nuclei (CCN) based on the dynamic IM and EM simulations. Using the same aerosol optical depth (AOD) computation method (core or mix), the IM simulation leads to higher AOD values and lower SSA values than the EM simulation. However, the differences between AOD computed using a core or mix method and AOD are lower than differences between AOD computed from the IM and EM simulations. For SSA, the larger differences, up to 11% between IM and EM simulations, are concentrated in the city of Paris, where a large percentage of EC is unmixed in the EM simulation, affecting the absorption and scattering properties of particles. For AOD, differences between IM and EM are rather low over the city of Paris, but they are high over some regions such as the north east and the south west of Paris. Differences are due to differences in inorganic concentrations resulting from differences in the mixing-state assumption, and leading to differences in water aerosol concentration, and AOD. For example, differences of 22% in inorganic concentrations can lead to differences as high as 80% in water concentration and 72% in AOD. Concerning CCN, at low supersaturation, IM leads to lower CCN activation percentage than EM, because the hydrophobic components of IM particles inhibit activation and only the hydrophilic particles of the EM simulation may be activated. At high supersaturation, IM leads to higher CCN activation percentage than EM, because most particles are activated except for the particles that are mostly hydrophobic in the EM simulation. Moreover, in case of high supersaturation, the difference in the spatial distribution between IM and EM simulations are more significant over urban regions. However, such distribution pattern also inverses under low supersaturation.

Although the potential of SCRAM to investigate particle mixing state has been demonstrated in this study, it is somehow limited as no mixing state observation data is available during our summer simulation period. So, the future work will focus on conducting a new simulation where particle type resolved measurement is available, such as the winter period of 2010 [Healy et al., 2012]. Besides, current simulation period is limited to only one week due to the relative high computational demand of external mixing simulation and limited computational resources. Although a comprehensive particle composition description has been used in this study, it is still possible to improve such representation. Because most of the particle mass and number are concentrated within a few particle compositions, and several compositions are hardly exist during the entire simulation. So, it is possible to optimize the computation efficiency by improving the particle class parametrization, which could reduce the total number of particle classes while conserving those particle classes with significant importance.

Chapter 4

Simulation of particle diversity and mixing state over Greater Paris: Model-to-data comparison

Résumé

Deux simulations, une avec l'hypothèse de mélange interne (MI) et une autre avec l'hypothèse de mélange externe (ME), sont effectuées entre le 15 janvier et le 11 février 2010, pendant la campagne hiver MEGAPOLI durant laquelle les compositions individuelles des particules ont été mesurées. D'abord, les simulations sont évaluées par des comparaisons des concentrations simulées d'O₃, de PM_{2.5} et de PM₁₀ avec les observations de la BDQA (Base de données de la qualité de l'air). Les statistiques montrent que les simulations donnent des résultats satisfaisants. Ensuite, les concentrations simulées des composés chimiques (concentration massique totale de chaque composé) et les concentrations des classes de particules (une classe est définie par sa taille et sa composition chimique) sont comparées avec les observations de Healy et al. [2013]. De bonnes corrélations sont trouvées entre les résultats des simulations et les mesures à la fois pour les PM₁ et pour les concentrations massiques de différents composés tels que EC (carbone élémentaire). Pour les comparaisons des concentrations des classes de particules entre la simulation et les observations, nous trouvons une assez bonne cohérence entre les résultats de simulation et les mesures pour les particules riches en EC. L'état de mélange des particules pauvre en EC est cependant un peu moins bien simulé, probablement à cause de l'algorithme de redistribution des organiques après condensation/évaporation. Ensuite, un indicateur de la diversité des particules et de l'état de mélange est calculé comme dans l'approche développée par Riemer and West [2013]. L'indicateur calculé à partir des simulations est comparé avec celui calculé à partir des mesures de Healy et al. [2012]. La valeur moyenne de l'indicateur est cohérente entre la simulation et la mesure (2,91 à partir de la simulation et 2,79 à partir des mesures). Cet indicateur représente le nombre moyen d'espèces dans chaque particule. La distribution spatiale de l'indicateur (en moyenne sur le temps de la simulation) montre que les particules sont peu mélangées en région urbaine, tandis qu'elles sont plutôt bien mélangées en région rurale. Cela indique que l'hypothèse de mélange interne traditionnellement utilisée dans les modèles de chimie transport est bien adaptée aux régions rurales, mais cette hypothèse est moins

réaliste en régions urbanisées proches des sources d'émissions.

Sommaire

4.1	Introduction	97
4.2	Model presentation	98
4.3	Simulation setup and measurement database	99
4.4	Result analysis and discussion	103
4.4.1	Bulk mass concentrations	103
4.4.2	Concentration of each particle composition	108
4.4.3	Mixing state analysis	114
4.5	Conclusion	121

4.1 Introduction

Atmospheric particles possess a large diversity of their chemical compositions, and those compositions are constantly evolving as particles mix with each other and interact with surrounding gases. The diversity of particle compositions in a population of a given size range is often referred to as the particle mixing state [Healy et al., 2014]. Although most measurements are performed for "bulk" chemical compounds, i.e. without considering the particle mixing state (e.g., aerodyne high-resolution time-of-flight aerosol mass spectrometer (HR-ToF-AMS) [DeCarlo et al., 2006], and multi-angle absorption photometer (MAAP) [Petzold and Schönlinner, 2004]), more and more field studies have focused on measuring individual particle compositions using the single particle mass spectrometers such as the aerosol time-of-flight mass spectrometer (ATOFMS). Particle mixing state may allow to assist in the identification of particle sources [Murphy et al., 2006; Ault et al., 2010; Healy et al., 2012; Dall’Osto et al., 2013], as well as to determine climate-relevant particle properties such as cloud condensation nuclei (CCN) activity, hygroscopicity, optical absorption and scattering [Mallet et al., 2004; Furutani et al., 2008; Herich et al., 2009; Crosbie et al., 2015]. Furthermore, information on the particle mixing state can be a powerful tool to assess ageing processes and the relative impact of local and regional sources of ambient particles in urban environments [Healy et al., 2013].

Aside from observations, the modelling of composition-resolved particles remains challenging. In most air-quality and climate models, for computational reasons, the particle diversity is not considered, and it is assumed that all particles within the same size section [Debry et al., 2007a] or within the same mode [Sartelet et al., 2006] have an homogeneous composition. Those models are often referred to as internal-mixing models. An external-mixing model provides additional complexity by allowing for multiple particle compositions within a given size range. Limited by complexity and computational resources, most of the developed external-mixing models are 0-D box models [Jacobson et al., 1994; Russell and Seinfeld, 1998; Jacobson, 2002a; Lu and Bowman, 2010; Dergaoui et al., 2013; Zhu et al., 2015a]. Few attempts have been made to simulate the externally-mixed particles in three dimensions, usually neglecting coagulation, and introducing simplifying assumptions. In Kleeman and Cass [2001], different particle distributions are associated

with different emission sources. However, particles are not allowed to exchange freely between different populations, and only transportation and interaction with gas phase species is simulated. In the works of Stier et al. [2005] and Bauer et al. [2008], the particle distribution is represented by mixed and unmixed modes of predefined compositions; in Oshima et al. [2009a], the compositions of particles are discretized based on the mass fraction of black carbon in the particles. Riemer et al. [2009] model externally-mixed particles using an accurate stochastic approach, which may be computationally expensive when the number of particles is high. Zhu et al. [2015a] developed a Size-Composition Resolved Aerosol Model (SCRAM), where both the size and mass fractions of chemical components of particles are discretised. For a given particle size section range, particles could have distinct chemical compositions. When discretising mass fractions, chemical components may be grouped into several aggregates to reduce the computational cost. SCRAM takes into account the processes of coagulation, condensation/evaporation and nucleation. The SCRAM model has already been integrated into the Polyphemus air quality platform [Mallet et al., 2007] and used to evaluate the Paris region from 28 June to 5 July 2009 [Zhu et al., 2015b]. This evaluation showed that SCRAM is able to give satisfactory results for both $\text{PM}_{2.5}/\text{PM}_{10}$ mass concentrations and aerosol optical depths, as assessed from comparison to observations. Furthermore, the model has the ability to analyse the particle mixing state, as well as the impact of the mixing-state assumption on particle formation and properties. However, as no observational data of single particle composition and mixing state is available for the simulation of July 2009, the model performance could not be evaluated for that period [Zhu et al., 2015b]. In this work, a simulation is conducted for January/February 2010 when the composition of individual particles was measured [Healy et al., 2014] during the winter campaign of MEGAPOLI (Megacities: emissions, urban, regional and Global Atmospheric POLLution and climate effects, and Integrated tools for assessment and mitigation). As a result, the model performance in simulating the particle mixing state is able to be evaluated in the first time through the model-to-data comparison.

After a brief presentation of the model, the simulation set-up and the measurement data of Healy et al. [2013] are presented. The simulated bulk concentrations of chemical species and the concentrations of individual particle classes are then compared to the measurements. The single particle diversity and the mixing state index are computed based on the approach developed by Riemer and West [2013], and they are compared to the measurements based analyses of Healy et al. [2014].

4.2 Model presentation

The Polair3D air quality model [Sartelet et al., 2007] of the Polyphemus air quality platform [Mallet et al., 2007] is used to simulate air quality over the Paris area. The Carbon Bond 05 model (CB05) [Yarwood et al., 2005] is used for gas-phase chemistry. The VSRM model is applied for the in-cloud process of aerosols [Fahey and Pandis, 2001]. The SCRAM model [Zhu et al., 2015b] is used to simulate the dynamics of the aerosol size distribution.

In SCRAM, the mass fraction of a given chemical component or aggregate of chemical components within each particle is discretised into sections. Compared to previous work

[Zhu et al., 2015a, b], SCRAM now allows to discretize independently the mass fraction sections for each chemical component or aggregate of chemical components. In other words, the discretization and the number of mass-fraction sections can be different for each chemical component or aggregate of chemical components. A comprehensive particle composition list is generated by selecting the possible combinations of the mass-fraction sections of each chemical component or aggregate of chemical components. A combination of mass fractions is defined as acceptable only if the sum of the lower bounds of each fraction section within the combination is lower than 100%.

Although three aerosol dynamic processes may be taken into account in SCRAM: coagulation, condensation/evaporation and the homogeneous binary nucleation of sulphate and water nucleation, nucleation is not considered here. Within SCRAM, the condensation/evaporation of inorganic aerosols is determined using ISORROPIA [Nenes et al., 1998]. It can be solved with three different approaches: a fully dynamic approach, a bulk equilibrium approach or a hybrid approach. The fully dynamic approach computes dynamically the mass transfer rate between gas and particles for each particle size and composition section. It is the most accurate method among the 3 approaches, and it is used in this study. For the secondary organic aerosol (SOA) formation, the H²O model [Couvidat et al., 2012] is used, and bulk equilibrium is always assumed for organic species due to limitations of the H²O model. After condensation/evaporation, the moving-center algorithm is used for mass-number redistribution among fixed size sections and composition sections. More details about the discretisation method, the mathematical derivation, the different condensation/evaporation approaches and model validations can be found in Zhu et al. [2015a].

Although SCRAM has the ability to simulate externally-mixed (EM) particles, it may also be used for internally-mixed (IM) particles, i.e. using the internal-mixing assumption by having only one section for each mass-fraction section (between 0 and 100%).

4.3 Simulation setup and measurement database

Simulations are conducted over Greater Paris between 15 January and 11 February 2010. The domain covers the whole Greater Paris ($[1.35^{\circ}\text{E}, 3.55^{\circ}\text{E}] \times [48.00^{\circ}\text{N}, 49.50^{\circ}\text{N}]$) with a horizontal resolution of $0.02^{\circ} \times 0.02^{\circ}$, and 9 vertical levels from the ground to 12 000 m.

In order to generate initial and boundary conditions for the simulation over Greater Paris, two nested simulations over Europe and France are conducted (see Figure 4.1 for details of the domains). Because of limitation of computational resources, those simulations are conducted with the internal-mixing assumption and the bulk-equilibrium approach for condensation/evaporation. The initial and boundary conditions for the Europe simulation are obtained from the Model for OZone And Related chemical Tracers (Mozart v2.0) [Horowitz et al., 2003], and those for the France simulation are obtained from the Europe simulation. For both the France and Europe simulations, anthropogenic emissions of gases and particles are taken from the EMEP inventory [Vestreng, 2003], and the biogenic emissions are computed using the Model of Emissions of Gases and Aerosols from Nature (MEGAN) [Guenther et al., 2006]. Meteorology is from reanalysis of the European Centre for Medium-Range Weather Forecasts (ECMWF) model.

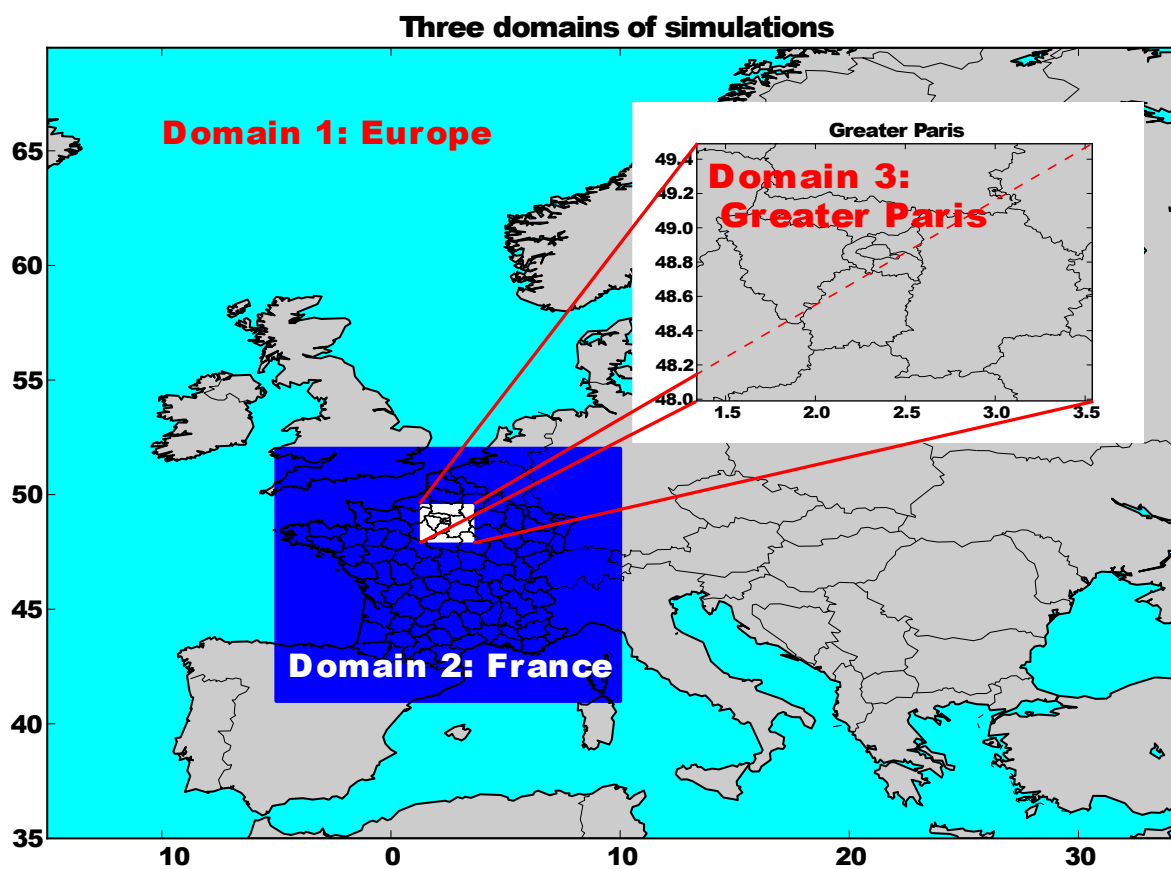


Figure 4.1: Map of three domains of simulations: Europe ($[-14.75^{\circ}\text{E}, 34.75^{\circ}\text{E}] \times [35.25^{\circ}\text{N}, 69.75^{\circ}\text{N}]$, resolution: $0.5^{\circ} \times 0.5^{\circ}$), France ($[-5.0^{\circ}\text{E}, 10.0^{\circ}\text{E}] \times [41^{\circ}\text{N}, 52^{\circ}\text{N}]$, resolution: $0.1^{\circ} \times 0.1^{\circ}$) and Greater Paris ($[1.35^{\circ}\text{E}, 3.55^{\circ}\text{E}] \times [48.00^{\circ}\text{N}, 49.50^{\circ}\text{N}]$, resolution: $0.02^{\circ} \times 0.02^{\circ}$)

For the simulations over Greater Paris, the anthropogenic emissions of gases and particles are obtained from Airparif (the Paris air quality agency, www.airparif.asso.fr) inventory for the year 2005 over Ile de France and from the EMEP inventory outside Ile de France. Following Couvidat et al. [2013], gas-phase semi-volatile organic compound (SVOC) emissions are estimated from primary organic aerosol (POA) emissions. Although a ratio $\frac{\text{Emissions}_{\text{SVOC}}}{\text{Emission}_{\text{POA}}}$ of 5 is used in Couvidat et al. [2013], this ratio is set to 2.5, as derived from measurements data from a recent traffic emission report [Charron and Aymoz, 2015]. Meteorology is simulated with the Weather Research & Forecasting (WRF) version 3.6 model [Skamarock et al., 2008] using the urban canopy model and the Corine land-use data base [Kim et al., 2013] with the YSU parametrization [Hong et al., 2006] for the planetary boundary layer. The WSM6 scheme [Hong and Lim, 2006] is used for the microphysics option of WRF, and the Kain-Fritsch convective parametrization [Kain, 2004] is used for cumulus physics.

Two simulations are conducted over Greater Paris: one with the internal-mixing (IM) assumption and one with the external-mixing (EM) assumption. The size distribution ranging from 0.01 to 10 μm is discretised into five size sections with bounds at 0.01, 0.1585, 0.4, 1.0, 2.5119 and 10 μm . As detailed in Couvidat et al. [2012], 31 particulate species are included in the simulations. In order to establish an appropriate comparison with the chemical species available from the observations, those 31 species are grouped into 5 groups in the EM simulation: Elementary Carbon (EC), Sulphate (SO_4), Nitrate (NO_3), all organics species are grouped into the Organic Aerosol group (OA), and all the other species (ammonium and sea salt) are in the group Others (OT). For the EM simulation, the mass fraction of the first group EC is discretised into three mass-fraction sections ($[0.0,0.1]$, $[0.1,0.9]$, $[0.9,1.0]$), while SO_4 , NO_3 and OA groups are discretised into two mass-fraction sections ($[0.0,0.1]$, $[0.1,1.0]$). If the mass fraction of one chemical group is located within the range $[0.1,1.0]$, then the chemical group is considered as one of the main chemical groups of the section, otherwise it is regarded as insignificant. EC is discretised with one more mass-fraction section than the other groups ($[0.9,1.0]$), to be able to distinguish freshly emitted EC particles from aged particles. The last group OT is not discretised and its mass fraction is obtained by mass conservation. A total of 17 possible particle compositions are generated, as presented in Table 4.1. The names assigned to the particle compositions are chosen depending on their main chemical groups. The water content within each particle is also computed and tracked with SCRAM, while it is excluded when computing the mass fraction of each chemical group.

The measurement data of O_3 , PM_{10} and $\text{PM}_{2.5}$ from the BDQA database ("Base de Données de la Qualité de l'Air": the French Data Basis for Air Quality that covers France) is used to evaluate the model performance. More detailed observation data is obtained during the winter MEGAPOLI (Megacities: Emissions, urban, regional and Global Atmospheric POLLution and climate effects, and Integrated tools for assessment and mitigation) campaign in 2010 [Healy et al., 2013], where chemical composition at single particle level was measured using an Aerosol Time-of-Flight Mass Spectrometer (ATOFMS) for particles within the size range 150-1067 (nm) at the urban background site of the Laboratoire d'Hygiène de la Ville de Paris (LHVP), Paris (48.75° N, 2.36° E) between 15 January and 11 February. Ten carbonaceous classes were identified from approximately 1.50 million detected spectra with the help of a K-means algorithm [Anderson

Table 4.1: 17 Externally-mixed particle compositions

Index	Composition Names	Mass fraction of each groups			
		EC	SO	NO	OA
1	OT	0-0.1	0-0.1	0-0.1	0-0.1
2	OA	0-0.1	0-0.1	0-0.1	0.1-1
3	NO	0-0.1	0-0.1	0.1-1	0-0.1
4	OA-NO	0-0.1	0-0.1	0.1-1	0.1-1
5	SO	0-0.1	0.1-1	0-0.1	0-0.1
6	OA-SO	0-0.1	0.1-1	0-0.1	0.1-1
7	SO-NO	0-0.1	0.1-1	0.1-1	0-0.1
8	OA-SO-NO	0-0.1	0.1-1	0.1-1	0.1-1
9	EC+	0.1-0.9	0-0.1	0-0.1	0-0.1
10	EC-OA	0.1-0.9	0-0.1	0-0.1	0.1-1
11	EC-NO	0.1-0.9	0-0.1	0.1-1	0-0.1
12	EC-OA-NO	0.1-0.9	0-0.1	0.1-1	0.1-1
13	EC-SO	0.1-0.9	0.1-1	0-0.1	0-0.1
14	EC-OA-SO	0.1-0.9	0.1-1	0-0.1	0.1-1
15	EC-SO-NO	0.1-0.9	0.1-1	0.1-1	0-0.1
16	EC-OA-SO-NO	0.1-0.9	0.1-1	0.1-1	0.1-1
17	EC	0.9-1	0-0.1	0-0.1	0-0.1

et al., 2005]. First, the number concentration of each ATOFMS class was calculated for each hour of the campaign, then the corresponding mass concentration of each particle class was estimated based on particle diameter and an assumed density value of 1.5 g cm^{-3} . The hourly-resolved mass fraction of each chemical species was also measured for each size sections, which helped to deduce the bulk mass concentration of each species during the measured period. Finally, the ATOFMS-derived total mass concentrations for each species were multiplied by a factor 1.24 to account for the low bias of the ATOFMS [Healy et al., 2013].

4.4 Result analysis and discussion

4.4.1 Bulk mass concentrations

Concentrations of $\text{PM}_{2.5}$, PM_{10} and O_3 from both the IM and EM simulations are first compared to the observations from the BDQA database to evaluate the model performance. Table 4.2 shows the definitions of the statistical indicators used in this study. Table 4.3 presents the statistics between both the IM and EM simulation results and the measurements during the entire simulation period (from 15 January to 11 February). Both the EM and IM simulations have good model performance, as the hourly O_3 concentration satisfies the recommended performance criteria [Russell and Dennis, 2000] ($|\text{MNGB}| \leq 15\%$ and $\text{MNGE} \leq 30\%$), and both the PM_{10} and $\text{PM}_{2.5}$ meet the model performance criterion for PM proposed by Boylan and Russell [2006] with $\text{MFE} \leq 75\%$ and $|\text{MFB}| \leq 60\%$. The statistics of $\text{PM}_{2.5}$ are even close to the model performance goal ($\text{MFE} \leq 50\%$ and $|\text{MFB}| \leq 30\%$) proposed by Boylan and Russell [2006], while PM_{10} is rather under-estimated, which is consistent with previous simulations over the same region [Couvidat et al., 2013; Wang et al., 2014; Zhu et al., 2015b]. Possible reasons for this under-estimation of coarse particles may be that re-suspension is not modelled and that boundary conditions may be under-estimated.

The concentrations of PM_{10} and $\text{PM}_{2.5}$ from the IM and EM simulations are very similar, which is consistent with the findings of the summer simulations [Zhu et al., 2015b]. However, the similarity between the PM_{10} and $\text{PM}_{2.5}$ from the IM and EM simulations may be artificial, and it may be caused by the bulk equilibrium approach used to compute the condensation/evaporation of organics. Organic mass is found to be the largest component of the total aerosol mass here. As shown in Zhu et al. [2015b] for inorganics, the mixing assumption strongly impacts concentrations of semi-volatile components when the condensation/evaporation is computed dynamically.

More detailed analysis are made for PM_1 and individual chemical components between model simulation results and observation data from Healy et al. [2013]. Because dust and sea-salt are not taken into account in the measurements of Healy et al. [2013], they are not included in the computation of simulated PM_1 concentrations for the comparison. In other words, PM_1 is computed by summing the concentrations of the first three size sections (between $0.01 \mu\text{m}$ and $1 \mu\text{m}$) and all composition sections, excluding the concentrations of dust and sea salt. The concentrations of elementary carbon (EC), sulphate (SO_4), nitrate (NO_3), ammonium (NH_4), organic aerosols (OA) in PM_1 are available in the measurements and are compared to the simulation results. The statistics are analysed between the results of both the IM and EM simulations and the measurements for

Table 4.2: Definitions of the statistics used in this work. $(o_i)_i$ and $(c_i)_i$ are the observed and the simulated concentrations at time and location i , respectively. n is the number of data

Statistic indicator	Definition
Root mean square error (RMSE)	$\sqrt{\frac{1}{n} \sum_{i=1}^n (c_i - o_i)^2}$
Correlation	$\frac{\sum_{i=1}^n (c_i - \bar{c})(o_i - \bar{o})}{\sqrt{\sum_{i=1}^n (c_i - \bar{c})^2} \sqrt{\sum_{i=1}^n (o_i - \bar{o})^2}}$
Mean normalised gross bias (MNGB)	$\frac{1}{n} \sum_{i=1}^n \frac{o_i - c_i}{c_i}$
Mean normalised gross error (MNGE)	$\frac{1}{n} \sum_{i=1}^n \frac{ o_i - c_i }{c_i}$
Normalised mean bias (NMB)	$\frac{\sum_{i=1}^n o_i - c_i}{\sum_{i=1}^n c_i}$
Normalised mean error (NME)	$\frac{\sum_{i=1}^n o_i - c_i }{\sum_{i=1}^n c_i}$
Mean fractional bias (MFB)	$\frac{1}{n} \sum_{i=1}^n \frac{c_i - o_i}{(c_i + o_i)/2}$
Mean fractional error (MFE)	$\frac{1}{n} \sum_{i=1}^n \frac{ c_i - o_i }{(c_i + o_i)/2}$

Table 4.3: Statistics between the IM and EM simulation results (from 15 January to 11 February) and the measurements of the BDQA network during the MEGAPOLI winter campaign. (Obs. stands for observation. Sim. stands for simulation. Corr. stands for correlation.)

Species	Sim.	Obs. mean $\mu\text{g m}^{-3}$	Sim. mean $\mu\text{g m}^{-3}$	RMSE $\mu\text{g m}^{-3}$	Corr. %	MNGB %	MNGE %	MFB %	MFE %
O ₃	IM	31.59	37.07	18.72	61.23	-2.78	20.44	-8.13	23.71
	EM	31.59	37.07	18.72	61.23	-2.78	20.44	-8.13	23.71
PM ₁₀	IM	30.68	19.63	22.49	38.26	-24.33	51.06	-46.64	63.34
	EM	30.68	19.44	22.65	37.86	-25.10	51.41	-47.69	64.08
PM _{2.5}	IM	24.95	21.65	19.02	39.58	19.53	66.86	-9.39	55.57
	EM	24.95	21.53	19.21	38.65	19.55	67.73	-10.08	56.28

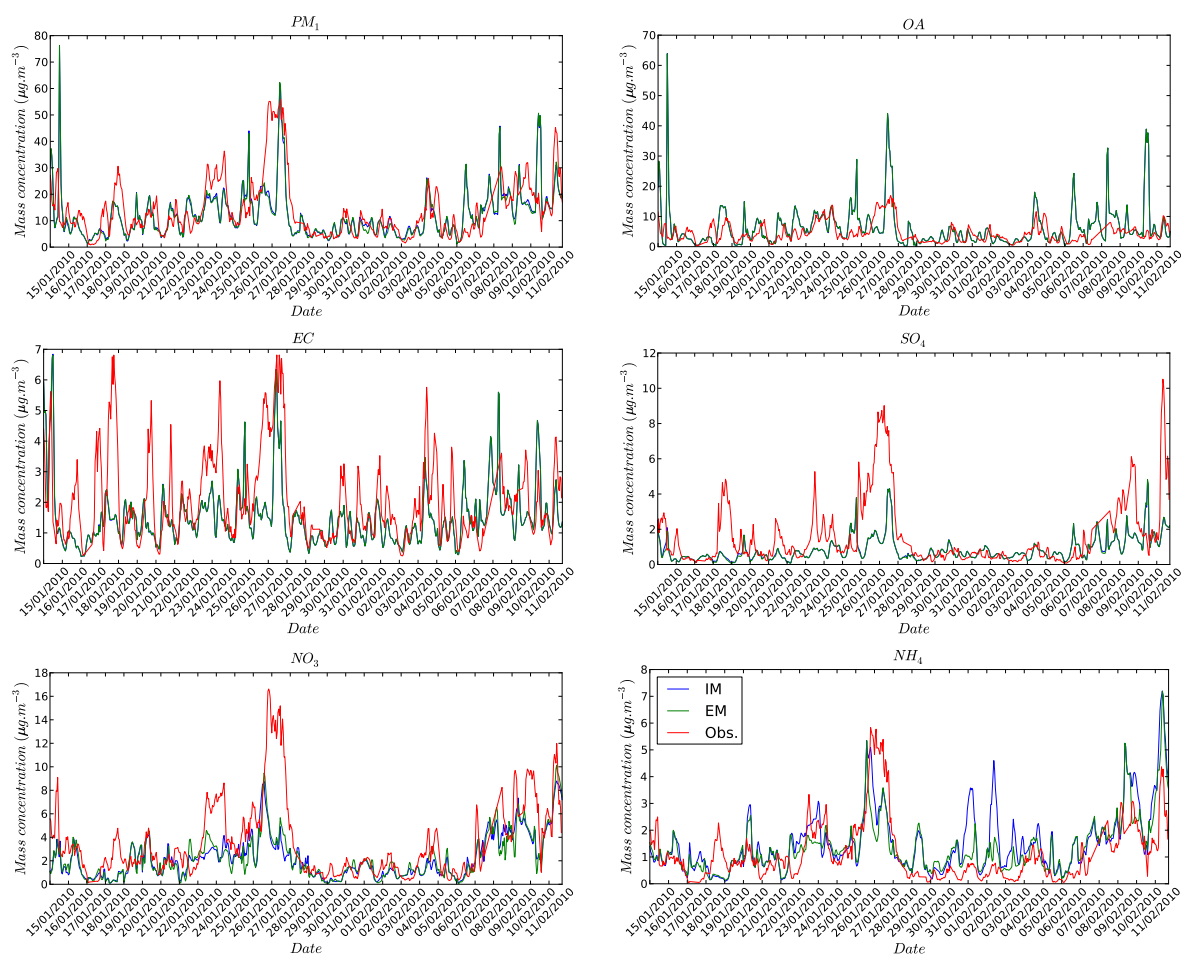


Figure 4.2: Comparisons of the IM (blue line) and the EM (green line) simulation results with ATOFMS-derived mass concentrations for PM₁, EC, OA and inorganic ions (Obs. stands for observation - red line)

Table 4.4: Statistics between the IM and EM simulation results (from 15 January to 11 February) and the measurements of [Healy et al., 2013] at LHVP site (48.75° N, 2.36° E) during the MEGAPOLI winter campaign. (Obs. stands for observation. Sim. stands for simulation. Corr. stands for correlation.)

Species	Sim.	Obs. mean	Sim. mean	RMSE	Corr.	NMB	NME	MFB	MFE
		$\mu\text{g m}^{-3}$	$\mu\text{g m}^{-3}$	$\mu\text{g m}^{-3}$	%	%	%	%	%
PM ₁	IM	14.21	12.16	9.53	59.47	-14.42	43.45	-8.83	45.84
	EM	14.21	11.99	9.62	59.06	-15.60	43.82	-10.62	46.52
EC	IM	2.08	1.46	1.42	46.82	-29.59	46.56	-26.33	49.35
	EM	2.08	1.47	1.41	46.90	-29.45	46.54	-26.16	49.30
SO ₄ ⁻	IM	1.62	0.84	1.82	54.52	-48.48	65.34	-31.36	70.14
	EM	1.62	0.83	1.83	53.55	-49.04	65.91	-33.02	71.30
NO ₃ ⁻	IM	3.59	2.20	2.85	64.79	-38.73	49.15	-39.47	61.79
	EM	3.59	2.23	2.77	67.57	-37.90	49.06	-40.67	64.49
NH ₄ ⁺	IM	1.15	1.54	1.10	61.47	33.42	70.29	38.98	69.07
	EM	1.15	1.34	0.95	61.88	15.74	59.62	32.64	65.12
OA	IM	4.65	6.20	6.41	38.72	33.19	77.86	10.28	60.59
	EM	4.65	6.21	6.42	38.79	33.44	77.99	10.42	60.64

the entire simulation period, and they are presented in Table 4.4. Meanwhile, the time evolution of the different chemical components are plotted in Figure 4.2.

Over the entire simulation period, Table 4.4 and Figure 4.2 show that both the IM and EM results compare well to observations. The statistics of comparisons of PM_1 and EC meet both the model performance goal and criterion proposed by Boylan and Russell [2006], while the statistics of the other components meet the model performance criterion. EC, SO_4 and NO_3 are moderately under-estimated, while OA and NH_4 are moderately over-estimated. SO_4 tends to be more under-estimated during the first two weeks because of the under-estimation of some peaks, as can be seen in Figure 4.2. On 18 January, a peak of SO_4 was caused by a strong fog event according to Healy et al. [2013]. The model is not able to reproduce this peak, as fog events may not be properly modelled in our simulations, where cloud chemistry occurs depending on the liquid water content of the grid cell. This also explains the under-estimation of the peak concentrations of NO_3 and NH_4 during the same period. The under-estimation of sulfate may also be linked to the formation of organo-sulfate, as Healy et al. [2013] found some internally-mixed organics and sulfate during that fog event. Another peak of SO_4 occurs between 25 and 28 January, where highly polluted continental air masses, which most likely originated from the north-western and eastern Europe, are transported over Greater Paris [Healy et al., 2013]. The under-estimation of this peak may due to the uncertainties in the larger-scale simulations (France and Europe), leading to the under-estimation of the amount of sulphate transported into Greater Paris through boundary conditions. Such under-estimation of sulphate has been spotted in previous simulations over Europe during the winter period of 2001 [Sartelet et al., 2007]. It may originate from uncertainties in sulphur aqueous chemistry. As emphasized by Bessagnet et al. [2004], sulphur aqueous chemistry, which is predominant in winter, is very difficult to simulate, because it is very sensitive to temperature and pH. Note that during that peak, EC is relatively well modelled, while OA is over-estimated. There is no peak of SO_4 during the period between 28 January and 7 February, which is a local-emission dominated period and is well modelled.

As for PM_{10} and $PM_{2.5}$, the differences in PM_1 concentrations between the IM and EM simulations are not significant, although noticeable differences occur in the NO_3 and NH_4 peaks, as shown in the time evolution curves of Figure 4.2. As expected, both the IM and EM simulations lead to similar concentrations of non-volatile components (EC, SO_4) and also of OA (because of the bulk-equilibrium assumption made when computing condensation/evaporation of organics). Because EC, SO_4 and OA represent more than 71% of the PM_1 concentration, the variations of the PM_1 concentration with the mixing-state hypothesis are limited. For volatile inorganics (NO_3 and NH_4), the EM assumption results in higher NO_3 concentration and lower NH_4 , as noted in the summer simulations [Zhu et al., 2015b]. Besides, NH_4 peaks are found significantly reduced between 30 January to 3 February with EM results (see Figure 4.2), which is more consistent with observations.

Figure 4.3 represents the size distribution of mass concentration and mass fraction for each chemical species. Compared to Fig. 4. of Healy et al. [2013], a similar distribution was found for EC with top concentration at low diameters (< 200 nm), while for secondary inorganic components such as NO_3 , SO_4 and NH_4 , larger mass fractions are found at higher diameters (> 400 nm) as indicated by the observation. However, different from the measurements, most of the OA mass was found at smallest size sections, which is

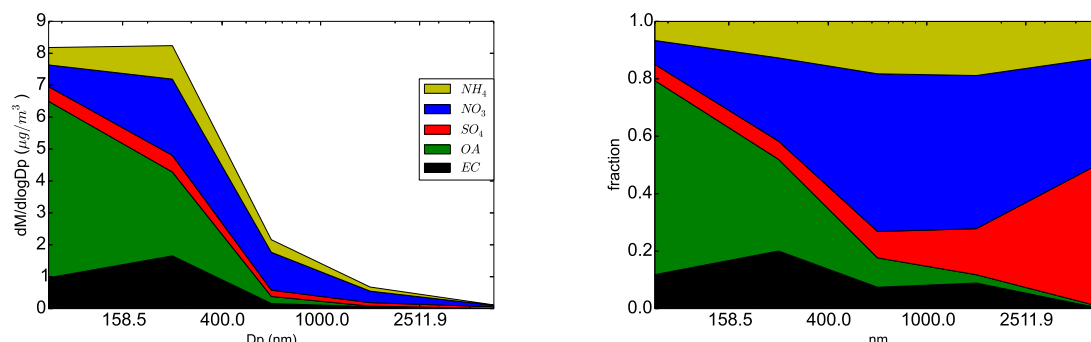


Figure 4.3: Mass-size distribution (left, stacked) and size-resolved average mass fractions (right, stacked) for each chemical species from external mixing simulation.

due to the bulk-equilibrium approached used for organic species and the redistribution method used to redistribute newly condensed organic mass after each equilibrium which will be addressed later.

4.4.2 Concentration of each particle composition

In the EM simulation, 17 particle classes are discretised based on the combinations of the mass-fraction sections of the different chemical components (or groups of chemical components), as defined in Table 4.1. The chemical group OT contains NH₄, dust and sea salt. However, as dust and sea salt are not included in the measurements of [Healy et al., 2013], they are not considered when computing particle total mass, and the composition of each particle class is therefore recomputed after the simulation. In the updated particle classes, the only component considered in the group OT is NH₄. Table 4.5 shows the average mass fraction of each chemical component at the site of LHVP for PM₁ particles, as well as the mass fraction of each particle class within the PM₁ concentration. It is clear that most of the particle mass is concentrated in a few particle classes. OA dominant particles represent more than half of the total particle mass (60.09%), while the rest of the particle mass concentrates in the particle classes OA-NO (19.79%), EC-OA (13.13%), EC (2.90%), OA-SO (1.27%) and EC-OA-NO (1.01%).

To facilitate the comparisons to measurements, the particle classes that have low mass concentrations compared to the total particle mass (lower than 0.1 %), are merged together or regrouped with particle classes of larger mass fractions. Table 4.6 shows the mass ratio of the class to the total particle mass for each of the 8 particle classes remaining after merging, as well as the mass fraction of each chemical group within each particle class. The merging does not affect the classes OA and EC-OA, while the classes EC and EC+ are merged into EC; NO and OA-NO are merged into OA-NO; SO and OA-SO are merged into OA-SO; EC-OA and EC-NO are merged into EC-OA-NO; SO-NO and OA-SO-NO are merged into OA-SO-NO; EC-OA-SO, EC-SO, EC-OA-SO, EC-SO-NO and EC-OA-SO-NO are merged into EC-OA-SO. Particles are also classified depending on their EC mass fraction: the EC-rich particle types include particle classes with high EC mass fractions (EC, EC-OA, EC-OA-NO, EC-OA-SO). In contrast, the other particle classes (OA, OA-NO, OA-SO, OA-SO-NO) are considered as EC-poor particles, as their

Table 4.5: Mass ratio of each particle class to the total mass, and the mass fraction of each chemical group within each particle class

Mass ratio %	Particle class	Mass fraction of each groups				
		EC	SO ₄	NO ₃	OA	NH ₄
<0.01	OT	0.09	0.09	<0.01	0.08	0.74
60.09	OA	<0.01	0.03	0.04	0.90	0.03
<0.01	NO	0.03	0.02	0.68	0.08	0.19
19.79	OA-NO	0.02	0.05	0.19	0.65	0.09
0.01	SO	0.07	0.31	<0.01	0.08	0.54
1.27	OA-SO	0.02	0.13	0.03	0.74	0.09
<0.01	SO-NO	0.03	0.27	0.39	0.07	0.24
0.78	OA-SO-NO	0.03	0.12	0.20	0.53	0.12
0.71	EC+	0.89	0.01	0.01	0.09	<0.01
13.13	EC-OA	0.33	0.03	0.02	0.60	0.02
0.08	EC-NO	0.61	0.01	0.29	0.06	0.03
1.01	EC-OA-NO	0.32	0.03	0.18	0.43	0.04
<0.01	EC-SO	0.46	0.34	0.01	0.05	0.14
0.19	EC-OA-SO	0.14	0.15	0.03	0.54	0.14
<0.01	EC-SO-NO	0.21	0.23	0.25	0.09	0.22
0.02	EC-OA-SO-NO	0.19	0.15	0.18	0.31	0.17
2.90	EC	0.93	<0.01	<0.01	0.06	<0.01

EC mass fraction is less than 0.1.

To obtain a comparable classification of the particle classes in the simulations and in the observations, merging of some of the observed particle classes is also done. Table 4.7 shows the association between ATOFMS particle classes from the measurements and the merged particle classes from the simulations, as well as the mass fractions of each chemical component within each particle type from the measurements. In the study of [Healy et al., 2013], Potassium (K) is used to identify the biomass burning origin of the particles. Since K is not included in the current version of SCRAM and its mass fraction is very small, the particle class K-OA-NO_x from the measurements is merged with the OA-NO_x class, and it is compared to the OA-NO class of the simulation. The classes from the measurements are assigned to classes of the simulation depending on the mass fraction of the chemical components of the class. For example, the class OA-TMA from the measurements, which links organics to trimethylamine (TMA), is merged in the OA-SO-NO class of the simulation, because it contains OA (45%) but also 12% of SO₄ and 17% of NO₃. Actually, there is no particle class that can be truly considered as unmixed from the measurements: K-OA only contains 52% of OA mass but also 21% of NO₃; K-EC contains 52% of EC mass, but also 24% of OA. However, in the simulation, particles within the EC class (2.90% of the total aerosol mass) is considered as unmixed (other chemical components contribute each to less than 10% of the particle mass), as well as particles within the OA class which consist of 60.09% of the total aerosol mass. This high percentage of unmixed OA is a consequence of the algorithm used for condensation/evaporation of organics in SCRAM with the bulk equilibrium assumption. This algorithm only gives the total amount of mass condense/evaporate in each time step regardless the particle size and their Kelvin effect. Then the total amount of condense/evaporate mass is redistribute back to each section j based on a weight factor W_i^j defined by following equation:

$$W_i^j = \frac{N_j d_p^j f(K_n, \alpha_i)}{\sum_{k=1}^{N_s} N_k d_p^k f(K_n, \alpha_i)} \quad (4.1)$$

where N_j is the number concentration of section j , d_p^k is the the particle wet diameter of section j , and $f(K_n, \alpha_i)$ describes the non-continuous effects [Dahneke, 1983] based on Knudsen number $K_n = \frac{2\lambda}{d_p}$ (with λ the air mean free path), and accommodation coefficient $\alpha_i = 0.5$. $d_p^j f(K_n, \alpha_i)$ represents the condensation/evaporation kernel of single particle in section j , so the numerator represents the total condensation/evaporation kernel of all particles within section j while the denominator represents the total condensation/evaporation kernel of particles from all sections. Generally, larger particles will have higher $d_p^j f(K_n, \alpha_i)$ values but they also will have much smaller number concentrations. What have been found from the simulation is that sections with smaller diameter dominate the weight factor due to their high number concentrations, as a result, most of the newly formed OA is condensed into the smallest sections. However, in reality, the condensation on tiny particles will be limited due to strong Kelvin effect, and more OA should be condensed on larger particles. In the other side, the condensation/evaporation of inorganic species are computed dynamically, taking into account both condensation/evaporation potential and Kelvin effect, which makes them tend to condense on relatively larger particles. As a combination of both effects, most of the OA is condensed on the smallest sections which are not favourite for inorganic condensation. This may explain why most

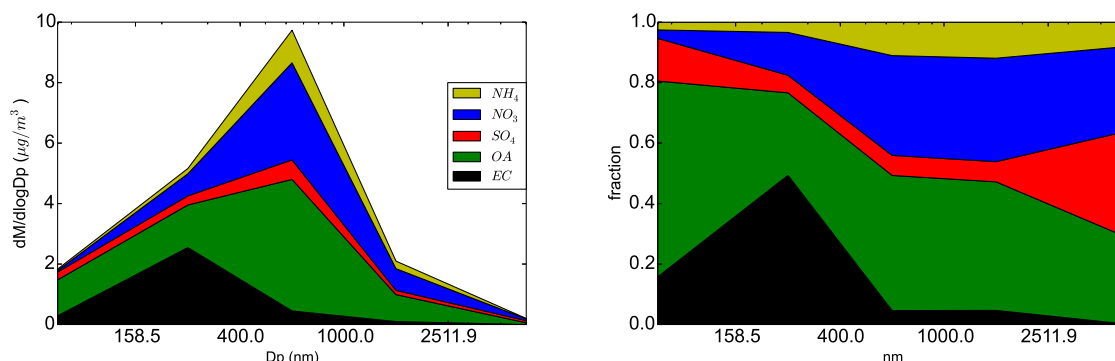


Figure 4.4: Mass-size distribution (left, stacked) and size-resolved average mass fractions (right, stacked) for each chemical species from inter mixing simulation using bulk equilibrium approach with updated redistribution method.

OA is not well mixed. To estimate the influence of the weighting factors used for redistribution, an attempt has been conducted to take into account the Kelvin effect during the redistribution process after the bulk-equilibrium condensation/evaporation process, with an updated weighting factor:

$$W_i^j = \frac{N_j d_p^j f(K_n, \alpha_i) (1/(K_e(d_p) - 1))}{\sum_{k=1}^{N_s} N_k d_p^k f(K_n, \alpha_i) (1/(K_e(d_p) - 1))} \quad (4.2)$$

where $K_e(d_p)$ represents the Kelvin effect for a particle of diameter d_p , ($K_e(d_p)$ is close to 1 for large particles and, for small particles, it become larger as the particle diameters become smaller). A quick test run with the bulk-equilibrium approach for both organics and inorganic shows a much reasonable size distribution for OA, as presented in Figure 4.4. Much less OA is concentrated in the smallest sections, and more OA is concentrated between 400 nm and 1000 nm, which is more consistent with the observation of Healy et al. [2013]. This suggests that the redistribution weighting factor defined in equation (4.2) is better suited for redistribution than the previously used factors, which did not take into account the Kelvin effect.

The mixing state of EC is well reproduced in the simulation. By comparing Table 4.6 and Table 4.7, a relatively good consistency is found for the mass ratio of EC-rich and EC-poor particles between simulation results and measurements. The simulation results estimate 18.04% of EC-rich particles and 81.96% EC-poor particles, which is similar to the ratio from the measurements: 16.8% EC-rich particles and 83.2% EC-poor particles. Furthermore, 10.3% of EC particles are found to be mixed with OA (EC-OA class) in the measurements against 13.13% in the simulation. The percentage of EC-OA-NO particles is under-estimated in the simulation (1.09%) compared to the measurements (3.8%), as well as the percentage of EC-OA-SO particles (0.21% in the simulation compared to 2.7% in the measurements). In the measurements, EC-OA-SO particles have the highest concentrations during the fog event, indicating that the under-estimation of EC-OA-SO particles in the simulation is probably linked to the fog event when sulphate concentrations are strongly under-estimated in the simulation. Besides, a large difference exist in simulated mass fraction of NO₃ and OA for EC-poor group

Table 4.6: Mass ratio of particle class to the total mass, and the mass fraction of each chemical group within each particle class

Particle class	Mass ratio %	Mean mass $\mu\text{g m}^{-3}$	Mass fraction of each group				
			EC	SO ₄	NO ₃	OA	NH ₄
OA	60.09	7.21	<0.01	0.03	0.04	0.90	0.03
OA-NO	19.79	2.37	0.02	0.05	0.19	0.65	0.09
OA-SO	1.29	0.15	0.02	0.13	0.03	0.73	0.09
OA-SO-NO	0.78	0.09	0.03	0.12	0.20	0.53	0.12
EC	3.61	0.43	0.92	0.01	<0.01	0.06	<0.01
EC-OA	13.13	1.57	0.33	0.03	0.02	0.60	0.02
EC-OA-NO	1.09	0.13	0.35	0.02	0.19	0.40	0.04
EC-OA-SO	0.21	0.03	0.15	0.16	0.04	0.51	0.14

when compared to the observation. OA mass fraction is largely over estimated (sim. 0.83 vs obs. 0.36) due to the overestimation of bulk OA concentration, while the NO₃ is largely underestimated (sim. 0.08 vs obs. 0.32) due to most of the EC-poor particles are concentrated in the smallest size section, where the condensation of NO₃ is largely limited by the Kelvin effect.

As for the total EC, the mixing state of EC-rich particles is relatively well simulated based on the mass ratio between EC (2.90%) and all EC rich particles (18.04%) from Table 4.8, as most particles are found to be mixed with other species (84%) which is close to the measurements, where all EC particles are found mixed with other species. Besides, the average mass fraction of EC is around (0.45) for all EC-rich particles in the simulation based on the mass fraction of EC in each particle class and their mass ratio from Table 4.6, which is close to the one from the measurements (0.48) computed based on the same method from Table 4.7. This indicates that the average degree of mixing of EC-rich particles is similar between simulation and measurements. However, the mixing state of EC-poor particles is not as well simulated as the mixing state of EC-rich particles. Most of the EC-poor particles are nearly unmixed (73%) in the simulation, while all of the particles are found to be well mixed (with OA mass fraction between 0.27 and 0.52) from the measurements. Most of the mass fraction of EC-poor particles are OA dominated, as indicated by the high value (0.83) of the OA mass fraction for the EC-poor particles from the simulation. These EC-poor particles tend to have low diameters (92% below 0.4 μm). The condensation/evaporation of organics is done using the bulk-equilibrium approach, which redistributed the total condensed OA mass onto particles depending on the combination of their number concentration and their condensation kernel as explained in former paragraph. In order to improve the mixing result, the redistribution of the OA mass should be improved to decrease the mass of organics in the bins of low diameters.

Table 4.9 presents the statistics for EC-rich and EC-poor particles where a relatively good correlation can be found for both EC-rich and EC-poor particles (43.11% and 60.50%

Table 4.7: Mass fractions of each chemical group determined for each ATOFMS class [Healy et al., 2013], and their corresponding SCRAM class

Class SCRAM	Class ATOFMS	Mass ratio %	Mean mass $\mu\text{g m}^{-3}$	Mass fraction of each group				
				EC	SO ₄	NO ₃	OA	NH ₄
OA-NO	K-OA	8.80	1.50	0.14	0.09	0.21	0.52	0.07
	K-OA-NO _x	28.73	4.91	0.06	0.07	0.52	0.27	0.07
	OA-NO _x	13.99	2.39	0.07	0.09	0.27	0.40	0.17
OA-SO	OA-SO _x	8.92	1.52	0.08	0.31	0.10	0.40	0.11
OA-SO-NO	K-OA-SO _x	19.68	3.36	0.05	0.23	0.22	0.36	0.13
	OA-TMA	3.10	0.53	0.04	0.12	0.17	0.45	0.21
EC-OA	EC-OA	8.27	1.41	0.62	0.06	0.02	0.30	0.01
	K-EC	2.00	0.34	0.57	0.04	0.08	0.24	0.06
EC-OA-NO	EC-OA-NO _x	3.83	0.65	0.32	0.06	0.23	0.33	0.06
EC-OA-SO	EC-OA-SO _x	2.70	0.46	0.21	0.33	0.05	0.21	0.04

Table 4.8: Mass fractions of each chemical group for EC-rich and EC-poor particles from both observation (Obs.) and simulation (Sim.)

Cases	Particle class	Mass ratio %	Mass fraction of each group				
			EC	SO ₄	NO ₃	OA	NH ₄
Obs.	EC-rich	16.8	0.48	0.10	0.08	0.31	0.03
	EC-poor	83.2	0.07	0.14	0.32	0.36	0.11
Sim.	EC-rich	18.04	0.45	0.02	0.03	0.48	0.02
	EC-poor	81.96	0.01	0.03	0.08	0.83	0.05

Table 4.9: Statistics of EC-rich and EC-poor particles between simulation results (15 to 28 January) and the measurements of [Healy et al., 2013] at LHVP site (48.75° N, 2.36° E). (Obs. stands for observation. Sim. stands for simulation. Corr. stands for correlation.)

Particle class	Obs. mean $\mu\text{g m}^{-3}$	Sim. mean $\mu\text{g m}^{-3}$	RMSE $\mu\text{g m}^{-3}$	Corr. %	NMB %	NME %	MFB %	MFE %
EC rich	4.77	2.14	3.71	43.11	-55.13	63.11	-83.68	89.96
EC poor	11.82	9.85	8.46	60.50	-16.68	45.56	-7.61	48.98

respectively). The statistics of EC-poor particles even satisfy the model performance goal of Boylan and Russell [2006] for PM simulation. The statistics of EC-rich particles are not as good as those of EC-poor particles, because the particle mass is under-estimated due to the underestimation of EC, NO₃ and SO₄ (EC-rich particles do not only contains EC mass, but also the mass of the other species mixed with EC). However, this table shows that the SCRAM model can offer a reasonable performance to simulate the concentrations of EC-rich and EC-poor particles.

4.4.3 Mixing state analysis

Healy et al. [2014] compute a quantitative mixing-state index (χ) of measured particles based on the information-theoretic entropy approach proposed by Riemer and West [2013]. The same method is used in this study to derive the mixing-state index of simulated particles. The detailed description of this method can be found in Riemer and West [2013]. For a population of N particle compositions ($N=17$ in this study) and A distinct chemical components (or species, $A=5$ in this study), the mass of species a in particle i is denoted as μ_i^a for $i = 1, \dots, N$ and $a=1, \dots, A$; the total mass of particle i is μ_i ; the total mass of species a in the total particle population is μ^a , and the total mass of the entire population is μ . These masses are computed as follows:

$$\mu_i = \sum_{a=1}^A \mu_i^a \quad \mu^a = \sum_{i=1}^N \mu_i^a \quad \mu = \sum_{i=1}^N \mu_i \quad (4.3)$$

The mass fraction of species a in particle i (p_i^a), the mass fraction of particle i in the population (p_i), and the mass fraction of species a in the population (p^a) can be calculated as follows:

$$p_i^a = \frac{\mu_i^a}{\mu_i} \quad p_i = \frac{\mu_i}{\mu} \quad p^a = \frac{\mu^a}{\mu} \quad (4.4)$$

Those basic information can be computed either for particles within each size section or for particles merged from several size sections. In this study, for comparison to measurements, which were performed for PM₁, the analysis is done for particles from the first three size sections (10 nm -1000 nm).

The information-theoretic Shannon entropy is a measure of the uncertainty associated with a random variable. According to Riemer and West [2013], the Shannon entropy associated with each single particle (H_i) can be computed based on the mass fraction of each species within that particle:

$$H_i = \sum_{a=1}^A -p_i^a \ln p_i^a \quad (4.5)$$

While the average per-particle Shannon entropy (H_α) is given by:

$$H_\alpha = \sum_{i=1}^N -p_i H_i \quad (4.6)$$

Finally, the Shannon entropy of the entire bulk population (H_γ) equals to:

$$H_\gamma = \sum_{a=1}^A -p^a \ln p^a \quad (4.7)$$

Based on those Shannon entropies, their corresponding diversity values can be derived:

$$D_i = e^{H_i} \quad D_\alpha = e^{H_\alpha} \quad D_\gamma = e^{H_\gamma} \quad (4.8)$$

where D_i is the particle diversity, or the effective number of species in particle i , D_α is the average single particle diversity, and D_γ is the bulk population diversity.

Finally, the mixing state index χ can be derived by following equation:

$$\chi = \frac{D_\alpha - 1}{D_\gamma - 1} \quad (4.9)$$

To summarize, D_i represents the number of chemical components in a particle, D_α represents the average value of D_i over the entire particle population, and D_γ shows the bulk population diversity which is consistent under both IM and EM assumptions. Eventually, χ represents the degree of similarity between an arbitrary mixing case and a pure internal mixture. As a result, $\chi=0\%$ for a pure external mixture, because $D_i = D_\alpha = 1$, while $\chi=100\%$ for a pure internal mixture as $D_\alpha = D_\gamma$.

The single particle diversity (D_i) is computed from the simulation results and compared to the measurements at the LHVP site. Most of the simulated particles (64.5%) are within the D_i range of 1.8 to 3.0, which is very close to the measurements of Healy et al. [2014], where the D_i value of the majority of particles is also in range of 1.8 and 3.0 (about 71%). As most of particle numbers are concentrated in the smallest size sections, the D_i values are normalised by the number of particles in each size section in order to get a better representation of the variation of D_i with the particle size. Figure 4.5 shows the dependence of the time-averaged number concentrations on diversity and particle diameters, as well as the dependence of time-averaged particle composition on particle diameter. This figure is to be compared to Figure 3 of Healy et al. [2014]. As noted by Healy et al. [2014], smaller particles have higher mass fractions of EC and OA, while larger particles have higher inorganic mass fractions. Although the particle number concentrations tend to be under-estimated in the simulation, high number concentrations are observed at low diameters (below 200 nm) for low diversity (2 in the measurements and between 1.8 and 3 in the simulation) and at high diameters for high diversity (4 in the measurements and between 3.4 and 4.2 in the simulation). In agreement with the measurements, at low diameters, most of the particles are composed of 2 or 3 species, mostly OA and EC. At high diameters, particles are composed of inorganics (80% in the simulation and 60% in the measurements). As the particles diameter growth, the mass fraction of inorganics grows as in the measurements, indicating the condensation/evaporation of inorganic species is correctly modelled. However, the OA mass is under-estimated at high diameters but over-estimated at low diameters, indicating as noted before that the redistribution of OA after condensation/evaporation needs to be improved or to be computed dynamically.

As in the measurements, the mass fraction of EC decreases from the section with diameters between 158.6 nm and 400 nm to a value lower than 10% at high diameters. The variation of EC with particle diameters is largely linked to the size distribution used in the emissions: 54% was emitted in the section [10-158.5 nm], 42% in the section [158.5-400 nm] and 3% in the section [400-1000 nm]. Although the mass fraction of EC increases to about 52% in the measurements, it stays below 30% in the simulation, because of the over-estimation of OA at low diameters and because of the assumed size-distribution of emissions.

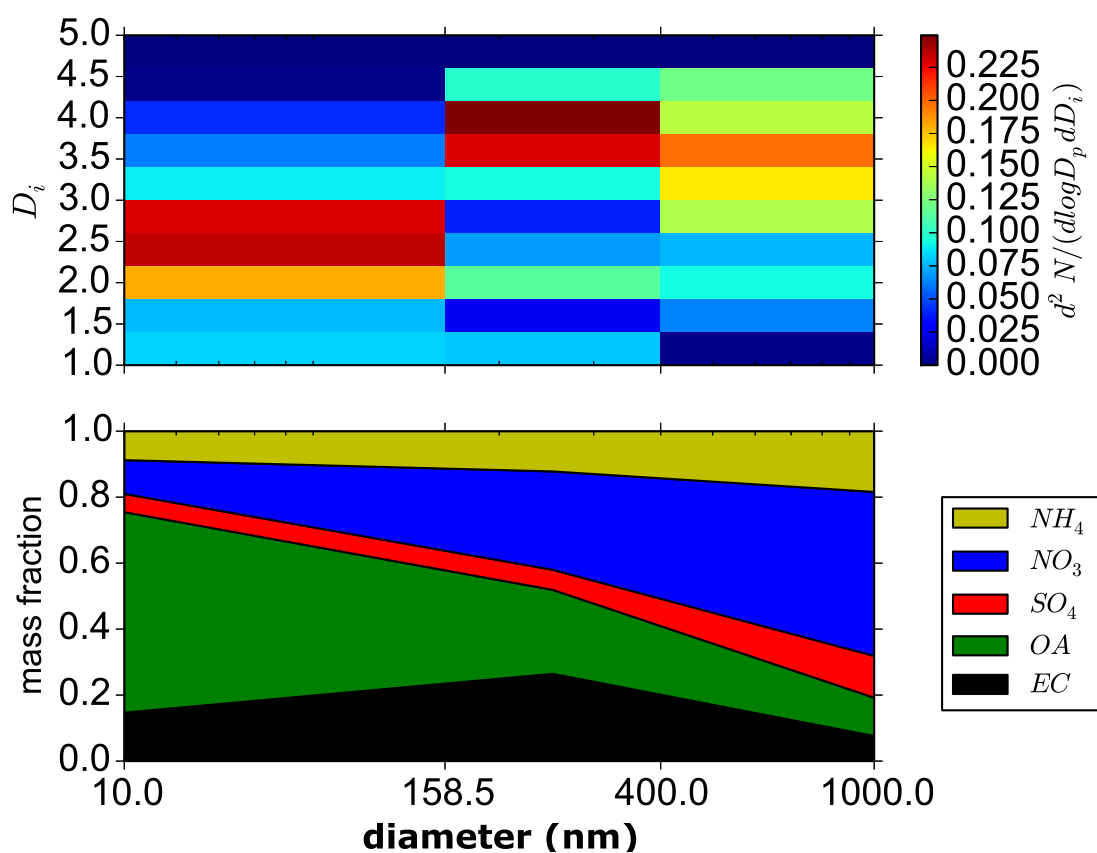


Figure 4.5: Dependence of the time-averaged number concentration on single particle diversity (diversity normalised by the number of particles in each section) and particle diameter (upper panel), and dependence of time-averaged particle composition on particle diameter (lower panel).

The average single particle diversity (D_α) and the species diversity of the bulk population (D_γ) are also derived from the simulation results. Unlike D_i which represents the characteristic of a single particle, D_α and D_γ describe the overall attribute of the entire particle population. The mixing state index can potentially range from 0% (fully externally mixed) to 100% (fully internally mixed). The averaged value of D_α from the simulation (2.91) is close to the one from the measurements (2.79), while that averaged value of D_γ tends to be under-estimated (3.76 from the simulation and 4.04 from the measurements), because of the bulk over-estimation of OA and of the bulk under-estimation of SO₄. As a result, the mixing state index χ is slightly over-estimated (69% in the simulation and 59% in the measurements), although the average single particle diversity is well represented. These low-values of the mixing-state index indicate that the particle population at LHVP is not internally mixed.

The relationship between D_α , D_γ and χ at the LHVP site is displayed in Figure 4.6, to be compared with Figure 5 of Healy et al. [2014]. The values of the mixing-state index range from 23% to 90%, with a mean value of 69%. This result is generally consistent with the measurements of Healy et al. [2014], where the mixing-state index is found to vary between 37% and 72%, with a mean value of 59%. Another phenomenon observed from the measurements, and also apparent in Figure 4.6 is that the average single particle diversity (D_α) never goes above 4 (3.5 in the measurements), even when the the bulk population diversity (D_α) approaches the maximum value of 5. This indicates that there exists a variety of different chemical mixing states for particles of the same size.

The diurnal variations of D_α , D_γ and χ are computed from both simulation and observation results, and their mean value upon time of day is shown in Figure 4.7, as well as the corresponding variation of the mass fraction of each chemical components. The averaged value of D_α from the simulation (2.91) are very close to the one from the measurement (2.79), as well as their curves. However, D_γ is relatively underestimated from the simulation due to the overestimation of OA and underestimation of SO₄. As a result, the mixing state index χ is overestimated. A decrease of both D_α and χ can be observed between 5:00-8:00, due to the increase of traffic emissions which introduce large amount of particles with high EC mass fractions and low D_i value. However, D_γ does not increase during this period as suggested by the measurement because the growth of the mass fraction of EC is not able to compensate the rapid decrease of the mass fraction of NO₃, and the mass fraction of OA also increased during that period. The χ quickly increased between 8:00-14:00 due to the combining effect of growing D_α and decreasing D_γ . The slowly increase of D_α is due to the decrease of traffic emission and ageing of existing particles. While the decreasing of D_γ is largely caused by the increase of OA fraction and decrease of of EC and inorganic fractions. χ drop again between 14:00-20:00 due to the increase of D_γ as a result of slowly increasing EC mass fraction. A rapid increase of D_α can be observed between 20:00-22:00 as a result of enhanced ammonium nitrate during the night time which is reflected by the increase of inorganic mass fraction during that period as well as an increase of D_γ .

The previous discussion is based on the measurements and simulation results at the LHVP site. Because our modelling study provides comprehensive data for the study of the spatial distribution of particle properties, Figure 4.8 presents the spatial distribution of D_α , D_γ and χ over the entire simulated domain, averaged over the simulation period. The values of D_α are lower close to center Paris and traffic roads and higher in rural

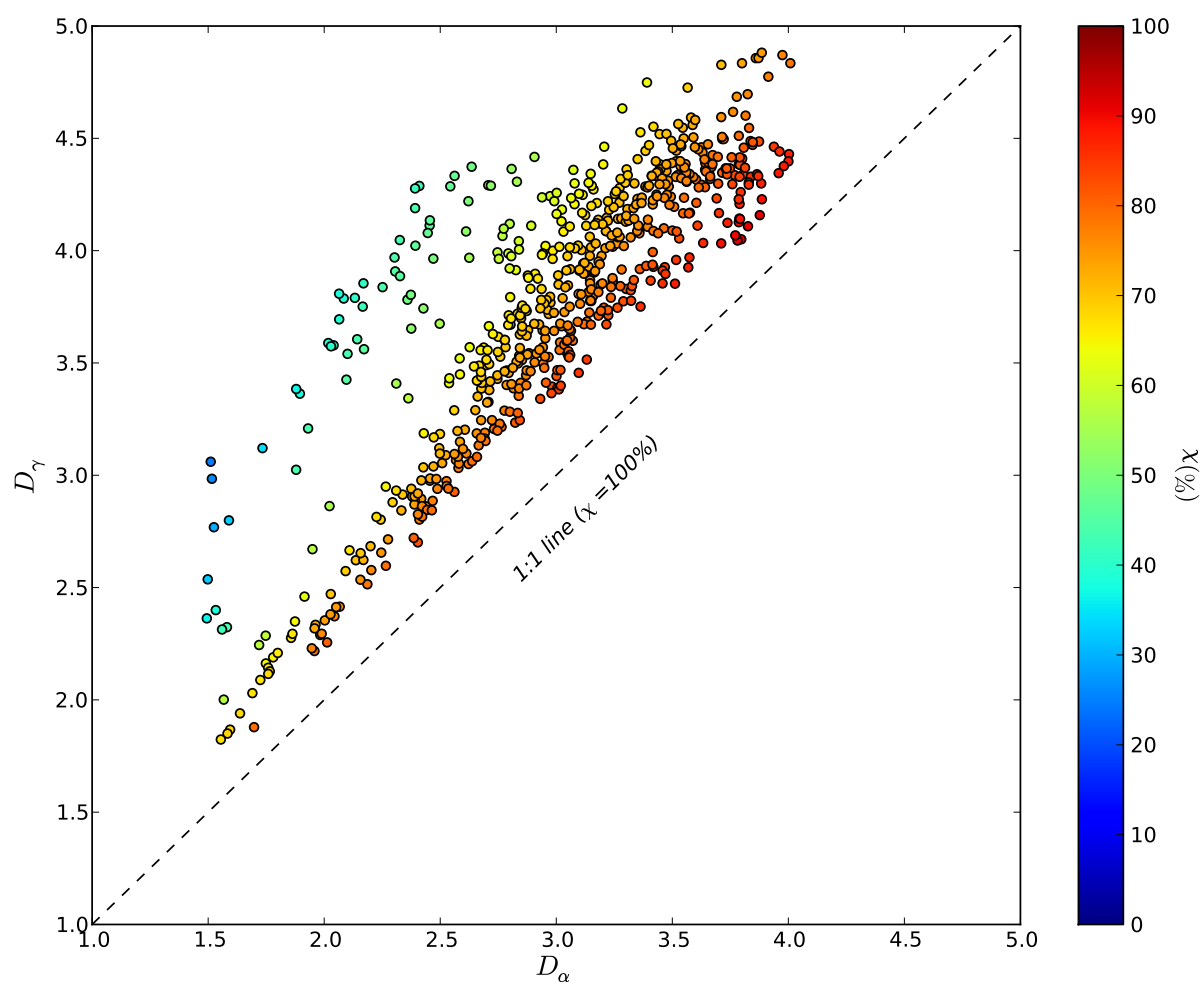


Figure 4.6: Scattering plot of the hourly mixing-state index (χ) as a function of average particle diversity (D_α) and average bulk population diversity (D_γ).

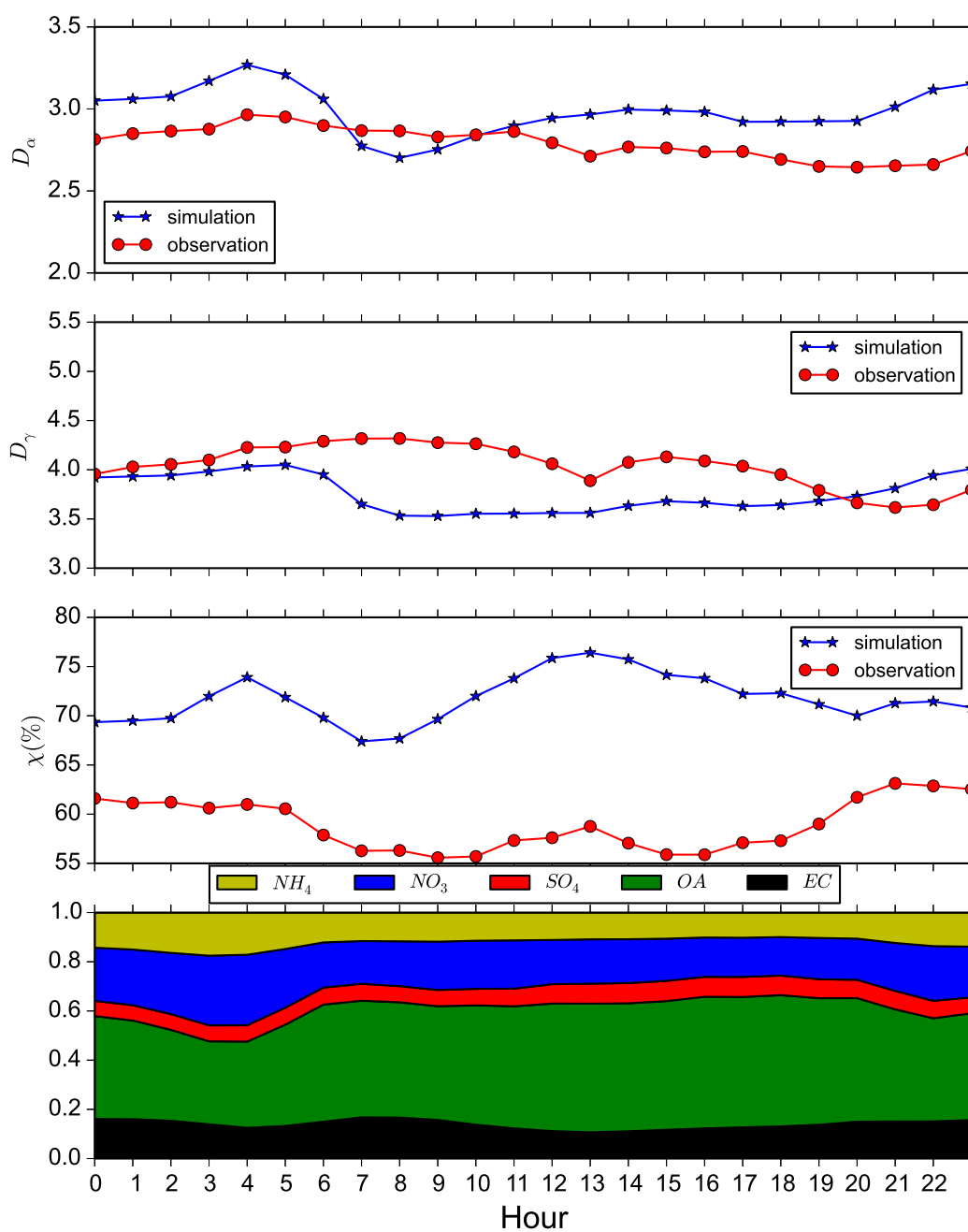


Figure 4.7: Diurnal variations of the mixing state index (χ) and bulk population mass fraction.

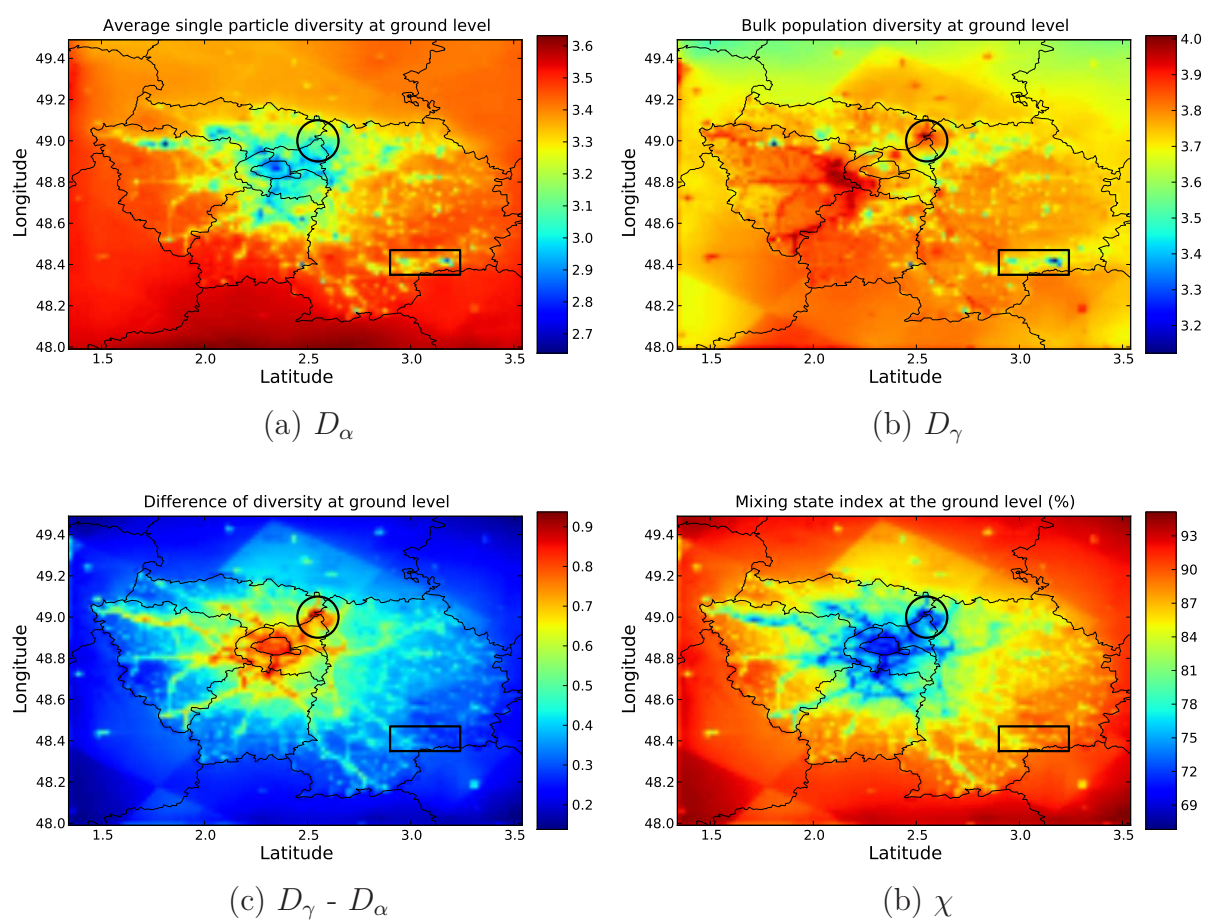


Figure 4.8: Spatial distribution of time-averaged average single particle diversity (D_α , a), average bulk population diversity (D_γ , b), difference between D_α and D_γ (c), and mixing state index (χ , d) over Greater Paris.

areas, because diversity is lower where emissions are high, as freshly emitted particles mostly consist of pure chemical component with a single particle diversity close to 1. The spatial of D_γ is relatively uniform as it represents the number of bulk chemical components. However, there are regions where D_γ can suddenly increase or decrease, and these variations may not be similar to those of D_α . For example, in the region within the black box in Figure 4.8 (strong dust emissions from sand and stone mining industry along the river Seine), some parts have low D_γ and low D_α . This type of region (low D_α and low D_γ) may imply a relatively homogeneous emission source, where only one type of particles is emitted. Other regions, such as the south west of Paris and Roissy airport (delimited by the black circle in Figure 4.8) have low D_α value and high D_γ value. In such regions, there may be heterogeneous emission sources, where particles with distinct compositions may be emitted from the same place or transported to that place. Considering the spatial distribution of the mixing-state index χ , regions with larger difference between D_α and D_γ usually have lower χ , which means they are less internally mixed. Usually, the regions of low χ correspond to regions of low D_α (high traffic emissions). Note that for regions of low D_α but low D_γ , such as within the black box of Figure 4.8, the mixing-state index can be high, although the region may correspond to a location of strong emission. Actually, χ represents the homogeneity of particles, and a group of particles with heterogeneous compositions has a low mixing-state index and is considered as externally mixed. However, a group of particles dominated by a homogeneous composition has a high mixing-state index and it is considered as internally mixed, even if the dominated particles consist of only one species. Such classification of the particle mixing-state is slightly different from the mixing-state identification of Table 4.1, where particles with only one specie or group of chemical compound are considered as unmixed. However, those unmixed particles can have a high mixing-state index, if they dominate the total particle concentration.

4.5 Conclusion

The particle diversity and mixing state is studied with the help of the newly developed size-composition resolved aerosol model (SCRAM) coupled to the Polyphemus air-quality platform. Two simulations are conducted over Greater Paris with different mixing-state assumption (internal mixing IM or external mixing EM).

Both simulations model well the total mass of O_3 , PM_{10} and $PM_{2.5}$, as assessed from comparisons to observations from the BDQA network. The simulation results of both bulk concentrations of chemical species and the concentration of individual particle classes are compared with the observations of Healy et al. [2013]. Good correlations are found between simulation results and measurements for both PM_1 and bulk species concentrations, and the statistics of most species satisfy the model performance criteria proposed by Boylan and Russell [2006], although the concentration of SO_4 is under-estimated during a strong fog event and during periods prevailed by transported continental air masses.

For the concentration of individual particles obtained from the EM simulation, a relatively good consistency is found for the mass fraction of EC-rich and EC-poor particles between simulation results and observations. According to the simulation results, 18.04% of particles are EC-rich particles and 81.96% are EC-poor particles, which is similar to

the ratio from the measurements: 16.78% of EC-rich particles and 83.22% of EC-poor particles. Finally, the single particle diversity and the mixing-state index are computed from the results of the EM simulation based on a new quantification approach developed by Riemer and West [2013], and they are compared with the observation based analyses of Healy et al. [2014] at the urban site LHVP. The average value of the single particle diversity is consistent between the simulation and the measurements (2.91 from the simulation and 2.79 from the measurements). It represents the average effective number of species in each particle. The averaged bulk population diversity, which is the effective number of species in the bulk population, is slightly under-estimated (3.76 from the simulation and 4.04 from the observation), probably because of the under-estimation of sulfate or nitrate in the model. The mixing-state index, which depends on both the single particle diversity and the bulk population diversity, is well represented by the simulation, with a value of 69% from the simulation and 59% from the measurements, indicating that particles are not internally mixed. Finally, the time-averaged spatial distribution of the mixing-state index shows that particles are rather externally mixed in urban regions in and around Paris, while they are rather internally mixed in rural regions. This indicates that traditional aerosol models, which assume that particles are internally mixed, may be suitable for simulating rural regions, while in urbanised areas, the internal-mixing assumption does not hold.

Chapter 5

Conclusion

Résumé

Ce chapitre présente les conclusions et les perspectives de ce travail. Tout d'abord, un nouveau modèle SCRAM (Size-Composition Resolved Aerosol Model) est développé. Dans SCRAM, les particules sont discrétisées selon leurs tailles et compositions. SCRAM est validé par comparaisons avec des simulations "académiques" publiées dans la littérature pour la coagulation de particules en mélange interne et la condensation/évaporation. L'impact du degré de mélange sur les concentrations de particules a ensuite été étudié dans une simulation 0-D en utilisant des données représentatives d'un site trafic en Ile de France. Dans le cas étudié, on constate que la coagulation est très efficace à mélanger les particules et la condensation peut éventuellement diminuer le pourcentage de particules mélangées. Puis SCRAM est intégré dans la plate-forme de qualité de l'air Polyphemus et utilisé pour effectuer des simulations sur l'Ile de France pendant l'été 2009. Une évaluation par comparaison à des observations a montré que SCRAM donne des résultats satisfaisants pour les concentrations de $PM_{2.5}/PM_{10}$ et l'épaisseur optique des aérosols. En outre, l'hypothèse de mélange choisie dans SCRAM influence la formation des particules et leurs propriétés, telles que les propriétés optiques et la formation de noyaux de condensation dans les nuages. Deux simulations sont effectuées (une avec l'hypothèse de MI et l'autre avec l'hypothèse de ME) entre le 15 janvier et le 11 février 2010, pendant la campagne hiver MEGAPOLI durant laquelle les compositions des particules individuelles ont été mesurées. Les résultats des simulations se comparent bien aux mesures de concentration massique de différents composés et aux concentrations de particules riches en carbone élémentaire (EC). Ensuite, un indicateur de la diversité des particules et de l'état de mélange est calculé comme dans l'approche développée par Riemer and West [2013]. La valeur de l'indicateur est cohérente entre la simulation et la mesure. Cet indicateur représente le nombre d'espèces dans chaque particule. La distribution spatiale de l'indicateur montre que les particules sont peu mélangées en région urbaine, tandis qu'elles sont plutôt bien mélangées en région rurale. Enfin, le modèle développé dans cette thèse peut être appliqué à d'autres modèles de qualité de l'air et il y a beaucoup de perspectives pour la recherche et les applications, telles que l'introduction de l'approche dynamique pour la formation des aérosols organiques, des études fines sur les relations

nuages-aérosols, l’identification de sources de pollution et des analyses d’impact.

Sommaire

5.1	Conclusions	124
5.2	Perspectives	126
5.2.1	Dynamic condensation/evaporation of organics	126
5.2.2	Cloud aerosol study	126
5.2.3	Source identifications and impact analysis	127
5.2.4	Improve the computational efficiency	127

5.1 Conclusions

This thesis presents a newly developed size-composition resolved aerosol model (SCRAM) which is able to simulate the dynamics (nucleation, coagulation, condensation/evaporation) of externally-mixed particles in the atmosphere, and it evaluates the performances of SCRAM in three-dimensional simulations. The main work is split into four parts: the research context of external mixing and aerosol modelling; the development of the box model of SCRAM and its validation tests; the 3D application of SCRAM during the summer period of 2009 and the influence of different mixing state assumption on particle properties; the model to data comparison of particle mixing state during winter period of Megapoli campaign.

Firstly, a new box model (SCRAM) is developed based on the discretisation scheme of [Dergaoui et al., 2013], where particles are classified by both their size and composition. Each particle composition is defined by a combination of mass-fraction sections of the different chemical components or aggregate of components. All three main processes involved in aerosol dynamic (coagulation, condensation/evaporation and nucleation) are included in SCRAM. The model is first validated by comparison with a reference solution and results of simulations using internally-mixed particles. The degree of particle mixing is investigated in a 0-D simulation using data representative of air pollution in Greater Paris. The relative influence on the mixing state of the different aerosol processes (condensation/evaporation, coagulation) and of the algorithm used to model condensation/evaporation (bulk equilibrium, dynamic) is studied. It is found that coagulation is quite efficient at mixing particles, as the percentage of mixed particles decreases for both number concentration and mass concentrations when coagulation is not taken into account in the simulation. On the opposite, condensation may decrease the percentage of mixed particles when low-volatility gaseous emissions are high. Besides, the choice of the condensation/evaporation (C/E) approach (bulk equilibrium or dynamic) influences the size and composition distributions, under both the internally-mixed (IM) and externally-mixed (EM) assumptions. While the size and composition distributions simulated with the IM and EM simulations are similar if the bulk-equilibrium approach is used for condensation/evaporation (C/E), the distributions are different if the dynamic approach is used.

Secondly, SCRAM is integrated into the Polyphemus air quality platform and used to conduct simulations over Greater Paris during summer 2009. The evaluation shows

that SCRAM gives satisfactory results for $\text{PM}_{2.5}$, PM_{10} concentrations and aerosol optical depths, as assessed from comparisons to observations. Besides, the model is able to analyze the particle mixing state, as well as the impact of the mixing-state assumptions on particle formation and properties. By comparing results from IM and EM simulations with the dynamic approach for C/E, it is found that EM leads to higher nitrate concentration ($1.24 \mu\text{g m}^{-3}$ on average) than IM ($0.76 \mu\text{g m}^{-3}$ on average), and the differences are especially high for peak concentrations (up to nearly 100% for nitrate). The mixing state of black carbon (BC) is also studied, and it is found that at the urban site of Paris, the unmixed BC percentage is always higher than 35% with peaks around 80% during rush hours, when traffic emissions are the highest. Analyses on particle optical properties show that in general IM simulation leads to higher aerosol optical depth (AOD) and lower signal scattering albedo (SSA). For SSA, the larger differences, up to 11% between the IM and EM simulations, are concentrated in the city of Paris, where BC is mostly unmixed in the EM simulations. For AOD, differences between IM and EM are mostly due to differences in aerosol water content concentrations, which are caused by differences in inorganic aerosol formation. For example, differences of 22% in inorganic concentrations can lead to differences as high as 80% in water concentration and 72% in AOD. Concerning CCN, at low supersaturation, IM leads to lower CCN activation percentage than EM, because the hydrophobic components of IM particles inhibit activation and only the hydrophilic particles of the EM simulation may be activated. At high supersaturation, IM leads to higher CCN activation percentage than EM, because most particles are activated except for the particles that are mostly hydrophobic in the EM simulation. Moreover, at high supersaturation, the differences in the spatial distribution between the IM and EM simulations are more significant over urban regions. However, at low supersaturation, such distribution pattern inverses.

Finally, two simulations are conducted between 15 January and 11 February 2010 where the composition of individual particles is measured during the winter campaign of Megapoli. First, concentrations of O_3 , $\text{PM}_{2.5}$ and PM_{10} are compared with observations from the BDQA database, and their statistics satisfy the published evaluation criteria. Then, the simulation results of the bulk concentrations of chemical species and the concentration of the individual particle classes are compared with the observations of Healy et al. [2013]. Good correlations are found between simulation results and measurements for both PM_1 and bulk species concentrations, and the statistics of PM_1 and BC even satisfy the model performance goals proposed by Boylan and Russell [2006]. For the concentration of individual particles obtained from the EM simulation, a relatively good consistency is found for the mass fraction of BC rich and BC poor particles between simulation results and observations. The simulation estimates that 18.04% of particles are BC-rich particles and 81.96% are BC-poor particles, which is similar to the ratio from the measurements: 16.78% of particles are BC-rich particles and 83.22% of particles are BC-poor particles. The simulated BC-rich particles tend to show a better consistency with observations in terms of mixing state, as most of them are found mixed to other species, similarly to the measurements. Finally, the single particle diversity and the mixing-state index are computed from the results of the EM simulation based on a new quantification approach developed by Riemer and West [2013], and they are compared with the observation based analyses of Healy et al. [2014]. First, the average single particle diversity, which represents the average effective number of species in each particle, is consistent

between the simulation and the measurements (2.91 from the simulation and 2.79 from the measurements). However, the averaged bulk population diversity, which is the effective number of species in the bulk population, is slightly under estimated (3.76 from the simulation and 4.00 from the measurements). This may be due to the under-estimation of sulfate and nitrate in the model. Besides, the model shows a close while slightly higher mixing state index in average, with 69% from the simulation and 59% from the observation. The time averaged spatial distribution of the mixing state index shows that particles are relatively externally mixed in the urban region of Paris, while particles are basically internally mixed in rural regions. This indicates that traditional aerosols model which assume that particles are internally mixed, may be suitable for modelling rural regions. However, they may not be suitable for urbanized areas, where particles are more freshly emitted and less mixed.

5.2 Perspectives

This study presents a new method to model externally-mixed aerosols with a comprehensive representation of particle compositions, and it demonstrates the ability to simulate particle mixing in 3D Eulerian simulations. The model developed in this thesis can be applied to any other air quality models or computational fluid dynamic models, and there are many perspectives for further research and application.

5.2.1 Dynamic condensation/evaporation of organics

The influence of the mixing-state assumption on aerosol formation has been observed for inorganic species. However, the effect of the mixing-state assumption on the formation of organics species could not be investigated in this study, because in the current version of SCRAM, the condensation/evaporation of organic species is solved with the H₂O module, which only contains the bulk equilibrium approach. The bulk equilibrium approach does not distinguish between different particle compositions, as it only considered the partition of total mass between the gas and particle phases. Therefore, more comprehensive investigations could be conducted with SCRAM, regarding the effect of the mixing-state assumption on aerosol formation if the condensation/evaporation of organics is computed dynamically, as done for inorganic species. A newly developed secondary organic aerosol processor (SOAP) [Couvidat and Sartelet, 2014] may be a good choice, as it contains a dynamic representation of organic aerosols.

5.2.2 Cloud aerosol study

In the atmosphere, particles play an essential role for cloud formation, as they are the best candidates for water vapour to condense upon. The condition for a particle to be activated as cloud condensation nuclei (CCN) depends on its diameter and hygroscopicity, which is determined by the chemical composition. Because the external mixing assumption allows particles of different compositions to coexist within the same size section, the activation of a size section would rather be progressive rather than instantaneous as under the internal-mixing assumption. A simple demonstration on how the mixing-state assumption could impact the activation of CCN is made in Chapter 3. It would be interesting to

make further investigations by comparing model predictions with field measurements [Lance et al., 2013; Jurányi et al., 2013]. Furthermore, we could also investigate how the assumption of external mixing could affect the prediction of cloud droplet number concentrations (CDNC) by coupling SCRAM with a cloud convection model.

5.2.3 Source identifications and impact analysis

Another potential application of SCRAM is the source identification and impact analysis. By discretizing the particle composition, it becomes possible to separate different emission sources and study their potential impact over space and time. With SCRAM, different types of emissions could be categorized into different composition sections and their evolutions can be tracked independently. With internal-mixing models, it is difficult to separate different emission sources even if they have distinct compositions. Besides, some toxic chemical components or radioactive pollutants may be released due to accidents or natural disasters. A precise assessment of their potential impact may highly depend on the knowledge of their detailed compositions, as their toxicity could also evolve with their compositions. In such cases, the external-mixing model would definitely provide more accurate information on candidate particles, and offer better impact analysis than internal-mixing models.

5.2.4 Improve the computational efficiency

Although SCRAM is able to simulate externally-mixed particles on a large scale 3-D domain, its computational cost is too high for forecasting or long-term simulations. For example, the external-mixing simulation conducted in chapter 4 takes around 21 minutes to compute a 10 minutes simulation, on a computer equipped with Intel(R) Bi-Xeon E5-2680v2 CPU (10 core-2.8GHz x40). Therefore the computational efficiency of SCRAM should be improved, in order to make it more suitable for daily forecast or long-term simulations. One possibility is to improve the particle composition discretization. Based on the results of previous simulations, it is found that most of the particle mass and number concentrations are concentrated within a few particle composition sections. Several composition sections are almost always empty during the simulation, such as the SO-NO, EC-SO-NO and NO compositions in table 4.5. So, it is possible to optimize the computational efficiency by improving the particle class parametrization: by reducing the total number of particle classes and only conserving the particle classes of significant mass/number concentrations.

Appendix A

Change of variables for the evolution of number and mass distributions

This appendix describes how to derive the equations of change for the number concentration \bar{n} and mass concentration \bar{q} distributions as a function of the variables $f_1, \dots, f_{(c-1)}, m$ used in the external mixing formulation.

To derive the equation of change for $\bar{n}(f_1, \dots, f_{(c-1)}, m)$ (Equation 2.5) from the equation of change for $n(m_1, \dots, m_c)$ (Equation 2.1), we need to perform a change of variables from m_1, \dots, m_c to $f_1, \dots, f_{(c-1)}, m$ and to compute the $[c \times c]$ Jacobian Matrix $\mathbf{J}(f_1, f_2, \dots, f_{(c-1)}, m)$

$$\begin{aligned}
 \mathbf{J} &= \begin{bmatrix} \frac{\partial m_1}{\partial f_1} & \frac{\partial m_1}{\partial f_2} & \cdots & \frac{\partial m_1}{\partial f_{(c-1)}} & \frac{\partial m_1}{\partial m} \\ \frac{\partial m_2}{\partial f_1} & \frac{\partial m_2}{\partial f_2} & \cdots & \frac{\partial m_2}{\partial f_{(c-1)}} & \frac{\partial m_2}{\partial m} \\ \vdots & \vdots & \ddots & \vdots & \vdots \\ \frac{\partial m_{(c-1)}}{\partial f_1} & \frac{\partial m_{(c-1)}}{\partial f_2} & \cdots & \frac{\partial m_{(c-1)}}{\partial f_{(c-1)}} & \frac{\partial m_{(c-1)}}{\partial m} \\ \frac{\partial m_c}{\partial f_1} & \frac{\partial m_c}{\partial f_2} & \cdots & \frac{\partial m_c}{\partial f_{(c-1)}} & \frac{\partial m_c}{\partial m} \end{bmatrix} \\
 &= \begin{bmatrix} m & 0 & \cdots & 0 & f_1 \\ 0 & m & \cdots & 0 & f_2 \\ \vdots & \vdots & \ddots & \vdots & \vdots \\ 0 & 0 & \cdots & m & f_{(c-1)} \\ -m & -m & \cdots & -m & 1 - \sum_{i=1}^{(c-1)} f_i \end{bmatrix}
 \end{aligned} \tag{A.1}$$

and the Jacobian inverse matrix:

$$\mathbf{J}^{-1} = \begin{bmatrix} \frac{1-f_1}{m} & -\frac{f_1}{m} & \dots & -\frac{f_1}{m} & -\frac{f_1}{m} \\ \frac{f_2}{m} & \frac{1-f_2}{m} & \dots & -\frac{f_2}{m} & -\frac{f_2}{m} \\ \vdots & \vdots & \ddots & \vdots & \vdots \\ -\frac{f_{(c-1)}}{m} & -\frac{f_{(c-1)}}{m} & \dots & \frac{1-f_{(c-1)}}{m} & -\frac{f_{(c-1)}}{m} \\ 1 & 1 & \dots & 1 & 1 \end{bmatrix} \quad (\text{A.2})$$

The relationship between n and \bar{n} is

$$n = \frac{\bar{n}}{\det(J)} = \frac{\bar{n}}{m^{(c-1)}} \quad (\text{A.3})$$

Thus,

$$\frac{\partial n}{\partial t} = \frac{\partial(\frac{\bar{n}}{m^{(c-1)}})}{\partial t} = \frac{1}{m^{(c-1)}} \frac{\partial \bar{n}}{\partial t} \quad (\text{A.4})$$

For the right-hand side of Equation (2.1), the terms $\frac{\partial(I_i n)}{\partial m_i}$ are replaced by terms depending on the new variables, using:

$$\begin{aligned} & \left(\frac{\partial(I_1 n)}{\partial m_1}, \frac{\partial(I_2 n)}{\partial m_2}, \dots, \frac{\partial(I_c n)}{\partial m_c} \right) = \\ & \left(\frac{\partial(I_1 n)}{\partial f_1}, \frac{\partial(I_2 n)}{\partial f_2}, \dots, \frac{\partial(I_{(c-1)} n)}{\partial f_{(c-1)}}, \frac{\partial(I_c n)}{\partial m} \right) \times \mathbf{J}^{-1} \end{aligned} \quad (\text{A.5})$$

For $i \in (1, (c-1))$, this leads to:

$$\frac{\partial(I_i n)}{\partial m_i} = \frac{1}{m} \frac{\partial(I_i n)}{\partial f_i} - \sum_{j=1}^{(c-1)} \frac{f_j}{m} \frac{\partial(I_i n)}{\partial f_j} + \frac{\partial(I_i n)}{\partial m} \quad (\text{A.6})$$

and for $i = c$:

$$\frac{\partial(I_c n)}{\partial m_c} = - \sum_{j=1}^{(c-1)} \frac{f_j}{m} \frac{\partial(I_c n)}{\partial f_j} + \frac{\partial(I_c n)}{\partial m} \quad (\text{A.7})$$

If we replace I_c with $I_0 - \sum_{i=1}^{(c-1)} I_i$ in (A.7), we have:

$$\begin{aligned} \frac{\partial(I_c n)}{\partial m_c} &= - \sum_{j=1}^{(c-1)} \frac{f_j}{m} \frac{\partial(I_0 n)}{\partial f_j} + \sum_{i=1}^{(c-1)} \sum_{j=1}^{(c-1)} \frac{f_j}{m} \frac{\partial(I_i n)}{\partial f_j} \\ &+ \frac{\partial(I_0 n)}{\partial m} - \sum_{i=1}^{(c-1)} \frac{\partial(I_i n)}{\partial m} \end{aligned} \quad (\text{A.8})$$

The sum of the first $(c-1)$ terms of the right side of Equation (2.1) may be written as follows.

$$\sum_{i=1}^{(c-1)} \frac{\partial(I_i n)}{\partial m_i} = \frac{1}{m} \sum_{i=1}^{(c-1)} \frac{\partial(I_i n)}{\partial f_i} - \sum_{i=1}^{(c-1)} \sum_{j=1}^{(c-1)} \frac{f_j}{m} \frac{\partial(I_i n)}{\partial f_j} + \sum_{i=1}^{(c-1)} \frac{\partial(I_i n)}{\partial m} \quad (\text{A.9})$$

The right-hand side of Equation (2.1) becomes

$$\begin{aligned} -\sum_{i=1}^c \frac{\partial(I_i n)}{\partial m_i} &= -\sum_{i=1}^{(c-1)} \frac{\partial(I_i n)}{\partial m_i} - \frac{\partial(I_c n)}{\partial m_c} = \\ &= -\frac{1}{m} \sum_{i=1}^{(c-1)} \frac{\partial(I_i n)}{\partial f_i} + \sum_{i=1}^{(c-1)} \frac{f_i}{m} \frac{\partial(I_0 n)}{\partial f_i} - \frac{\partial(I_0 n)}{\partial m} \end{aligned} \quad (\text{A.10})$$

If we denote $H_i = \frac{\partial f_i}{\partial t}$, then I_i may be written as follows.

$$I_i = \frac{\partial m_i}{\partial t} = \frac{\partial(m f_i)}{\partial t} = m \frac{\partial f_i}{\partial t} + f_i \frac{\partial m}{\partial t} = m H_i + f_i I_0 \quad (\text{A.11})$$

Replacing I_i by (A.11) in (A.10) and using $\frac{\partial m}{\partial f_i} = 0$,

$$\begin{aligned} -\sum_{i=1}^c \frac{\partial(I_i n)}{\partial m_i} &= -\frac{1}{m} \sum_{i=1}^{(c-1)} \frac{\partial(m H_i n + f_i I_0 n)}{\partial f_i} + \sum_{i=1}^{(c-1)} \frac{f_i}{m} \frac{\partial(I_0 n)}{\partial f_i} - \frac{\partial(I_0 n)}{\partial m} \\ &= -\sum_{i=1}^{(c-1)} \frac{\partial(H_i n)}{\partial f_i} - \frac{(c-1)}{m} I_0 n - \frac{\partial(I_0 n)}{\partial m} \end{aligned} \quad (\text{A.12})$$

Replacing n with $\frac{\bar{n}}{m^{(c-1)}}$ in Equation (2.1) and using (A.12), we have

$$\begin{aligned} \frac{1}{m^{(c-1)}} \frac{\partial \bar{n}}{\partial t} &= -\sum_{i=1}^{(c-1)} \frac{\partial(H_i \frac{\bar{n}}{m^{(c-1)}})}{\partial f_i} - \frac{(c-1)}{m^c} I_0 \bar{n} - \frac{\partial(I_0 \frac{\bar{n}}{m^{(c-1)}})}{\partial m} \\ &= -\frac{1}{m^{(c-1)}} \sum_{i=1}^{(c-1)} \frac{\partial(H_i \bar{n})}{\partial f_i} - \frac{1}{m^{(c-1)}} \frac{\partial(I_0 \bar{n})}{\partial m} \end{aligned} \quad (\text{A.13})$$

and the equation of change for \bar{n} is finally

$$\frac{\partial \bar{n}}{\partial t} = -\sum_{i=1}^{(c-1)} \frac{\partial(H_i \bar{n})}{\partial f_i} - \frac{\partial(I_0 \bar{n})}{\partial m} \quad (\text{A.14})$$

The equation of change for the mass distribution $q_i = n m_i$ of species i is derived as follows.

$$\frac{\partial q_i}{\partial t} = \frac{\partial n m_i}{\partial t} = -m_i \frac{\partial n}{\partial t} + n I_i \quad (\text{A.15})$$

And the equation of change for \bar{q}_i is obtained using $n = \frac{\bar{n}}{m^{(c-1)}}$, $q_i = \frac{\bar{q}_i}{m^{(c-1)}}$ and $m_i = m f_i$

$$\frac{\partial \bar{q}_i}{\partial t} = -m f_i \frac{\partial \bar{n}}{\partial t} + \bar{n} I_i \quad (\text{A.16})$$

Appendix B

The time derivation of Equation (2.10) and (2.9)

The time derivation of Equation (2.10) leads to:

$$\begin{aligned}
\frac{\partial N^j}{\partial t} &= \overbrace{\int_{m_k^-}^{m_k^+} \int_{f_{g_1}^-}^{f_{g_1}^+} \cdots \int_{f_{g_{(c-1)}}^-}^{f_{g_{(c-1)}}^+} \frac{\partial \bar{n}}{\partial t} dm df_{g_1}, \dots, df_{g_{(c-1)}}}^A \\
&+ \overbrace{\frac{dm_k^+}{dt} \int_{f_{g_1}^-}^{f_{g_1}^+} \cdots \int_{f_{g_{(c-1)}}^-}^{f_{g_{(c-1)}}^+} \bar{n}(m_k^+, f_{g_1}, \dots, f_{g_{(c-1)}}) df_{g_1}, \dots, df_{g_{(c-1)}}}^B \\
&- \frac{dm_k^-}{dt} \int_{f_{g_1}^-}^{f_{g_1}^+} \cdots \int_{f_{g_{(c-1)}}^-}^{f_{g_{(c-1)}}^+} \bar{n}(m_k^-, f_{g_1}, \dots, f_{g_{(c-1)}}) df_{g_1}, \dots, df_{g_{(c-1)}} \\
&+ \sum_{i=1}^{(c-1)} \left[\frac{df_{g_i}^+}{dt} \int_{m_k^-}^{m_k^+} \int_{f_{g_1}^-}^{f_{g_1}^+} \cdots \int_{f_{g_{i-1}}^-}^{f_{g_{i-1}}^+} \int_{f_{g_{i+1}}^-}^{f_{g_{i+1}}^+} \cdots \int_{f_{g_{(c-1)}}^-}^{f_{g_{(c-1)}}^+} \bar{n}(m, f_{g_1}, \right. \\
&\quad \left. \dots, f_{g_{i-1}}, f_{g_i}^+, f_{g_{i+1}}, \dots, f_{g_{(c-1)}}) dm df_{g_1} \dots df_{g_{i-1}} df_{g_{i+1}} \dots df_{g_{(c-1)}} \right. \\
&\quad \left. - \frac{df_{g_i}^-}{dt} \int_{m_k^-}^{m_k^+} \int_{f_{g_1}^-}^{f_{g_1}^+} \cdots \int_{f_{g_{i-1}}^-}^{f_{g_{i-1}}^+} \int_{f_{g_{i+1}}^-}^{f_{g_{i+1}}^+} \cdots \int_{f_{g_{(c-1)}}^-}^{f_{g_{(c-1)}}^+} \bar{n}(m, f_{g_1}, \dots, f_{g_{i-1}}, \right. \\
&\quad \left. f_{g_i}^-, f_{g_{i+1}}, \dots, f_{g_{(c-1)}}) dm df_{g_1} \dots df_{g_{i-1}} df_{g_{i+1}} \dots df_{g_{(c-1)}} \right]
\end{aligned} \tag{B.1}$$

Replacing $\frac{\partial \bar{n}}{\partial t}(m, f_{g_1}, \dots, f_{g_{(c-1)}})$ by Equation (2.5), we have

$$A = \int_{m_k^-}^{m_k^+} \int_{f_{g_1}^-}^{f_{g_1}^+} \cdots \int_{f_{g_{(c-1)}}^-}^{f_{g_{(c-1)}}^+} \left[-\frac{\partial(I_0 n)}{\partial m} - \sum_{x=1}^{(c-1)} \frac{\partial(H_{g_x} n)}{\partial f_{g_x}} \right] dm df_{g_1} \dots df_{g_{(c-1)}} \tag{B.2}$$

and using $I_0 = \frac{dm}{dt}$, $H_{g_i} = \frac{df_{g_i}}{dt}$ and $\frac{\partial f_{g_i}}{\partial f_{g_l}} = 0$ when $i \neq l$

$$\begin{aligned}
A = & - \left\{ \frac{dm_k^+}{dt} \int_{f_{g_1}^-}^{f_{g_1}^+} \dots \int_{f_{g_{(c-1)}}^-}^{f_{g_{(c-1)}}^+} \bar{n}(m_k^+, f_{g_1}, \dots, f_{g_{(c-1)}}) dm df_{g_1} \dots df_{g_{(c-1)}} \right. \\
& - \frac{dm_k^-}{dt} \int_{f_{g_1}^-}^{f_{g_1}^+} \dots \int_{f_{g_{(c-1)}}^-}^{f_{g_{(c-1)}}^+} \bar{n}(m_k^-, f_{g_1}, \dots, f_{g_{(c-1)}}) dm df_{g_1} \dots df_{g_{(c-1)}} \\
& + \sum_{i=1}^{(c-1)} \left[\frac{df_{g_i}^+}{dt} \int_{m_k^-}^{m_k^+} \int_{f_{g_1}^-}^{f_{g_1}^+} \dots \int_{f_{g_{i-1}}^-}^{f_{g_{i-1}}^+} \int_{f_{g_{i+1}}^-}^{f_{g_{i+1}}^+} \dots \int_{f_{g_{(c-1)}}^-}^{f_{g_{(c-1)}}^+} \bar{n}(m, f_{g_1}, \right. \\
& \dots, f_{g_{i-1}}, f_{g_i}^+, f_{g_{i+1}}, \dots, f_{g_{(c-1)}}) dm df_{g_1} \dots df_{g_{i-1}} df_{g_{i+1}} \dots df_{g_{(c-1)}} \\
& - \frac{df_{g_i}^-}{dt} \int_{m_k^-}^{m_k^+} \int_{f_{g_1}^-}^{f_{g_1}^+} \dots \int_{f_{g_{i-1}}^-}^{f_{g_{i-1}}^+} \int_{f_{g_{i+1}}^-}^{f_{g_{i+1}}^+} \dots \int_{f_{g_{(c-1)}}^-}^{f_{g_{(c-1)}}^+} \bar{n}(m, f_{g_1}, \dots, f_{g_{i-1}}, \\
& \left. \left. f_{g_i}^-, f_{g_{i+1}}, \dots, f_{g_{(c-1)}}) dm df_{g_1} \dots df_{g_{i-1}} df_{g_{i+1}} \dots df_{g_{(c-1)}} \right] \right\}
\end{aligned} \tag{B.3}$$

So $A = -B$, thus

$$\frac{\partial N^j}{\partial t} = (A + B) = 0 \tag{B.4}$$

which is expected since condensation/evaporation does not affect the total number of particles.

Similarly, an equation of change can be derived for Q_i^j . In order to simplify the writing of the equations, the following abbreviations are introduced:

$$\begin{aligned}
f_{g_1^{(c-1)}} &= f_{g_1}, \dots, f_{g_{(c-1)}} \\
f_{g_1^{(c-1)} \setminus i} &= f_{g_1}, \dots, f_{g_{i-1}}, f_{g_{i+1}}, \dots, f_{g_{(c-1)}} \\
df_{g_1^{(c-1)}} &= df_{g_1} \dots df_{g_{(c-1)}} \\
df_{g_1^{(c-1)} \setminus i} &= df_{g_1} \dots df_{g_{i-1}} df_{g_{i+1}} \dots df_{g_{(c-1)}} \\
\int_{f_{g_1^{(c-1)}}^-}^{f_{g_1^{(c-1)}}^+} &= \int_{f_{g_1}^-}^{f_{g_1}^+} \dots \int_{f_{g_{(c-1)}}^-}^{f_{g_{(c-1)}}^+} \\
\int_{f_{g_1^{(c-1)} \setminus i}^-}^{f_{g_1^{(c-1)} \setminus i}^+} &= \int_{f_{g_1}^-}^{f_{g_1}^+} \dots \int_{f_{g_{i-1}}^-}^{f_{g_{i-1}}^+} \int_{f_{g_{i+1}}^-}^{f_{g_{i+1}}^+} \dots \int_{f_{g_{(c-1)}}^-}^{f_{g_{(c-1)}}^+}
\end{aligned}$$

The time derivation of Equation (2.9) leads to:

$$\begin{aligned}
\frac{\partial Q_i^j}{\partial t} &= \int_{m_k^-}^{m_k^+} \int_{f_{g_1}^{-(c-1)}}^{f_{g_1}^{+(c-1)}} \frac{\partial \bar{q}_i}{\partial t} dm df_{g_1}^{(c-1)} \\
&+ \frac{dm_k^+}{dt} \int_{f_{g_1}^{-(c-1)}}^{f_{g_1}^{+(c-1)}} \bar{q}_i(m_k^+, f_{g_1}^{(c-1)}) df_{g_1}^{(c-1)} - \frac{dm_k^-}{dt} \int_{f_{g_1}^{-(c-1)}}^{f_{g_1}^{+(c-1)}} \bar{q}_i(m_k^-, f_{g_1}^{(c-1)}) df_{g_1}^{(c-1)} \\
&+ \sum_{i=1}^{(c-1)} \left[\frac{df_{g_1}^{+(c-1)}}{dt} \int_{m_k^-}^{m_k^+} \int_{f_{g_1}^{-(c-1)\setminus i}}^{f_{g_1}^{+(c-1)\setminus i}} \bar{q}_i(m, f_{g_i}^+, f_{g_1}^{(c-1)\setminus i}) dm df_{g_1}^{(c-1)\setminus i} \right. \\
&\quad \left. - \frac{df_{g_1}^{-(c-1)}}{dt} \int_{m_k^-}^{m_k^+} \int_{f_{g_1}^{-(c-1)\setminus i}}^{f_{g_1}^{+(c-1)\setminus i}} \bar{q}_i(m, f_{g_i}^-, f_{g_1}^{(c-1)\setminus i}) dm df_{g_1}^{(c-1)\setminus i} \right]
\end{aligned} \tag{B.5}$$

Substituting Equation (A.16) and $\bar{q}_i = m f_i \bar{n}$ into Equation (B.5), we obtain:

$$\begin{aligned}
\frac{\partial Q_i^j}{\partial t} &= \overbrace{\int_{m_k^-}^{m_k^+} \int_{f_{g_1}^{-(c-1)}}^{f_{g_1}^{+(c-1)}} m f_{g_i} \frac{\partial \bar{n}}{\partial t} dm df_{g_1}^{(c-1)}}^C + \int_{m_k^-}^{m_k^+} \int_{f_{g_1}^{-(c-1)}}^{f_{g_1}^{+(c-1)}} \bar{n} I_{g_i} dm df_{g_1}^{(c-1)} \\
&\quad + \overbrace{m_k^+ \frac{dm_k^+}{dt} \int_{f_{g_1}^{-(c-1)}}^{f_{g_1}^{+(c-1)}} f_{g_i} \bar{n}(m_k^+, f_{g_1}^{(c-1)}) df_{g_1}^{(c-1)} - m_k^- \frac{dm_k^-}{dt} \int_{f_{g_1}^{-(c-1)}}^{f_{g_1}^{+(c-1)}} f_{g_i} \bar{n}(m_k^-, f_{g_1}^{(c-1)}) df_{g_1}^{(c-1)}}^D \\
&+ \sum_{i=1}^{(c-1)} \left[f_{g_i}^+ \frac{df_{g_1}^{+(c-1)}}{dt} \int_{m_k^-}^{m_k^+} \int_{f_{g_1}^{-(c-1)\setminus i}}^{f_{g_1}^{+(c-1)\setminus i}} m \bar{n}(m, f_{g_i}^+, f_{g_1}^{(c-1)\setminus i}) dm df_{g_1}^{(c-1)\setminus i} \right. \\
&\quad \left. - f_{g_i}^- \frac{df_{g_1}^{-(c-1)}}{dt} \int_{m_k^-}^{m_k^+} \int_{f_{g_1}^{-(c-1)\setminus i}}^{f_{g_1}^{+(c-1)\setminus i}} m \bar{n}(m, f_{g_i}^-, f_{g_1}^{(c-1)\setminus i}) dm df_{g_1}^{(c-1)\setminus i} \right]
\end{aligned} \tag{B.6}$$

Similarly to Equation (B.1), it can be proved that $C = -D$, so that Equation (B.6) simplifies to:

$$\frac{\partial Q_i^j}{\partial t} = \int_{m_k^-}^{m_k^+} \int_{f_{g_1}^{-(c-1)}}^{f_{g_1}^{+(c-1)}} \bar{n} I_{g_i} dm df_{g_1}^{(c-1)} = N^j I_{g_i} \tag{B.7}$$

Thus, in each section, the change with time of number and mass concentrations is given by Equations (B.4) and (B.7).

Bibliography

- Airparif: Ile-de-France gridded emission inventory 2005 (version2008), URL <http://www.airparif.asso.fr/>, 2010. 75
- Albrecht, B. A.: Aerosols, cloud microphysics, and fractional cloudiness, *Science*, 245, 1227–1230, 1989. 21
- Anderson, B. J., Musicant, D. R., Ritz, A. M., Ault, A., Gross, D., Yuen, M., and Gälli, M.: User-friendly clustering for atmospheric data analysis, Carleton College, Northfield, MN, Technical Report, 2005. 101
- Anthony, H. K. and Mary-Scott, K.: *The Long-Range Atmospheric Transport of Natural and Contaminant Substances*, Springer, St. Georges, Bermuda, 1990. 18
- Ault, A. P., Gaston, C. J., Wang, Y., Dominguez, G., Thiemens, M. H., and Prather, K. A.: Characterization of the single particle mixing state of individual ship plume events measured at the port of Los Angeles, *Environmental science & technology*, 44, 1954–1961, 2010. 97
- Bauer, S., Wright, D., Koch, D., Lewis, E., McGraw, R., Chang, L.-S., Schwartz, S., and Ruedy, R.: MATRIX (Multiconfiguration Aerosol TRacker of mIXing state): an aerosol microphysical module for global atmospheric models, *Atmospheric Chemistry and Physics*, 8, 6003–6035, 2008. 36, 46, 73, 98
- Bessagnet, B., Hodzic, A., Vautard, R., Beekmann, M., Cheinet, S., Honoré, C., Liousse, C., and Rouil, L.: Aerosol modeling with CHIMERE—preliminary evaluation at the continental scale, *Atmospheric Environment*, 38, 2803–2817, 2004. 107
- Binkowski, F. S. and Roselle, S. J.: Models-3 Community Multiscale Air Quality (CMAQ) model aerosol component 1. Model description, *Journal of Geophysical Research: Atmospheres* (1984–2012), 108, 2003. 36, 45
- Bohren, C. F. and Huffman, D. R.: *Absorption and scattering of light by small particles*, John Wiley & Sons, 1983. 84
- Boylan, J. W. and Russell, A. G.: PM and light extinction model performance metrics, goals, and criteria for three-dimensional air quality models, *Atmospheric environment*, 40, 4946–4959, 2006. 38, 77, 85, 103, 107, 114, 121, 125
- Byun, D. and Schere, K. L.: Review of the governing equations, computational algorithms, and other components of the Models-3 Community Multiscale Air Quality (CMAQ) modeling system, *Applied Mechanics Reviews*, 59, 51–77, 2006. 34

- Capaldo, K., Pilinis, C., and Pandis, S. N.: A computationally efficient hybrid approach for dynamic gas/aerosol transfer in air quality models, *Atmospheric Environment*, 34, 3617–3627, 2000. 51
- Charron, A. and Aymoz, G.: PM-DRIVE: Particulate DiRect and Indirect On-Road Vehicular Emissions, Tech. rep., L’Agence de l’Environnement et de la Maîtrise de l’Energie (ADEME), 2015. 101
- Colbeck, I. et al.: *Aerosol Science: Technology and Applications*, John Wiley & Sons, 2014. 9, 18, 24
- Couvidat, F. and Sartelet, K.: The Secondary Organic Aerosol Processor (SOAP v1. 0) model: a unified model with different ranges of complexity based on the molecular surrogate approach, *Geoscientific Model Development Discussions*, 7, 379–429, 2014. 126
- Couvidat, F. and Sartelet, K.: The Secondary Organic Aerosol Processor (SOAP v1. 0) model: a unified model with different ranges of complexity based on the molecular surrogate approach, *Geoscientific Model Development*, 8, 1111–1138, 2015. 79
- Couvidat, F., Debry, É., Sartelet, K., and Seigneur, C.: A hydrophilic/hydrophobic organic (H₂O) aerosol model: Development, evaluation and sensitivity analysis, *Journal of Geophysical Research: Atmospheres* (1984–2012), 117, doi: 10.1029/2011JD017214, 2012. 45, 51, 57, 74, 76, 99, 101
- Couvidat, F., Kim, Y., Sartelet, K., Seigneur, C., Marchand, N., and Sciare, J.: Modeling secondary organic aerosol in an urban area: application to Paris, France, *Atmospheric Chemistry and Physics*, 13, 983–996, 2013. 55, 57, 59, 70, 75, 77, 101, 103
- Crippa, M., Canonaco, F., Slowik, J., El Haddad, I., De-Carlo, P., Mohr, C., Heringa, M., Chirico, R., Marchand, N., Temime-Roussel, B., et al.: Primary and secondary organic aerosol origin by combined gas-particle phase source apportionment, *Atmos. Chem. Phys*, 13, 8411–8426, 2013. 23
- Crosbie, E., Youn, J.-S., Balch, B., Wonaschütz, A., Shingler, T., Wang, Z., Conant, W., Betterton, E., and Sorooshian, A.: On the competition among aerosol number, size and composition in predicting CCN variability: a multi-annual field study in an urbanized desert, *Atmospheric Chemistry and Physics Discussions*, 15, 3863–3906, 2015. 97
- Dahneke, B.: Simple kinetic theory of Brownian diffusion in vapors and aerosols, in: *Theory of Dispersed Multiphase Flow*, pp. 97–133, Academic Press, 1983. 32, 47, 110
- Dall’Osto, M., Ovadnevaite, J., Ceburnis, D., Martin, D., Healy, R. M., O’Connor, I., Kourtchev, I., Sodeau, J., Wenger, J., and O’Dowd, C.: Characterization of urban aerosol in Cork city (Ireland) using aerosol mass spectrometry, *Atmospheric Chemistry and Physics*, 13, 4997–5015, 2013. 97
- Davidson, C. I., Phalen, R. F., and Solomon, P. A.: Airborne particulate matter and human health: a review, *Aerosol Science and Technology*, 39, 737–749, 2005. 20, 73

- Deboudt, K., Flament, P., Choël, M., Gloter, A., Sobanska, S., and Colliex, C.: Mixing state of aerosols and direct observation of carbonaceous and marine coatings on African dust by individual particle analysis, *Journal of Geophysical Research: Atmospheres* (1984–2012), 115, 2010a. 45
- Deboudt, K., Flament, P., Choël, M., Gloter, A., Sobanska, S., and Colliex, C.: Mixing state of aerosols and direct observation of carbonaceous and marine coatings on African dust by individual particle analysis, *Journal of Geophysical Research: Atmospheres* (1984–2012), 115, doi: 10.1029/2010JD013921, 2010b. 27, 32
- Debry, E. and Sportisse, B.: Reduction of the condensation/evaporation dynamics for atmospheric aerosols: Theoretical and numerical investigation of hybrid methods, *Journal of Aerosol Science*, 37, 950–966, 2006. 49, 51
- Debry, E., Fahey, K., Sartelet, K., Sportisse, B., and Tombette, M.: Technical Note: A new SIze REsolved Aerosol Model (SIREAM), *Atmospheric Chemistry and Physics*, 7, 1537–1547, 2007a. 47, 50, 97
- Debry, E., Fahey, K., Sartelet, K., Sportisse, B., and Tombette, M.: Technical Note: A new SIze REsolved Aerosol Model (SIREAM), *Atmospheric Chemistry and Physics*, 7, 1537–1547, 2007b. 36
- DeCarlo, P. F., Kimmel, J. R., Trimborn, A., Northway, M. J., Jayne, J. T., Aiken, A. C., Gonin, M., Fuhrer, K., Horvath, T., Docherty, K. S., et al.: Field-deployable, high-resolution, time-of-flight aerosol mass spectrometer, *Analytical chemistry*, 78, 8281–8289, 2006. 97
- Decesari, S., Allan, J., Plass-Duelmer, C., Williams, B., Paglione, M., Facchini, M., O’Dowd, C., Harrison, R., Gietl, J., Coe, H., et al.: Measurements of the aerosol chemical composition and mixing state in the Po Valley using multiple spectroscopic techniques, *Atmospheric Chemistry and Physics*, 14, 12 109–12 132, 2014. 27
- Dergaoui, H., Sartelet, K. N., Debry, É., and Seigneur, C.: Modeling coagulation of externally mixed particles: Sectional approach for both size and chemical composition, *Journal of Aerosol Science*, 58, 17 – 32, 2013. 37, 38, 41, 42, 43, 46, 47, 48, 54, 73, 74, 97, 124
- Devilliers, M., Debry, E., Sartelet, K., and Seigneur, C.: A new algorithm to solve condensation/evaporation for ultra fine, fine, and coarse particles, *Journal of Aerosol Science*, 2012. 36
- Devilliers, M., Debry, É., Sartelet, K., and Seigneur, C.: A new algorithm to solve condensation/evaporation for ultra fine, fine, and coarse particles, *Journal of Aerosol Science*, 55, 116–136, 2013. 50
- Djouad, R., Sportisse, B., and Audiffren, N.: Numerical simulation of aqueous-phase atmospheric models: use of a non-autonomous Rosenbrock method, *Atmospheric Environment*, 36, 873–879, 2002. 50

- Doll, D. C.: Guideline for regulatory application of the Urban Airshed Model, Tech. rep., Environmental Protection Agency, Research Triangle Park, NC (United States). Office of Air Quality Planning and Standards, 1991. 37
- Doyle, G. J.: Self-Nucleation in the Sulfuric Acid-Water System, *The Journal of Chemical Physics*, 35, 795–799, 1961. 30
- EPA, D.: Integrated science assessment for particulate matter, Tech. rep., US Environmental Protection Agency Washington, DC, 2009. 45
- EU Air Quality Standards: Air Quality Standards - Environment - European Commission, URL <http://ec.europa.eu/environment/air/quality/standards.htm>, [Online; accessed 26-March-2015], 2015. 20
- Fahey, K. M. and Pandis, S. N.: Optimizing model performance: variable size resolution in cloud chemistry modeling, *Atmospheric Environment*, 35, 4471–4478, 2001. 75, 98
- Fitzgerald, E., Ault, A. P., Zauscher, M., Mayol-Bracero, O. L., and Prather, K. A.: Comparison of the mixing state of long-range transported Asian and African mineral dust, *Atmospheric Environment*, 2015. 29
- Furutani, H., Dall’osto, M., Roberts, G. C., and Prather, K. A.: Assessment of the relative importance of atmospheric aging on CCN activity derived from field observations, *Atmospheric Environment*, 42, 3130–3142, 2008. 97
- GB 3095—2012: Ambient air quality standards GB 3095—2012, The Ministry of Environmental Protection of China, URL http://kjs.mep.gov.cn/hjbhbz/bzwb/dqhjbh/dqhjz1bz/201203/t20120302_224165.htm, 2012. 20
- Gelbard, F. and Seinfeld, J. H.: The general dynamic equation for aerosols. Theory and application to aerosol formation and growth, *Journal of Colloid and Interface Science*, 68, 363–382, 1979. 33
- Gelbard, F. and Seinfeld, J. H.: Simulation of multicomponent aerosol dynamics, *Journal of colloid and Interface Science*, 78, 485–501, 1980. 36, 45
- Gelbard, F., Tambour, Y., and Seinfeld, J. H.: Sectional representations for simulating aerosol dynamics, *Journal of Colloid and Interface Science*, 76, 541–556, 1980. 25, 36
- Goliff, W. S. and Stockwell, W. R.: The regional atmospheric chemistry mechanism, version 2, an update, International conference on Atmospheric Chemical Mechanisms, University of California, Davis, 96, 2008. 36
- Grell, G. A., Peckham, S. E., Schmitz, R., McKeen, S. A., Frost, G., Skamarock, W. C., and Eder, B.: Fully coupled “online” chemistry within the WRF model, *Atmospheric Environment*, 39, 6957–6975, 2005. 34

- Guenther, A., Karl, T., Harley, P., Wiedinmyer, C., Palmer, P., and Geron, C.: Estimates of global terrestrial isoprene emissions using MEGAN (Model of Emissions of Gases and Aerosols from Nature), *Atmospheric Chemistry and Physics Discussions*, 6, 107–173, 2006. 75, 99
- Hansen, J. and Nazarenko, L.: Soot climate forcing via snow and ice albedos, *Proceedings of the National Academy of Sciences of the United States of America*, 101, 423–428, 2004. 22
- Hansen, J., Sato, M., and Ruedy, R.: Radiative forcing and climate response, *Journal of Geophysical Research: Atmospheres* (1984–2012), 102, 6831–6864, 1997. 21
- Healy, R. M., Sciare, J., Poulain, L., Kamili, K., Merkel, M., Müller, T., Wiedensohler, A., Eckhardt, S., Stohl, A., Sarda-Estève, R., et al.: Sources and mixing state of size-resolved elemental carbon particles in a European megacity: Paris, *Atmospheric Chemistry and Physics*, 12, 1681–1700, 2012. 27, 39, 45, 57, 67, 73, 94, 95, 97
- Healy, R. M., Sciare, J., Poulain, L., Crippa, M., Wiedensohler, A., Prévôt, A. S., Baltensperger, U., Sarda-Estève, R., McGuire, M. L., Jeong, C.-H., et al.: Quantitative determination of carbonaceous particle mixing state in Paris using single-particle mass spectrometer and aerosol mass spectrometer measurements, *Atmospheric Chemistry and Physics*, 13, 9479–9496, 2013. 13, 14, 27, 73, 95, 97, 98, 101, 103, 106, 107, 108, 110, 111, 113, 121, 125
- Healy, R. M., Riemer, N., Wenger, J., Murphy, M., West, M., Poulain, L., Wiedensohler, A., O'Connor, I., McGillicuddy, E., Sodeau, J., et al.: Single particle diversity and mixing state measurements, *Atmospheric Chemistry and Physics*, 14, 6289–6299, 2014. 27, 39, 97, 98, 114, 115, 117, 122, 125
- Herich, H., Kammermann, L., Friedman, B., Gross, D. S., Weingartner, E., Lohmann, U., Spichtinger, P., Gysel, M., Baltensperger, U., and Cziczo, D. J.: Subarctic atmospheric aerosol composition: 2. Hygroscopic growth properties, *Journal of Geophysical Research: Atmospheres* (1984–2012), 114, doi: /10.1029/2008JD011574, 2009. 97
- Hess, M., Koepke, P., and Schult, I.: Optical properties of aerosols and clouds: The software package OPAC, *Bulletin of the American meteorological society*, 79, 831–844, 1998. 84
- Hinds, W. C.: *Aerosol technology: properties, behavior, and measurement of airborne particles*, John Wiley & Sons, 2012. 24
- Hoffmann, T., Odum, J. R., Bowman, F., Collins, D., Klockow, D., Flagan, R. C., and Seinfeld, J. H.: Formation of organic aerosols from the oxidation of biogenic hydrocarbons, *Journal of Atmospheric Chemistry*, 26, 189–222, 1997. 30
- Holben, B., Eck, T., Slutsker, I., Tanre, D., Buis, J., Setzer, A., Vermote, E., Reagan, J., Kaufman, Y., Nakajima, T., et al.: AERONET—A federated instrument network and data archive for aerosol characterization, *Remote sensing of environment*, 66, 1–16, 1998. 84

- Holben, B., Smirnov, A., Eck, T., Slutsker, I., Abuhassan, N., Newcomb, W., Schafer, J., Tanre, D., Chatenet, B., and Lavenu, F.: An emerging ground-based aerosol climatology- Aerosol optical depth from AERONET, *Journal of Geophysical Research*, 106, 12 067–12 097, 2001. 84
- Hong, S.-Y. and Lim, J.-O. J.: The WRF single-moment 6-class microphysics scheme (WSM6), *Asia-Pacific Journal of Atmospheric Sciences*, 42, 129–151, 2006. 101
- Hong, S.-Y., Noh, Y., and Dudhia, J.: A new vertical diffusion package with an explicit treatment of entrainment processes, *Monthly Weather Review*, 134, 2318–2341, 2006. 75, 101
- Horowitz, L. W., Walters, S., Mauzerall, D. L., Emmons, L. K., Rasch, P. J., Granier, C., Tie, X., Lamarque, J.-F., Schultz, M. G., Tyndall, G. S., et al.: A global simulation of tropospheric ozone and related tracers: Description and evaluation of MOZART, version 2, *Journal of Geophysical Research: Atmospheres* (1984–2012), 108, doi: 10.1029/2002JD002853, 2003. 99
- Hughes, L. S., Allen, J. O., Bhave, P., Kleeman, M. J., Cass, G. R., Liu, D.-Y., Fergenson, D. P., Morrical, B. D., and Prather, K. A.: Evolution of atmospheric particles along trajectories crossing the Los Angeles basin, *Environmental science & technology*, 34, 3058–3068, 2000. 27, 45
- Hussgroup.com: Diesel particulates are invisible but dangerous, URL <http://www.hussgroup.com/cdc/en/infocenter/PM.php>, [Online; accessed 26-March-2015], 2015. 9, 19
- Intergovernment Panel on Climate Control (IPCC): Climate Change 2007, the fourth Assessment Report of the IPCC, Cambridge Univ. Press, New York, USA, 2007. 9, 22
- Jacobson, M.: Analysis of aerosol interactions with numerical techniques for solving coagulation, nucleation, condensation, dissolution, and reversible chemistry among multiple size distributions, *Journal of Geophysical Research*, 107, 1327–1338, 2002a. 37, 42, 46, 73, 97
- Jacobson, M. Z.: Development and application of a new air pollution modeling system—II. Aerosol module structure and design, *Atmospheric Environment*, 31, 131–144, 1997. 47, 50
- Jacobson, M. Z.: Strong radiative heating due to the mixing state of black carbon in atmospheric aerosols, *Nature*, 409, 695–697, 2001. 46, 73
- Jacobson, M. Z.: Atmospheric pollution: history, science, and regulation, Cambridge University Press, 2002b. 24
- Jacobson, M. Z.: Control of fossil-fuel particulate black carbon and organic matter, possibly the most effective method of slowing global warming, *Journal of Geophysical Research: Atmospheres* (1984–2012), 107, ACH–16, 2002c. 21, 73

- Jacobson, M. Z., Turco, R. P., Jensen, E. J., and Toon, O. B.: Modeling coagulation among particles of different composition and size, *Atmospheric Environment*, 28, 1327–1338, 1994. 36, 37, 42, 46, 73, 97
- Jurányi, Z., Tritscher, T., Gysel, M., Laborde, M., Gomes, L., Roberts, G., Baltensperger, U., and Weingartner, E.: Hygroscopic mixing state of urban aerosol derived from size-resolved cloud condensation nuclei measurements during the MEGAPOLI campaign in Paris, *Atmospheric Chemistry and Physics*, 13, 6431–6446, 2013. 127
- Kain, J. S.: The Kain-Fritsch convective parameterization: an update, *Journal of Applied Meteorology*, 43, 170–181, 2004. 101
- Kim, Y., Sartelet, K., Raut, J.-C., and Chazette, P.: Evaluation of the Weather Research and Forecast/urban model over Greater Paris, *Boundary-layer meteorology*, 149, 105–132, 2013. 75, 101
- Kleeman, M. J. and Cass, G. R.: A 3D Eulerian source-oriented model for an externally mixed aerosol, *Environmental science & technology*, 35, 4834–4848, 2001. 36, 46, 73, 97
- Kleeman, M. J., Cass, G. R., and Eldering, A.: Modeling the airborne particle complex as a source-oriented external mixture, *Journal of Geophysical Research: Atmospheres* (1984–2012), 102, 21 355–21 372, 1997. 36, 46
- Koehler, K. A., DeMott, P. J., Kreidenweis, S. M., Popovicheva, O. B., Petters, M. D., Carrico, C. M., Kireeva, E. D., Khokhlova, T. D., and Shonija, N. K.: Cloud condensation nuclei and ice nucleation activity of hydrophobic and hydrophilic soot particles, *Physical Chemistry Chemical Physics*, 11, 7906–7920, 2009. 21
- Köhler, H.: Zur kondensation des wasserdampfe in der atmosphäre, *Geofys. Publ*, 2, 1921. 89
- Köhler, H.: Zur Thermodynamik der Kondensation an hygroskopischen Kernen und Bemerkungen über das Zusammenfließen der Tropfen, *Statens meteorologisk-hydrografiska anstalt*, 1926. 89
- Kulmala, M., Pirjola, L., and Mäkelä, J. M.: Stable sulphate clusters as a source of new atmospheric particles, *Nature*, 404, 66–69, 2000. 30
- Lance, S., Raatikainen, T., Onasch, T. B., Worsnop, D. R., Yu, X.-Y., Alexander, M., Stolzenburg, M., McMurry, P., Smith, J. N., and Nenes, A.: Aerosol mixing state, hygroscopic growth and cloud activation efficiency during MIRAGE 2006, *Atmospheric Chemistry and Physics*, 13, 5049–5062, 2013. 73, 127
- Leck, C. and Svensson, E.: Importance of aerosol composition and mixing state for cloud droplet activation over the Arctic pack ice in summer, *Atmospheric Chemistry and Physics*, 15, 2545–2568, 2015. 29, 45
- Leck, N. and Svensson, E.: Importance of aerosol composition and mixing state for cloud droplet activation in the high Arctic, *Atmospheric Chemistry and Physics Discussion*, 14, 21 223–21 283, 2014. 73

- Lesins, G., Chylek, P., and Lohmann, U.: A study of internal and external mixing scenarios and its effect on aerosol optical properties and direct radiative forcing, *Journal of Geophysical Research: Atmospheres* (1984–2012), 107, AAC–5, 2002a. 45
- Lesins, G., Chylek, P., and Lohmann, U.: A study of internal and external mixing scenarios and its effect on aerosol optical properties and direct radiative forcing, *Journal of Geophysical Research: Atmospheres* (1984–2012), 107, AAC–5, 2002b. 73
- Levin, Z., Ganor, E., and Gladstein, V.: The effects of desert particles coated with sulfate on rain formation in the eastern Mediterranean, *Journal of Applied Meteorology*, 35, 1511–1523, 1996. 32
- Lu, J. and Bowman, F. M.: A detailed aerosol mixing state model for investigating interactions between mixing state, semivolatile partitioning, and coagulation, *Atmospheric Chemistry and Physics*, 10, 4033–4046, 2010. 36, 37, 42, 46, 73, 97
- Mallet, M., Roger, J., Despiiau, S., Putaud, J., and Dubovik, O.: A study of the mixing state of black carbon in urban zone, *Journal of Geophysical Research: Atmospheres* (1984–2012), 109, doi: 10.1029/2003JD003940, 2004. 27, 45, 73, 86, 97
- Mallet, V., Quélo, D., Sportisse, B., Ahmed de Biasi, M., Debry, É., Korsakissok, I., Wu, L., Roustan, Y., Sartelet, K., Tombette, M., et al.: Technical Note: The air quality modeling system Polyphemus, *Atmospheric Chemistry and Physics*, 7, 5479–5487, 2007. 35, 74, 98
- Mann, G., Carslaw, K., Ridley, D., Spracklen, D., Pringle, K., Merikanto, J., Korhonen, H., Schwarz, J., Lee, L., Manktelow, P., et al.: Intercomparison of modal and sectional aerosol microphysics representations within the same 3-D global chemical transport model, *Atmospheric Chemistry and Physics*, 12, 4449–4476, 2012. 36
- Maxwell, G.: JC, “Colours in metal glasses and metal films,” *Philos. Trans. R. Soc. London, Sect. A*, 3, 385–420, 1904. 84
- McGraw, R.: Description of aerosol dynamics by the quadrature method of moments, *Aerosol Science and Technology*, 27, 255–265, 1997. 25
- McInnes, L., Covert, D., Quinn, P., and Germani, M.: Measurements of chloride depletion and sulfur enrichment in individual sea-salt particles collected from the remote marine boundary layer, *Journal of Geophysical Research: Atmospheres* (1984–2012), 99, 8257–8268, 1994. 32
- McMurry, P. H.: A review of atmospheric aerosol measurements, *Atmospheric Environment*, 34, 1959–1999, 2000. 45
- Mie, G.: Beiträge zur Optik trüber Medien, speziell kolloidaler Metallösungen, *Annalen der Physik*, 330, 377–445, 1908. 84
- Murphy, D., Cziczo, D., Froyd, K., Hudson, P., Matthew, B., Middlebrook, A., Peltier, R. E., Sullivan, A., Thomson, D., and Weber, R.: Single-particle mass spectrometry of tropospheric aerosol particles, *Journal of Geophysical Research: Atmospheres* (1984–2012), 111, doi: 10.1029/2006JD007340, 2006. 9, 26, 28, 73, 97

- Myhre, G., Samset, B., Schulz, M., Balkanski, Y., Bauer, S., Berntsen, T., Bian, H., Bellouin, N., Chin, M., Diehl, T., et al.: Radiative forcing of the direct aerosol effect from AeroCom Phase II simulations, *Atmospheric Chemistry and Physics*, 13, 1853–1877, 2013. 45
- Nenes, A. and Seinfeld, J. H.: Parameterization of cloud droplet formation in global climate models, *Journal of Geophysical Research: Atmospheres* (1984–2012), 108, 2003. 90
- Nenes, A., Pandis, S. N., and Pilinis, C.: ISORROPIA: A new thermodynamic equilibrium model for multiphase multicomponent inorganic aerosols, *Aquatic geochemistry*, 4, 123–152, 1998. 48, 74, 99
- Oshima, N., Koike, M., Zhang, Y., Kondo, Y., Moteki, N., Takegawa, N., and Miyazaki, Y.: Aging of black carbon in outflow from anthropogenic sources using a mixing state resolved model: Model development and evaluation, *Journal of Geophysical Research*, 114, 1–17, 2009a. 98
- Oshima, N., Koike, M., Zhang, Y., Kondo, Y., Moteki, N., Takegawa, N., and Miyazaki, Y.: Aging of black carbon in outflow from anthropogenic sources using a mixing state resolved model: 1. Model development and evaluation, *Journal of Geophysical Research: Atmospheres* (1984–2012), 114, 2009b. 37, 42, 46, 73
- Pandis, S. N., Wexler, A. S., and Seinfeld, J. H.: Secondary organic aerosol formation and transport—II. Predicting the ambient secondary organic aerosol size distribution, *Atmospheric Environment. Part A. General Topics*, 27, 2403–2416, 1993. 51
- Pascal, M., Corso, M., Chanel, O., Declercq, C., Badaloni, C., Cesaroni, G., Henschel, S., Meister, K., Haluza, D., Martin-Olmedo, P., et al.: Assessing the public health impacts of urban air pollution in 25 European cities: Results of the Aphekom project, *Science of the Total Environment*, 449, 390–400, 2013. 45, 73
- Petzold, A. and Schönlinner, M.: Multi-angle absorption photometry—a new method for the measurement of aerosol light absorption and atmospheric black carbon, *Journal of Aerosol Science*, 35, 421–441, 2004. 97
- Pilinis, C., Capaldo, K., Nenes, A., and Pandis, S.: MADM-A new multicomponent aerosol dynamics model, *Aerosol Science & Technology*, 32, 482–502, 2000. 50
- Polichetti, G., Cocco, S., Spinali, A., Trimarco, V., and Nunziata, A.: Effects of particulate matter (PM 10, PM 2.5 and PM 1) on the cardiovascular system, *Toxicology*, 261, 1–8, 2009. 19
- Putaud, J.-P., Van Dingenen, R., Alastuey, A., Bauer, H., Birmili, W., Cyrys, J., Flentje, H., Fuzzi, S., Gehrig, R., Hansson, H.-C., et al.: A European aerosol phenomenology–3: Physical and chemical characteristics of particulate matter from 60 rural, urban, and kerbside sites across Europe, *Atmospheric Environment*, 44, 1308–1320, 2010. 18

- Raes, F., Van Dingenen, R., Vignati, E., Wilson, J., Putaud, J.-P., Seinfeld, J. H., and Adams, P.: Formation and cycling of aerosols in the global troposphere, *Atmospheric Environment*, 34, 4215–4240, 2000. 9, 29, 30
- Riemer, N. and West, M.: Quantifying aerosol mixing state with entropy and diversity measures, *Atmospheric Chemistry and Physics*, 13, 11 423–11 439, 2013. 39, 95, 98, 114, 122, 123, 125
- Riemer, N., West, M., Zaveri, R. A., and Easter, R. C.: Simulating the evolution of soot mixing state with a particle-resolved aerosol model, *Journal of Geophysical Research*, 114, D09 202, 2009. 36, 46, 47, 73, 98
- Russell, A. and Dennis, R.: NARSTO critical review of photochemical models and modeling, *Atmospheric Environment*, 34, 2283–2324, 2000. 37, 103
- Russell, L. M. and Seinfeld, J. H.: Size-and composition-resolved externally mixed aerosol model, *Aerosol Science and Technology*, 28, 403–416, 1998. 73, 97
- Sartelet, K., Hayami, H., Albriet, B., and Sportisse, B.: Development and preliminary validation of a modal aerosol model for tropospheric chemistry: MAM, *Aerosol Science and Technology*, 40, 118–127, 2006. 36, 97
- Sartelet, K., Debry, E., Fahey, K., Roustan, Y., Tombette, M., and Sportisse, B.: Simulation of aerosols and gas-phase species over Europe with the POLYPHEMUS system: Part I—Model-to-data comparison for 2001, *Atmospheric Environment*, 41, 6116–6131, 2007. 34, 35, 45, 74, 98, 107
- Schmidt, H., Derognat, C., Vautard, R., and Beekmann, M.: A comparison of simulated and observed ozone mixing ratios for the summer of 1998 in Western Europe, *Atmospheric Environment*, 35, 6277–6297, 2001. 34
- Seaton, A., Godden, D., MacNee, W., and Donaldson, K.: Particulate air pollution and acute health effects, *The Lancet*, 345, 176–178, 1995. 19
- Seigneur, C., Hudischewskyj, a. B., Seinfeld, J. H., Whitby, K. T., Whitby, E. R., Brock, J. R., and Barnes, H. M.: Simulation of Aerosol Dynamics: A Comparative Review of Mathematical Models, *Aerosol Science and Technology*, 5, 205–222, 1986. 52, 53
- Seigneur, C., Pun, B., Pai, P., Louis, J.-F., Solomon, P., Emery, C., Morris, R., Zahniser, M., Worsnop, D., Koutrakis, P., et al.: Guidance for the performance evaluation of three-dimensional air quality modeling systems for particulate matter and visibility, *Journal of the Air & Waste Management Association*, 50, 588–599, 2000. 37
- Seinfeld, J. H.: Air pollution: A half century of progress, *AIChE Journal*, 50, 1096–1108, 2004. 34
- Seinfeld, J. H. and Pandis, S. N.: *Atmospheric Chemistry and Physics: From Air Pollution to Climate Change*, John Wiley & Sons, second edn., 1998. 89
- Seinfeld, J. H. and Pandis, S. N.: *Atmospheric chemistry and physics: from air pollution to climate change*, John Wiley & Sons, 2006. 30, 31, 32, 34

- Seinfeld, J. H. and Pandis, S. N.: Atmospheric chemistry and physics: from air pollution to climate change, John Wiley & Sons, 2012. 86
- Skamarock, W., Klemp, J., Dudhia, J., Gill, D., Barker, D., Duda, M., Huang, X., Wang, W., and Powers, J.: A description of the advanced research WRF version 3. NCAR Technical Note, NCAR/TN\ u2013475? STR, 123 pp, 2008. 75, 101
- Sportisse, B.: Pollution atmosphérique: des processus à la modélisation, Springer Science & Business Media, 2008. 9, 35
- Stier, P., Feichter, J., Kinne, S., Kloster, S., Vignati, E., Wilson, J., Ganzeveld, L., Tegen, I., Werner, M., Balkanski, Y., et al.: The aerosol-climate model ECHAM5-HAM, *Atmospheric Chemistry and Physics*, 5, 1125–1156, 2005. 36, 46, 73, 98
- Stockwell, W. R., Kirchner, F., Kuhn, M., and Seefeld, S.: A new mechanism for regional atmospheric chemistry modeling, *Journal of Geophysical Research: Atmospheres* (1984–2012), 102, 25 847–25 879, 1997. 36
- Tolbert, P. E., Mulholland, J. A., Macintosh, D. L., Xu, F., Daniels, D., Devine, O. J., Carlin, B. P., Klein, M., Butler, A. J., Nordenberg, D. F., et al.: Air quality and pediatric emergency room visits for asthma and Atlanta, Georgia, *American journal of epidemiology*, 151, 798–810, 2000. 19
- Tombette, M., Chazette, P., Sportisse, B., and Roustan, Y.: Simulation of aerosol optical properties over Europe with a 3-D size-resolved aerosol model: comparisons with AERONET data, *Atmospheric Chemistry and Physics*, 8, 7115–7132, 2008. 84
- Twomey, S.: The influence of pollution on the shortwave albedo of clouds, *Journal of the atmospheric sciences*, 34, 1149–1152, 1977. 21
- Vehkamäki, H., Kulmala, M., Napari, I., Lehtinen, K. E., Timmreck, C., Noppel, M., and Laaksonen, A.: An improved parameterization for sulfuric acid–water nucleation rates for tropospheric and stratospheric conditions, *Journal of Geophysical Research: Atmospheres* (1984–2012), 107, AAC–3, 2002. 47, 74
- Verwer, J. G., Spee, E., Blom, J., and Hundsdorfer, W.: A second-order Rosenbrock method applied to photochemical dispersion problems, *SIAM Journal on Scientific Computing*, 20, 1456–1480, 1999. 50
- Vestreng, V.: Review and Revision. Emission data reported to CLRTAP. EMEP MSC-W Status Report 2003, Tech. rep., Meteorological Synthesizing Centre–West, Norwegian Meteorological Institute, Oslo, 2003. 99
- Wang, Y., Sartelet, K., Bocquet, M., and Chazette, P.: Assimilation of ground versus lidar observations for PM 10 forecasting, *Atmospheric Chemistry and Physics*, 13, 269–283, 2013. 35
- Wang, Y., Sartelet, K. N., Bocquet, M., and Chazette, P.: Modelling and assimilation of lidar signals over Greater Paris during the MEGAPOLI summer campaign, *Atmospheric Chemistry and Physics*, 14, 3511–3532, 2014. 75, 77, 84, 103

- Wex, H., McFiggans, G., Henning, S., and Stratmann, F.: Influence of the external mixing state of atmospheric aerosol on derived CCN number concentrations, *Geophysical Research Letters*, 37, 2010. 73
- Wexler, A. S. and Seinfeld, J. H.: The distribution of ammonium salts among a size and composition dispersed aerosol, *Atmospheric Environment. Part A. General Topics*, 24, 1231–1246, 1990. 51
- Whitby, E. R. and McMurry, P. H.: Modal aerosol dynamics modeling, *Aerosol Science and Technology*, 27, 673–688, 1997. 25, 36, 45
- WHO: Burden of disease from Ambient Air Pollution for 2012, URL http://www.who.int/phe/health_topics/outdoorair/databases/en/, [Online; accessed 26-March-2015], 2014. 20
- Yarwood, G., Rao, S., Yocke, M., and Whitten, G.: Updates to the carbon bond chemical mechanism: CB05, Tech. rep., Final report to the US EPA, RT-0400675, 2005. 36, 74, 98
- Yu, F. and Turco, R. P.: Ultrafine aerosol formation via ion-mediated nucleation, *Geophysical Research Letters*, 27, 883–886, 2000. 30
- Zhang, Y., Seigneur, C., Seinfeld, J. H., Jacobson, M. Z., and Binkowski, F. S.: Simulation of Aerosol Dynamics: A Comparative Review of Algorithms Used in Air Quality Models, *Aerosol Science and Technology*, 31, 487–514, 1999. 52, 53
- Zhang, Y., Pun, B., Vijayaraghavan, K., Wu, S.-Y., Seigneur, C., Pandis, S. N., Jacobson, M. Z., Nenes, A., and Seinfeld, J. H.: Development and application of the model of aerosol dynamics, reaction, ionization, and dissolution (MADRID), *Journal of Geophysical Research: Atmospheres* (1984–2012), 109, 2004. 36, 45
- Zhang, Y., McMurry, P. H., Yu, F., and Jacobson, M. Z.: A comparative study of nucleation parameterizations: 1. Examination and evaluation of the formulations, *Journal of Geophysical Research: Atmospheres* (1984–2012), 115, 2010. 47
- Zhu, S., Sartelet, K., and Seigneur, C.: A size-composition resolved aerosol model for simulating the dynamics of externally mixed particles: SCRAM (v 1.0), *Geoscientific Model Development*, 8, 1595–1612, 2015a. 42, 73, 74, 76, 97, 98, 99
- Zhu, S., Sartelet, N. K., Zhang, Y., and Nenes, A.: Three-dimensional modelling of the mixing state of particles over Greater Paris, *Journal of Geophysical Research*, p. submitted, 2015b. 98, 99, 103, 107